FLUCTUATIONS NEAR THIN FILMS OF POLYMERS, ORGANIC PHOTOVOLTAICS, AND ORGANIC SEMICONDUCTORS PROBED BY ELECTRIC FORCE MICROSCOPY

A Dissertation

Presented to the Faculty of the Graduate School

of Cornell University

in Partial Fulfillment of the Requirements for the Degree of

Doctor of Philosophy

by

Nikolas Charles Hoepker

January 2013

FLUCTUATIONS NEAR THIN FILMS OF POLYMERS, ORGANIC PHOTOVOLTAICS, AND ORGANIC SEMICONDUCTORS PROBED BY ELECTRIC FORCE MICROSCOPY

Nikolas Charles Hoepker, Ph.D.

Cornell University 2013

Scanned probe microscopy has the ability to image a surface by probing dynamic fluctuations. In this work, we measure surface-induced fluctuations as noise in the cantilever resonance frequency. We provide a theoretical basis of surface-induced cantilever frequency noise, which we then use to study thin polymer films, organic photovoltaics, and organic semiconductors.

Over polymer films we demonstrate that the observed frequency noise is due to fluctuations in the sample's electric polarization. We have developed a theory that links these fluctuations to the dielectric function of the polymer. Our theory correctly predicts the magnitude and spectral shape of the observed frequency noise, as well as its dependence on distance and tip-voltage.

Over polymer-blend heterojunction solar cells we find that in the presence of light, cantilever frequency noise increases by almost two orders of magnitude and, remarkably, shows a wavelength dependence that follows the absorption spectrum of one of the polymer components. We attribute the light-induced noise to charge trapping and detrapping.

In molecular organic semiconductors, we investigate charge-induced frequency noise. Charge motion in these materials has to date been described using microscopic charge-hopping models, which essentially neglect long-range inter-carrier interactions. Here we demonstrate that inter-carrier interactions cannot be ignored in a frequency noise experi-

ment because these interactions suppress fluctuations in the electrostatic potential by several orders of magnitude.

keywords: transistor, poly(3-hexylthiophene) (P3HT), N,N'-Diphenyl-N,N'-di(3-tolyl)-4-benzidine (TPD),

BIOGRAPHICAL SKETCH

Nikolas Hoepker was born in Switzerland on June 27, 1983. He grew up in Liechtenstein, where he attended the Liechtensteinische Gymnasium. He soon discovered his interest in physics and, encouraged by his physics teacher, Fritz Epple, he attended two international physics olympiads in Leicester, England in 2000 and in Antalya, Turkey in 2001. After graduating from the Liechtensteinische Gymnasium in 2002, he moved to California to further pursue his studies in physics at the University of California, Davis. Under the direction of Professor Rajif Singh, he modeled stress induced DNA denaturation. In 2006, he graduated with a Bachelor of Science in Physics from the University of California, Davis and moved to New York to pursue a PhD in physics at Cornell University. His doctoral work was completed under the supervision of Professor John Marohn in 2012.

This thesis is dedicated to my parents, Chris and Waltraud Hoepker.

ACKNOWLEDGEMENTS

I would like to thank my parents for providing their continual support. This work would not have been possible without their help. I am also thankful to my brother, Alexander, for his moral and intellectual support.

I would like to thank Professor Marohn for the opportunity to work in his lab. He has always been both very inspiring and supportive, and has a unique, intuitive sense of physics. I am indebted to Showey Yazdanian who has been a great lab partner, mentor, and friend. I also want to thank Swapna Lekkala and Professor Roger Loring, who co-authored the work described in Chapter 3 [1] and Chapter 5 [2], as well as Dr. Justin Luria who performed the experiments relevant to the work in Chapter 4 [3].

I am thankful for the supportive lab environment in the Marohn group, for the pleasant company of my lab mates, and for all the baked goods provided during group meetings.

Finally, I would like to thank the white house for offering their couch to crash on on countless occasions. I want to thank all of my friends for filling my life with music and laughter, and the Ithaca tango community for the opportunity to learn such a unique style of dance. I'm also grateful for the chance to have lived in Ithaca with its numerous gorges and swimming holes.

This work was funded by the National Science Foundation through the Cornell Center for Nanoscale Systems (EEC-0117770 and EEC-0646547) and through single-investigator grants to John Marohn (DMR-1006633) and Roger Loring (CHE-0743299). This work was performed in part at the Cornell NanoScale Science and Technology Facility, a member of the National Nanotechnology Infrastructure Network, supported by the National Science Foundation (ECS-0335765).

TABLE OF CONTENTS

LIST OF FIGURES

LIST OF TABLES

Chapter 1

Introduction

Scanned probe microscopy has enabled the nanometer-resolution imaging of surfaces with contrast based on topography [4], chemical forces [4–6], magnetization [5, 7], capacitance [8, 9], and electrostatic potential [8, 10]. Scanned probe microscopy also has the capacity to image a surface by probing dynamical fluctuations. Such fluctuations can be probed indirectly in measurements of sample-induced dissipation by application of the fluctuation-dissipation theorem [11–17]. Fluctuations may also be observed directly through stochastic force gradients exerted by the sample on the cantilever, which produces cantilever frequency noise. In Chapter 2, we provide the theoretical and experimental basis for measuring cantilever frequency noise in the atomic force microscope geometry, where the cantilever tip moves perpendicular to the sample surface.

Sample induced fluctuations in the electric polarization can set an ultimate limit for the sensitivity of force (or force gradient) detection. For example, in magnetic resonance force microscopy, such fluctuations currently limit the sensitivity of this technique [18]. Israeloff and coworkers introduced the use of a charged atomic force microscope tip (electric force microscopy) to probe polarization fluctuations in a glassy polymer film [19–24]; the observed cantilever frequency noise was ascribed to thermal fluctuations in the electric polarization of the sample. In Chapter 3 we provide a complete description of the cantilever frequency noise induced by such fluctuations in the electric polarization. Our measurements above thin polymer films agree well with the predicted dependence of the cantilever frequency noise on tip-sample distance, frequency, and tip voltage.

Apart from our studies of fluctuations in the electric polarization over thin films, we apply our theoretical framework of frequency noise to organic devices, which offer the promise of cheap alternatives to silicon based technologies. Despite a large body of research, degradation pathways in many organic photovoltaic materials and polymeric semiconductors remain unknown. However, it is known that these devices suffer from degradation due to charge trapping. In Chapter 4, we measure charge trapping and detrapping in bulk heterojunction solar cells as a fluctuation in the cantilever resonance frequency as observed in an electric force microscope experiment. Unlike earlier studies of traps [25, 26], our experiments are sensitive to the dynamics of charge trapping and detrapping. We found that in the presence of variable-wavelength light, cantilever frequency noise increases by almost two orders of magnitude. We attribute the increase in noise to charge trapping and detrapping. We have developed a theory that reasonably reproduces the magnitude and spectral shape of the frequency noise as well as the dependence on distance and tip-voltage. Our measurements elucidate details in the trapping mechanism and allow us to determine the density of trapped charges. With accurate modeling, such measurements give valuable information on charge trapping and inform the synthetic process.

We also investigate frequency noise generated by molecular organic semiconductors with mobile charges. We focus on molecular materials because, in addition to being of practical interest in low-cost circuits, the long Debye screening length makes Coulomb interactions non-negligible at carrier densities typically present in working devices. In amorphous materials, the dependence of carrier motion on carrier density, electric field, and temperature has to date been described using microscopic charge-hopping models [27–33] which largely neglect long-ranged inter-carrier interactions. Recently, it has been shown that inter-carrier interactions greatly enhance the performance of electronic ratchet circuits [34]. In Chapter 5 we propose and demonstrate another dramatic signature of inter-carrier interactions, the

suppression of electrostatic potential fluctuations by several orders of magnitude.

Chapter 2

Methods

2.1 Experimental Methods

In this work, we use an electric force microscope to probe small electrical forces that originate from thin organic dielectric films, organic semiconductor solar cells, and organic semiconductor transistors. These forces arise through a capacitive coupling between the organic material and a metal coated cantilever. Rather than observing these forces by measuring the deflection of the cantilever, we instead focus on shifts in the cantilever resonance frequency f_c. To this end, the cantilever is driven at its own resonance frequency, so that its displacement given by

$$\Delta z(t) = z_0(t) \cos\left(2\pi f_c(t) t\right). \tag{2.1}$$

Here $z_0(t)$ and $f_c(t)$ are the instantaneous cantilever amplitude and resonance frequency, respectively. These two quantities acquire a time dependence due to a time-dependent interaction with the sample, thermal noise in the cantilever, and noise in the instrumentation. In this work we focus on measuring the resonance frequency $f_c(t)$ rather than the cantilever amplitude $z_0(t)$, or for that matter, displacements $\delta z(t)$ of the un-driven cantilever. A merit of frequency detection is that it enables measuring low-frequency forces while at the same time being insensitive to low-frequency noise injected by the instrumentation, as will be discussed in sections Section 2.4.3 and Section 2.4.4.

In order to measure the instantaneous cantilever resonance frequency, one must have a means both to drive the cantilever and to detect its position. The cantilever position is

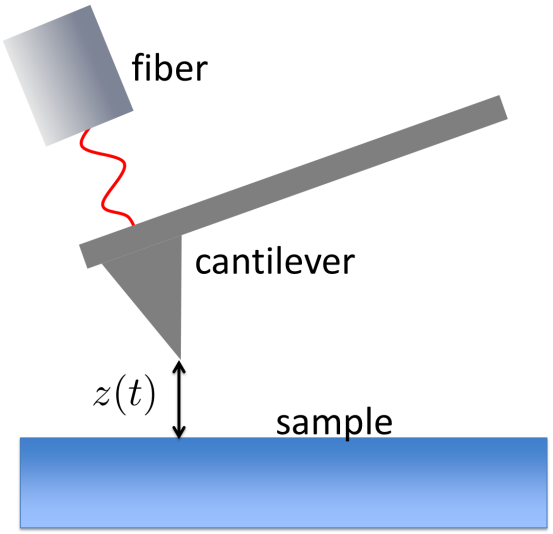

Figure 2.1: An artist's rendering of the electric force microscope cantilever a distance z above a sample.

detected by laser interferometry [35, 36]. A sketch of the cantilever and the laser beam is shown Figure 2.1. A nice discussion of the basic principle of laser interferometry can be found in Ref. 36. Briefly, the cantilever displacement at the location of the laser spot $\Delta z(t)$ is read as a voltage $V(t)$ on the photo diode,

$$\begin{aligned} V(t) &= V_0 + \frac{V_{\mathrm{pk-pk}}}{2} \sin\left(\frac{4\pi(\Delta z(t) + z_0)}{\lambda + \Delta\lambda}\right) \\ V(t) &\approx V_0 + \frac{V_{\mathrm{pk-pk}}}{2} \sin\left(\frac{4\pi\Delta z(t)}{\lambda} + \frac{4\pi z_0}{\lambda + \Delta\lambda}\right), \end{aligned} \tag{2.2}$$

where $z_0 \gg \Delta z$ is the mean distance from the end of the fiber to the reflecting pad (ie. the cantilever), $\lambda = 1310$ nm is the wavelength of the laser, and $\Delta\lambda$ is a small temperature-dependent shift in its wavelength of typically less than a percent, which is controlled using a temperature controller (ILX Lightwave LDT-5910B). The quantity $V_{\mathrm{pk-pk}}$ is the maximum peak-to-peak voltage in the photo detector. $V_{\mathrm{pk-pk}}$ usually determined experimentally from the maximum peak-to-peak voltage that is observed when the cantilever is driven at large oscillation amplitudes. If the distance z_0 is big enough (0.2 mm is typical), it is possible

to adjust $\Delta\lambda$ such that the second argument in 2.2 is equal to integer multiples of π, e.g. the cantilever is "on fringe". For small oscillations, $\Delta z \ll \lambda$, changes in the interferometer voltage can be approximated as

$$\Delta V(t) \approx \frac{2\pi c V_{\mathrm{pk-pk}}}{\lambda} \Delta z_t(t) \tag{2.3}$$

where we have written the displacement of the cantilever at the location spot $\Delta z(t) = c\Delta z_t(t)$ in terms of the displacement of the cantilever tip $\Delta z_t(t)$. The quanity c is a geometrical factor defined by [37]

$$c \equiv \frac{\text{distance from the base of the cantilever to the laser spot}}{\text{cantilever length}}. \tag{2.4}$$

If the laser spot is located at the cantilever tip, we have $c = 1$. Otherwise, $c < 1$. The fraction in Eq. 2.4 is the conversion factor between cantilever tip displacement and voltage. Using laser interferometry to detect cantilever displacement, the cantilever is driven by self-oscillation using a positive feedback loop [38]. For the cantilever to be driven on-resonance, the driving force must be phase shifted by $\pi/2$ (see Section 2.3) with respect to the cantilever displacement. The phase shift of $\pi/2$ is achieved using a (variable-phase) phase shifting circuit. The voltage $\Delta V(t)$ is connected to the input of this circuit and the output is used to drive a small piezo-electric crystal to which the cantilever is attached. The rms-squared of the piezo drive voltage can be set with this circuit. A band-pass filter (see Figure 2.2) is used to reduce both low- and high-frequency noise and to avoid exciting higher order harmonic modes of the cantilever. The cutoff frequency of the filter is set close to the resonance frequency of the cantilever, as explained in the caption of Figure 2.2. In order to convert the position signal $z(t)$ into a frequency $f_c(t)$, we use a software frequency demodulator, which is discussed in more detail in Ref. 39 and in the supporting information of Ref. 1. In order to avoid aliasing, the position signal is passed through a 20^{th} order Butterworth bandpass filter centered at f_c, as discussed in Ref. 39.

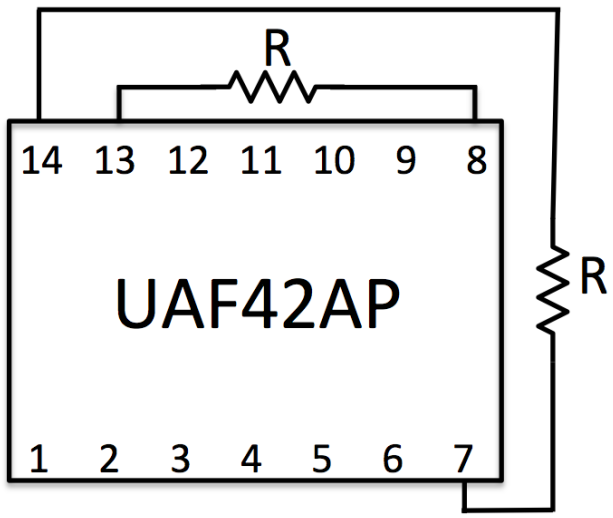

Figure 2.2: A diagram of the bandpass filtering circuit. The two resistors are of equal resistance and determine the bandpass filter frequency $f_{\text{pass}} = \frac{1}{2\pi RC}$ where $C = 1$ nF, which should be set close to the cantilever resonance frequency f_c. At the time of writing, $R = 3.85$ kΩ, such that $f_{\text{pass}} = 41.3$ kHz. The quality factor of the circuit is $Q \approx 5$.

In principle, the cantilever resonance frequency $f_c(t)$ in Eq. 2.1 responds instantaneously to an external perturbation. This can be seen by solving the equations of motion of a harmonic oscillator. If the spring constant of a harmonic oscillator is changed at time $t = 0$, the resonance frequency also changes at $t = 0$. In practice, however, the response time of the cantilever resonance frequency is finite and determined my the feedback circuitry, in particular the bandpass filter.

The work in this thesis distinguishes itself from conventional electric force microscope measurements in that we investigate primarily fluctuating rather than static forces, which manifest themselves in a fluctuating frequency shift $\delta f_c(t)$. In order to be sensitive to such sample-induced frequency fluctuations (or noise), these fluctuations must be larger than those induced by either ambient mechanical vibrations, thermal vibrations, or by the in-

strumentation. The various sources of frequency noise will be discussed in more detail in Section 2.4.2. To reduce ambient vibrations, the scanned probe microscope was installed on a commercial vibration isolation stage (Minus-k 250BM-3). With the electric force microscope stationed in Baker Lab 146, it was found that even with the vibration isolation stage present, the vibration-induced noise frequency noise was prohibitively large to accurately measure sample-induced fluctuations. The parameters used for this measurement are the same as those used in the measurement described in Chapter 3. To reduce ambient vibrations, the scanned probe microscope was moved to PSB B19, where it was placed on a vibration-isolated cement slab. In Figure 2.3 it can be seen that the vibrations observed with the vibration-isolation stage present are approximately two orders of magnitude smaller in PSB B19 than they are in Baker Lab 146. As a result, the vibration-induced frequency noise is lowered by two orders of magnitude as well. While in Baker Lab 146 the vibration-induced low-frequency noise is of the same order of magnitude as sample-induced dielectric noise, the vibration-induced noise was negligible in PSB B19.

Thermo-mechanical displacement fluctuations arise both from collisions with air particles and from thermal interactions with cantilever phonon modes. Placing the electric force microscope in vacuum ($P = 0.5 \times 10^{-6}$ mbar) effectively eliminates the collision-induced noise. Operating in vacuum also reduces sample contamination and prevents damage to the sample due to electrical discharge from the cantilever tip. Electrical discharge is less likely to occur in vacuum because the air, which acts as an ionizing medium, is no longer present. The astute reader may note that mean-free path is larger in vacuum, thereby increasing the chance of an electrical discharge. The latter effect is, however, negligible at pressures below $P = 10^3$ mbar, where the mean-free path is much larger than a typical tip-sample distance (1 μm). Performing cantilever measurements under vacuum poses the challenge of running the necessary fiberoptic cables into the vacuum chamber. For this purpose, we used swageloks

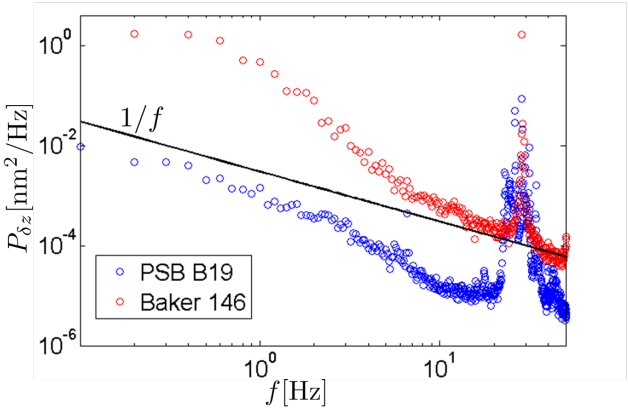

Figure 2.3: Observed noise spectra, $P_{\delta z}(f)$, of the tip-sample distance fluctuations with the electric force microscope placed on a vibration isolation stage (Minus-k 250BM-3) in Baker Lab 146 (red) and in PSB B19 (blue). Displacements, δz were measured by laser interferometry, by mounting a fiber to the probe head and watching the sample stage.

(Swagelok SS-4-UT-A-4) containing 1/4" custom-made teflon ferrules, as discussed in Ref. 39. A #67 hole was drilled through each teflon ferrule to produce a correctly sized hole for the optical fiber. 1/4" rather than 1/8" teflon ferrules were used because it was found that the larger ferrules prevents the teflon from getting irreversibly crushed. [39] Two such feedthroughs were used to accommodate two fiber-optic cables, one to sense the cantilever displacement and the other to observe the motion of the sample along z. A drawing of the probe head along with the fiber optic feedthrough system is shown in Figure 2.4.

The cantilever was moved relative to the sample using a stack of four commercial nanopositioners (Attocube ANPz51, ANSxy50, ANPx51, and ANPx50). The specifications of these positioners are summarized in Table 2.1. A 19-pin cable was used to provide the necessary wires to control these positioners and to apply voltages to the cantilever and the sample. A pin diagram of the various electrical wires is shown in Figure 2.5.

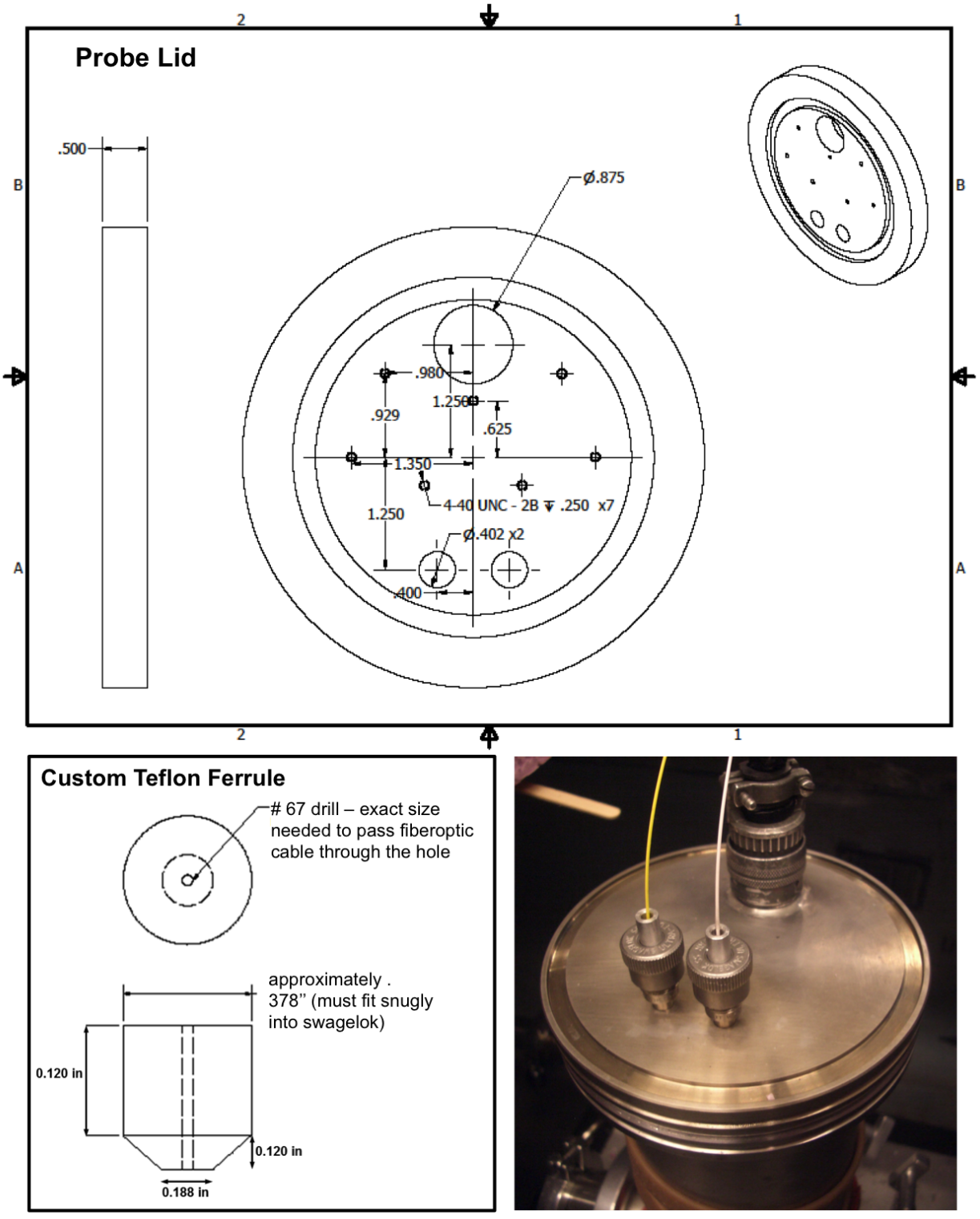

Figure 2.4: A diagram of the fiberoptic feedthrough system. Top: A drawing of the probe lid with two 0.04" holes for two fiberoptic feedthroughs. Bottom left: A drawing of the custom-made teflon ferrule. Bottom right: A picture of the lid, the swageloks (Swagelok SS-4-UT-A-4) containing the teflon ferrules, and of the fiberoptic cables.

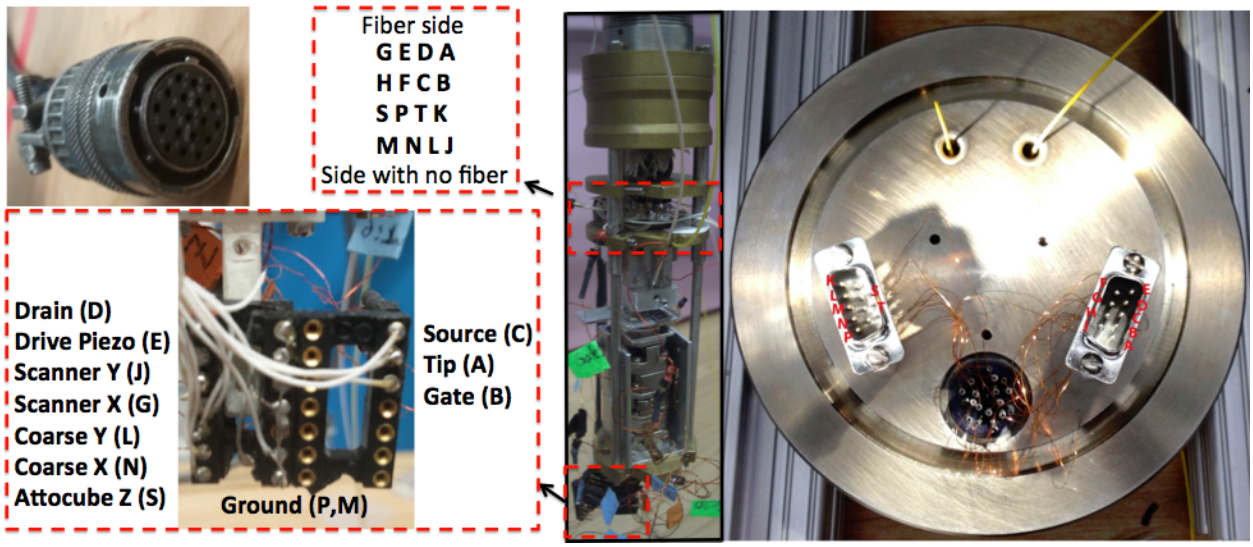

Figure 2.5: A diagram of the electrical connections. The letters (A-P) indicate the individual wires on the 19-pin cable (top left). The arrangement of electrical wires immediately above the cantilever slider is shown in the top left panel. Also shown is the arrangement and function of the electrical wires below the stack of nanopositioners and immediately above the cantilever holder. The wire arrangement at the probe lid is shown in the right panel. Wire F powers a thermistor, wire H provides an additional voltage to the sample (i.e. a 2^{nd} gate voltage), wires P and M supply the ground, and wires K and T are functioning spare electrical connections.

Model	nm / V (fine)	Fine range [um]	Coarse range [mm]	Max Load [g]
ANPz51	50	5	2.5	50
ANPx51	40	5	3	25
ANPx50	130	5	4	25
ANSxy50	577	30	n/a	50

Table 2.1: Specifications of the stack of nanopositioners. The nm/V conversion factor for fine positioning was measured by fiber interferometry for each attocube. The fine and coarse range, and the maximum load was obtained from the manufacturer.

Accurate measurements of the cantilever frequency noise spectrum require signal averaging for a long time, often on the order of minutes. During this time thermally-induced drifts, for instance in the tip-sample distance, obscure the measurement and manifest themselves as low-frequency noise. In order to reduce such thermally-induced low-frequency artifacts, the electric force microscope was placed in a custom-built styrofoam box. An estimate of the effect of thermal drifts on the tip-sample separation can be obtained from the dimensions and thermal expansion coefficients of the various materials used in the probe head. In retrospect, the entire probe should have been designed from the same material (i.e. titanium, which is the material the nanopositioners are made from) in order to minimize thermal effects. From the length of the steel rods (7.8 cm), and the height of the stack of titanium nanopositioners (4.5 cm) and Aluminum cantilever holder (3.3 cm) as shown in Figure 2.6, we estimate a thermal expansion coefficient of

$$(12\cdot 10^{-6}\mathrm{K}^{-1})(7.8\text{ cm})+(8.6\cdot 10^{-6}\mathrm{K}^{-1})(-4.5\text{ cm})+(23\cdot 10^{-6}\mathrm{K}^{-1})(-3.3\text{ cm}) = -214\text{ nm/K}. \tag{2.5}$$

The thermal expansion of the magnet and the sapphire plates [40] was ignored. The negative sign in Eq. 2.5 indicates that the sample approaches the cantilever upon heating. The

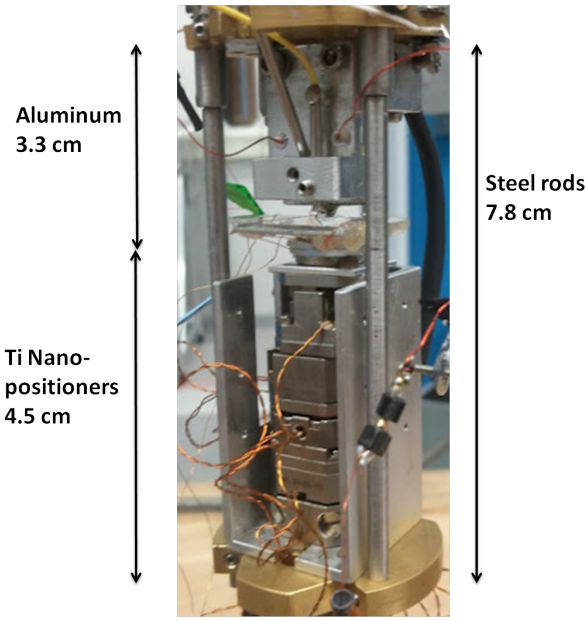

Figure 2.6: A picture of the nanopositioners, the sample, and the cantilever holder. The box protecting the nanopositioners of made of aluminum. Also shown are the various dimensions used to estimate the coefficient of thermal expansion.

sign in Eq. 2.5 was confirmed by heating the probe and monitoring the stage position by interferometry, as shown in Figure 2.7. It was observed that placing the probe inside a styrofoam box reduced thermal drifts by a factor of roughly $\times 5$ to $\sim$ 15 nm in one hour, provided that the probe was allowed to thermally equilibrate overnight.

2.2 Calculating Correlation Functions and Power Spectra

Having discussed the experimental setup, we now examine the physics of cantilever frequency noise. We begin with a discussion of noise spectra and correlations functions in general. Consider a time dependent fluctuating quantity $A(t) = A_0 + \delta A(t)$ of average value A_0. The

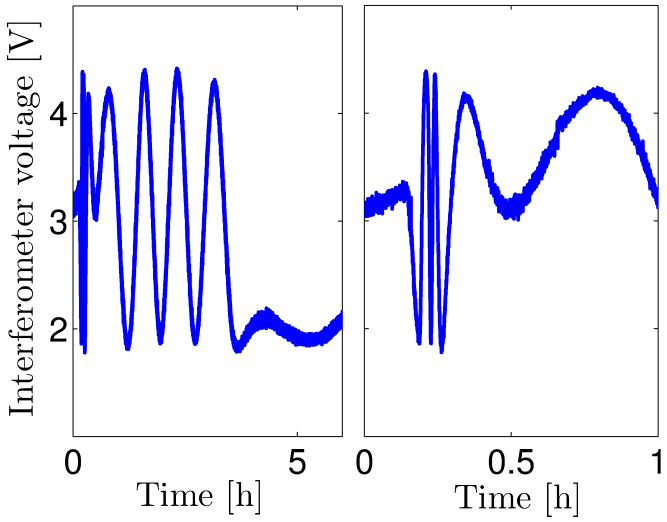

Figure 2.7: Thermally-induced drifts in the tisamle separation: Voltage on the interferometer that tracks the tip-sample motion. A 1600 nm laser (laser diode: Lucent D2525P878, diode mount: Thorlabs LM14S2, laser driver: Thorlabs LDC 202 C, temperature controller: Thorlabs TED 200 C) was used for this measurement. In the right and left panels we display the same data, plotted on different time scales. At time $t = 7$ min, the probe was heated for 8 min using a hot air gun and then allowed to cool back to room temperature. Both heating and cooling of the probe are evident from the interferometer data. After roughly 4 h, the probe reached room temperature. The slower drift in tip-sample distance after 4 h is due to fluctuations in the room temperature.

rms-squared value of the noise $\delta A(t)$ is defined as

$$\delta A^2_{\rm rms} = \left\langle \delta A^2 \right\rangle = \lim_{\tau\to\infty} \frac{1}{\tau} \int_0^\tau dt\, \delta A(t)^2. \tag{2.6}$$

To examine the noise in the signal $A(t)$ in more detail, we commonly form a power spectrum $P_{\delta A}$ of $\delta A(t)$, defined as

$$P_{\delta A}(f) \equiv 4 \int_0^\infty dt \cos(2\pi f t)\, C_{\delta A}(t) \tag{2.7}$$

$$C_{\delta A}(t) = \lim_{\tau\to\infty} \frac{1}{\tau} \int_0^\tau dt' \delta A(t-t')\, \delta A(t'). \tag{2.8}$$

where $C_{\delta A}(t)$ the correlation function of $\delta A(t)$. Here we restrict ourselves to positive frequencies, $f > 0$. Since $P_{\delta A}(f) = P_{\delta A}(-f)$ we don't lose any information with this restriction, which amounts to lumping the negative and positive frequencies together. The constant of proportionality of 4 in Eq. 2.7 assures that the area under the power spectrum equals rms-squared noise, which by Eq. 2.8 is also equal to the zero time correlation function, i.e.

$$\delta A^2_{\rm rms} = \int_0^\infty df\, P_{\delta A}(f) = C_{\delta A}(0). \tag{2.9}$$

Other authors specify power spectra as a function of its angular frequency $\omega = 2\pi f$ rather than the frequency f. Two quantities are commonly used: the spectral density $P_{\delta A}(\omega)$ and the Fourier transform of the correlation function $\hat{C}_{\delta A}(\omega)$, which are defined by

$$\begin{aligned} P_{\delta A}(\omega) &\equiv \frac{2}{\pi} \int_0^\infty dt \cos(\omega t) C_{\delta A}(t) \\ \tilde{C}_{\delta A}(\omega) &\equiv \int_0^\infty dt \cos(\omega t) C_{\delta A}(t) \end{aligned} \tag{2.10}$$

where once again we restrict ourselves to positive frequencies, $\omega = 2\pi f > 0$. We thus have

$$P_{\delta A}(f) = 2\pi P_{\delta A}(\omega) = 4\tilde{C}_{\delta A}(\omega). \tag{2.11}$$

As an example, assume that $P_{\delta A}(f) = Cf^2$. In that case we have from Eq. 2.11 and $\omega = 2\pi f$,

$$P_{\delta A}(\omega) = \frac{C\omega^2}{(2\pi)^3}. \tag{2.12}$$

We note that $P_{\delta A}(\omega)$ is normalized, i.e. $\int_0^\infty d\omega P_{\delta A}(\omega) = \delta A^2_{\rm rms}$, while $\tilde{C}_{\delta A}(\omega)$ is not. To avoid further confusion, we will refrain from using $P_{\delta A}(\omega)$ and $C_{\delta A}(\omega)$, and for that matter from ω in general for the remainder of this thesis.

Power spectra and cross-correlation functions between two fluctuating quantities $\delta A(t)$ and $\delta B(t)$ are defined analogous to Eq. 2.7,

$$\begin{aligned} P_{\delta A,\delta B}(f) &\equiv 4\int_0^\infty dt \cos(2\pi f t) C_{\delta A,\delta B}(t) \\ C_{\delta A,\delta B}(t) &= \lim_{\tau\to\infty}\frac{1}{\tau}\int_0^\infty dt' \delta A(t-t')\,\delta B(t'). \end{aligned} \tag{2.13}$$

Here we show how to compute the power spectrum of derivatives of $\delta A(t)$ and $\delta B(t)$. For example, let $\delta A(t) = \delta\phi(\bar{r},t)$ and $\delta B(t) = \delta\phi(\bar{r}',t)$. In this example, $P_{\delta A,\delta B}(f)$ is the power spectrum of the electric potential $\delta\phi$ between positions $\bar{r}$ and $\bar{r}'$. From Eq. 2.13 it is straightforward to show that

$$P_{\partial_z^n\delta\phi(\bar{r}),\partial_{z'}^m\delta\phi(\bar{r}')}(f) = \partial_z^n\partial_{z'}^m P_{\delta\phi(\bar{r}),\delta\phi(\bar{r}')}(f) \tag{2.14}$$

where z and z' are spatial coordinates associated with $\bar{r}$ and $\bar{r}'$, respectively. For $m = n = 1$, Eq. 2.14 gives the power spectrum of the electric field $E_z = -\partial_z\delta\phi$, i.e.

$$P_{\delta E_z(\bar{r}),\delta E_z(\bar{r}')} = \partial_z\partial_{z'} P_{\delta\phi(\bar{r}),\delta\phi(\bar{r}')}(f). \tag{2.15}$$

We note that the above method only works if the coordinates $\bar{r}$ and $\bar{r}'$ are kept distinct, i.e. one must not set $\bar{r} = \bar{r}'$ before taking the necessary derivatives.

From the definition of the Fourier transform,

$$\widetilde{\delta A}(f) = \int_0^\infty dt e^{-2\pi i f t}\delta A(t), \tag{2.16}$$

one can show using Parseval's theorem that the power spectra in Eq. 2.7 and Eq. 2.13 can also be expressed in terms of a Fourier transform, i.e.

$$P_{\delta A}(f) = \frac{4}{\tau}|\widetilde{\delta A}(f)|^2 \tag{2.17}$$

and

$$P_{\delta A,\delta B}(f) = \lim_{\tau\to\infty} \frac{4}{\tau} \widetilde{\delta A}(f)\, \widetilde{\delta B}^*(f). \tag{2.18}$$

The form in Eq. 2.17 and Eq. 2.18 can be particularly useful. As an example, consider the fluctuating quantities δA, δB_1, and δB_2, which are related by

$$\delta A(t) = c_1 \delta B_1(t) + c_2 \delta B_2(t) \tag{2.19}$$

where c_1 and c_2 are constants. From Eq. 2.17 and Eq. 2.18, it is straightforward to show that

$$P_{\delta A}(f) = |c_1|^2 P_{\delta B}(f) + 2|c_1 c_2^*| P_{\delta B_1,\delta B_2} + |c_2|^2 P_{\delta B_2}. \tag{2.20}$$

If the origin of the fluctuation $\delta A(t)$ is thermal, $P_{\delta A}(f)$ can be calculated from the fluctuation-dissipation theorem,

$$P_{\delta A}(f) = -\frac{4k_B T}{2\pi f} \text{Im } \chi(f), \tag{2.21}$$

where $k_B T$ is the temperature and $\chi(f)$, defined by $\widetilde{\delta A}(f) = \chi(f)\widetilde{\delta B}(f)$, describes a linear response between a generalized coordinate $\widetilde{\delta A}$ and a generalized force $\widetilde{\delta B}$. Fluctuations (i.e. $P_{\delta A}(f)$) and dissipation (i.e. Im $\chi(f)$) are linked because they both arise from a coupling of the stystem (i.e. an oscillator) to a thermal bath. A good discussion of this theorem and its derivation is presented in Ref. 41. In Section 2.3 we will provide an intuitive explanation of this theorem when applied to a harmonic oscillator. Using $\widetilde{\delta A}(f) = \chi(f)\widetilde{\delta B}(f)$, the theorem can also be expressed as

$$P_{\delta B}(f) = \frac{4k_B T}{2\pi f} \text{Im } \chi(f)^{-1}. \tag{2.22}$$

We note there that the sign in Eq. 2.21 and Eq. 2.22 may vary across textbooks, but is always such that the power spectrum is positive. The sign used here (i.e. Im $\chi(f) < 0$) is consistent with the definition of the Fourier transform in Eq. 2.16, which implies that oscillatory terms have time dependence $\delta A(t) = A(0)e^{2\pi i f t}$. The prefactor in Eq. 2.21 ensures consistency

with the equipartition theorem, i.e.

$$\begin{aligned} \int_0^\infty P_{\delta A}(f)df &= -\frac{4k_BT}{2\pi}\mathrm{Im}\int_{-\infty}^{\infty}\frac{\chi(f)}{2f}df \\ \delta A^2_{\mathrm{rms}} &= k_BT\chi(0) \end{aligned} \tag{2.23}$$

where a factor of $-i\pi$ arose from performing the integral using contour integration.

In practice, the time signal $\delta A(t)$ is not acquired continuously, but at some finite acquisition rate $f_{\mathrm{aq}} = 1/\Delta t$ in finite measurement time τ. In that case, the Fourier transform in Eq. 2.16 is replaced by a discrete Fourier transform,

$$\begin{aligned} \widetilde{\delta A}(f_m) &= \sum_{n=1}^{N} e^{-2\pi i f_m t_n}\delta A(t_n) \\ t_n &= n\Delta t, \end{aligned} \tag{2.24}$$

where $N = \tau/\Delta t$ is the number of measurement points. The frequencies f_m are discrete and given by

$$f_m = -\frac{1}{2\Delta t},\ldots,-\frac{1}{\tau},0,\frac{1}{\tau},\frac{2}{\tau},\ldots,\frac{1}{2\Delta t}. \tag{2.25}$$

The maximum frequency in Eq. 2.25 is commonly referred to as the Nyquist frequency, defined by

$$f_{\mathrm{nyq}} = \frac{1}{2\Delta t} = \frac{f_{\mathrm{aq}}}{2}. \tag{2.26}$$

We see that the measurement time τ determines the spacing $b = 1/\tau$ between points in frequency space, while the acquisition rate f_{aq} determines the Nyquist frequency. The quantity b is commonly called the measurement bandwidth. We will use a superscript τ to distinguish the observed noise spectra, $P^{\tau}_{\delta A}(f_m)$, which are acquired over a time τ from the one defined in Eq. 2.17. We note that the observed spectra, $P^{\tau}_{\delta A}(f_m)$, are only defined at the discrete frequencies $f = f_m$.

Having discussed noise spectra, we now briefly review how to compute the signal-to-noise ratio (SNR) from these spectra. The SNR is *defined* as the square root of the ratio of the power in the observed signal to the power in the observed noise, evaluated at the same Fourier component f_m. Given a signal $\Delta A(t) = \Delta A_0 \cos(2\pi f_m t + \theta)$ and an experimentally observed noise power spectrum $P^{\tau}_{\delta A}(f_m)$, this ratio is

$$\text{SNR} \equiv \frac{\Delta A_0}{\sqrt{P^{\tau}_{\delta A}(f_m) b}}. \tag{2.27}$$

We note that for a finite measurement time τ, $P^{\tau}_{\delta A}(f_m)$ is in general not identical to the true noise spectrum $P_{\delta A}(f)$. Let us express Eq. 2.27 in terms of $P_{\delta A}(f)$ rather than $P^{\tau}_{\delta A}(f_m)$ because the former is the quantity predicted by theory. Since acquiring the signal in finite time amounts to applying a rectangular windowing function to the data, $P^{\tau}_{\delta A}(f_m)$ is a convolution of $P_{\delta A}(f)$ with $\text{sinc}^2[2\pi\tau(f_m - f)]$. If we approximate $\text{sinc}^2[2\pi\tau(f_m - f)]$ as a square pulse of width $b = 1/\tau$ centered at f_m, the result of this convolution is

$$\begin{aligned} \text{SNR} &\approx \frac{\Delta A_0}{\sqrt{\int_{f_m - b/2}^{f_m + b/2} P_{\delta A}(f) df}} \\ \text{SNR} &\approx \frac{\Delta A_0}{\sqrt{b P_{\delta A}(f_m)}} \propto \frac{1}{\sqrt{\tau}} \end{aligned} \tag{2.28}$$

where in the last step we assumed the noise to be nearly white over the measurement bandwidth. In this approximation, $P_{\delta A}(f_m) \approx P^{\tau}_{\delta A}(f_m)$. If the signal is measured by lock-in detection rather than by taking the discrete Fourier component at f_m, the SNR is determined by the filtering function of the lock-in amplifier. For the purpose of estimating the SNR, the filtering function can be approximated as a square pulse of width b (the noise-equivalent bandwidth, $b \approx 1/\tau$), so that Eq. 2.28 retains its validity. If the signal to be measured is a DC value, i.e. ΔA_0, the SNR ratio is given by

$$\text{SNR}_{\text{DC}} = \frac{\Delta A_0}{\sqrt{2 \int_0^{b/2} P_{\delta A}(f) df}}, \tag{2.29}$$

as can easily be shown from Eq. 2.28 by lumping together the negative and positive frequency components of the noise, as is done in Eq. 2.7.

2.3 A Review of the Damped Harmonic Oscillator

The equations of motion of a harmonic oscillator are given by

$$m_c \frac{\partial^2 z}{\partial t^2} = -k_c(z-d) - \Gamma \frac{\partial z}{\partial t} \tag{2.30}$$

where k_c is the cantilever spring constant, m_c its mass, $f_c = \frac{1}{2\pi}\sqrt{\frac{k_c}{m_c}}$ its resonance frequency, and equilibrium displacement d. The quantity Γ is called friction and is a figure of merit of the oscillator. Γ describes the ease by which energy is exchanged between the harmonic oscillator and its surroundings (i.e. the lattice) and is therefore a measure of the strenght of the coupling of the oscillator to its surroundings. For a cantilever at ambient conditions, this exchange of energy is mainly due to collisions with gas molecules, while in high-vacuum energy is primarily exchanged through interactions with phonon modes. The connection between Γ and a coupling to the lattice is evident in three different ways. First, by solving the equations of motion of an un-driven oscillator, one can show that the cantilever amplitude z_0 and the energy in the oscillator $E(t) = \frac{1}{2}k_c z(t)^2 + m_c \dot{z}(t)^2$ after an initial excitation decay are

$$\begin{aligned} z_0(t) &= z_0(0)e^{-t/\tau_{\text{ring}}} \\ E(t) &= E(0)e^{-2t/\tau_{\text{ring}}} \end{aligned} \tag{2.31}$$

where

$$\tau_{\text{ring}} \equiv \frac{Q}{\pi f_c} \tag{2.32}$$

is the ringdown time and Q is the quality factor,

$$Q \equiv \frac{k_c}{2\pi f_c \Gamma}. \tag{2.33}$$

The quality factor Q describes the number of oscillations before the cantilever amplitude decays substantially. The larger Γ (or the smaller Q), the faster energy is dissipated to the lattice, which implies a stronger lattice coupling. The connection between Γ and a coupling to the lattice is also evident from the response to a driven oscillation, $F(t) = F_0 e^{2\pi i f t}$. Adding this force $F(t)$ to the right-hand side of Eq. 2.30 and taking a temporal Fourier transform, we obtain

$$\tilde{z}(f) = \chi(f)\tilde{F}(f) \tag{2.34}$$

where

$$\chi(f) = k_c^{-1}\left(1 - \left(\frac{f}{f_c}\right)^2 + i\frac{f}{Qf_c}\right)^{-1} \tag{2.35}$$

is the so-called response function. A sketch of the magnitude squared of the response function, $|\chi|^2$, is shown in Figure 2.8. On resonance ($f = f_c$), the cantilever displacement $\tilde{z}(f)$,

$$\tilde{z}(f_{\text{res}}) = -\frac{iQ}{k_c}\tilde{F}(f_{\text{res}}), \tag{2.36}$$

lags behind the force by a phase $\pi/2$, which implies that force $\tilde{F}$ and velocity $\tilde{v}$ are in phase, thus maximizing the power $\tilde{P} = \tilde{F}\tilde{v}$ transferred to the cantilever. As before we see that a larger value of Γ (smaller Q) is linked to increased dissipation to the lattice, which is evident from the lower on-resonance response obtained with smaller Q. Somewhat more surprisingly, Figure 2.8 also shows that a larger friction coefficient Γ broadens the resonance curve. The physical reason for this broadening is that the cantilever is coupled to off-resonance modes in the lattice. Thirdly, the connection between Γ and the lattice coupling is also evident from thermally-induced force noise $P_{\delta F}$ that the lattice exerts on the oscillator. To make this connection, we compute $P_{\delta F}$ from disspation-fluctuations relation in Eq. 2.22. Using $\delta F(t) = \delta B(t)$ and $\delta z(t) = \delta A(t)$, we have

$$P_{\delta F}(f) = \frac{4k_B T}{2\pi f}\text{Im }\chi^{-1}(f) = 4k_B T\Gamma, \tag{2.37}$$

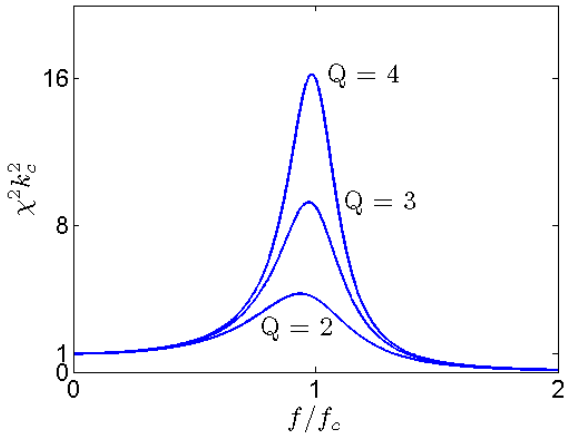

Figure 2.8: The square of the magnitude of the harmonic oscillator response function $\chi(f)$ in Eq. 2.35 for a number of different quality factors Q, as indicated on the graph. As Q is increased (i.e. the friction Γ is lowered), the response function becomes sharper and the on-resonance response larger.

where $k_B T$ is the temperature of the lattice. The disspation-fluctuations relation makes physical sense: A stronger coupling to the lattice (i.e. a larger Γ) results not only in more dissipation *to the lattice* (see Eq. 2.33, Eq. 2.31, and Eq. 2.32), but also in increased thermal fluctuations *from the lattice* (see Eq. 2.37). The thermal noise floor in Eq. 2.37 forms the basis for calculating the *thermally-limited* minimum detectable force $F_{\rm min}$, defined as the force for which SNR= 1. From Eq. 2.28 and Eq. 2.37, we have

$$F_{\rm min} = \sqrt{P_{\delta F} b} = \sqrt{4 k_B T \Gamma b}. \tag{2.38}$$

where $b = \tau^{-1}$ is the measurement bandwidth and $k_B T$ the temperature. The longer the measurement, the smaller the forces that can be detected.

We saw that the cantilever resonance frequency can be obtained from the on-resonance response of the oscillator, while the quality factor can be estimated from the ringdown time

in Eq. 2.32. To obtain the spring constant, we measure the Brownian motion spectrum of the oscillator (e.g. the thermally-induced displacement noise in the absence of an external driving force). From Eq. 2.34, Eq. 2.35, and Eq. 2.37, the Brownian motion spectrum is [42]

$$\begin{aligned} P_{\delta z}^{\text{therm}}(f) &= |\chi(f)|^2 4k_B T\Gamma \\ P_{\delta z}^{\text{therm}}(f) &= \frac{4k_B T}{2\pi k_c Q f_c \left[\left(1-\left(\frac{f}{f_c}\right)^2\right)^2 + \frac{f^2}{Q^2 f_c^2}\right]}. \end{aligned} \tag{2.39}$$

We note that the area under the Brownian motion spectrum in Eq. 2.39, i.e. $\langle \delta z_{\text{rms}}^2 \rangle = \int_0^\infty df P_{\delta z}^{\text{therm}}(f)$, is consistent with what is predicted from the equipartition theorem, i.e $\langle \delta z_{\text{rms}}^2 \rangle = k_B T/k_c$. The area under the Brownian motion spectrum, and therefore the spring constant k_c, can be determined by fitting the observed displacement noise spectrum to thermal noise in Eq. 2.39 plus a white (apparent) displacement noise which is injected by the instrumentation (see Section 2.4.4). The difficulty in fitting the displacement noise data is that the error bars of the data, which determine the weights used for the fit, are themselves dependent on the size of the noise. Prof. John Marohn has developed an iterative procedure to accomplish this fit with self-consistent error bars. The key idea is that the standard deviation at each point in the power spectrum is given by $P_{\delta z}/\sqrt{N_{\text{avg}}}$ where N_{avg} is the number of signals that were averaged to obtain $P_{\delta z}$. Position noise data with a best fit obtained by this method are shown in Figure 2.9. From this fit, one also obtains the quality factor Q and the instrument noise floor. When collecting the Brownian motion data, one must choose the acquisition frequency f_{aq} and the measurement time τ appropriately. The acquisition frequency must be such that the Nyquist frequency (see Eq. 2.26) is well above the cantilever resonance frequency, i.e.

$$f_{\text{aq}} \tilde{>} 3 f_c. \tag{2.40}$$

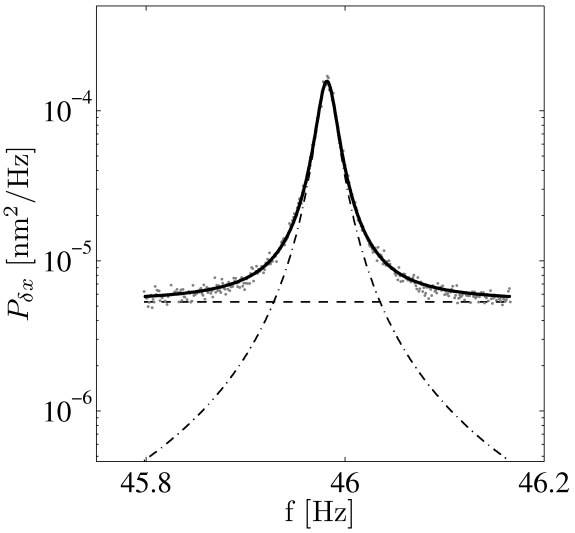

Figure 2.9: The power spectrum of displacement fluctuations of the undriven cantilever (solid line) was obtained from an average of 240 displacement noise spectra each lasting 1 s. Also shown is a fit of the data to the sum of an instrument noise floor (dashed line) and a contribution from the Brownian motion spectrum in Eq. 2.39 (dot-dashed line).

The measurement time τ, which by Eq. 2.25 determines the spacing $1/\tau$ of points in frequency space, is usually chosen such that there are a sufficient number of data points N across the cantilever resonance curves. This leads to the condition

$$\tau > \frac{NQ}{2\pi f_c} = 0.3 \text{ s} \tag{2.41}$$

for $f_c = 50$ kHz, $Q = 3000$, and $N = 30$. In order to increase the accuracy of the fit, the spring constant k_c is usually determined by averaging several hundred such displacement noise spectra, resulting in a typical error of the best fit value of the spring constant of around 15%. Additional errors in the determination of the spring constant may arise from an incorrect estimate of the displacement-to-voltage conversion factor in Eq. 2.4, either by incorrectly estimating $V_{\text{pk}-\text{pk}}$ or the location of the laser spot (i.e. in the constant c). Both factors contribute to erros in the measurement of the displacement noise and therefore the spring constant $k_c \propto V_{\text{pk}-\text{pk}}^{-2} c^{-2}$. Having reviewed the harmonic oscillator, we now discuss the origins of sample-induced frequency shifts.

2.4 Cantilever Frequency Shifts Induced by a Perturbing Hamiltonian

Here we discuss how a perturbation in the Hamiltonian results in a shift in the resonance frequency of the cantilever, which we model as a harmonic oscillator. The presence of a time- and spatially-dependent perturbing Hamiltonian $W(z,t)$ introduces a force $F = -\partial W/\partial z$. The perturbing force alters the equations of motion of the unperturbed harmonic oscillator in Eq. 2.30 as follows,

$$m_c \frac{\partial^2 z}{\partial t^2} = -k_c(z-d) - \Gamma_c \frac{\partial z}{\partial t} - \frac{\partial W}{\partial z}, \tag{2.42}$$

where m_c is the mass, k_c the spring constant, $f_c = \sqrt{k_c/m_c}$ the resonance frequency, $\Gamma_c = k_c/2\pi f_c Q$ is the friction, and Q the quality factor of the oscillator.

Using the Hamiltonian-Jacobi formalism to rewrite Eq. 2.42 in terms of action and angle coordinates, one can show that the perturbed resonance frequency is [43]

$$f(t) = f_c \left(1 + \frac{1}{k_c z_0^2} \left\langle \frac{\partial W}{\partial z} z \right\rangle\right), \tag{2.43}$$

where z_0 is the cantilever amplitude and f_c the unperturbed resonance frequency. The angular brackets indicate a time-weighted average over a cantilever period. We proceed by decomposing Eq. 2.43 into a static and a time dependent term,

$$W(z,t) = \overline{W}(z) + \delta W(z,t). \tag{2.44}$$

Expansion of $W(z,t)$ about the unperturbed equilibrium tip-sample separation $z = d$ yields a static sample-induced frequency shift $\Delta f_c(d)$ associated with $\overline{W}(z)$ and a stochastic frequency shift $\delta f_c(d,t)$ arising from $\delta W(d,t)$. Using $z = z_0 \cos(2\pi f_c t)$ and expanding Eq. 2.43 to second order in $z - d$, we find that the static frequency shift is

$$\Delta f_c(d) = \frac{f_c}{2k_c} \overline{W}_2(d) \tag{2.45}$$

with $\overline{W}_n(d) \equiv d^n \overline{W}(z)/dz^n|_{z=d}$ and $C_n(d) \equiv d^n C(z)/dz^n|_{z=d}$. To fourth order in $z - d$, the frequency shift $\delta f_c(t) = f(t) - \overline{f(t)}$ induced by the perturbing Hamiltonian is

$$\begin{aligned} \delta f_c(d,t) = \frac{f_c}{2k_c} \Big[& \delta W_2(d,t) + k_c^{-1} \left(\overline{W}_3(d)\, \delta W_1(d,t) \right. \\ & \left. + \overline{W}_1(d)\, \delta W_3(d,t) \right) - \frac{5 z_{\mathrm{rms}}^2}{6} \overline{W}_3(d)\, \delta W_3(d,t) \\ & + \frac{z_{\mathrm{rms}}^2}{4} \delta W_4(d,t) \Big]. \end{aligned} \tag{2.46}$$

The term containing δW_2 arises from the harmonic approximation to $\delta W(z,t)$. The two terms containing products of components of W_1 and W_3 arise from the interplay between

cubic anharmonicity in $W(z,t)$ and the shift in equilibrium oscillator displacement caused by terms linear in $z-d$. The term quadratic in components of W_3 is the frequency shift of a cubically perturbed harmonic oscillator, calculated to second order in perturbation theory [44] within an adiabatic approximation in which the potential energy fluctuations $\delta W_3(d,t)$ are taken to be slow with respect to the period of the oscillator. This adiabatic approximation is appropriate here, as the frequency jitter occurs on time scales four orders of magnitude smaller than the cantilever period. This term results from calculating the frequency shift for time-independent potential anharmonicity W_3 and replacing this quantity with the slowly-varying $W_3(d,t)$. The term in Eq. 2.46 proportional to δW_4 is calculated within the same adiabatic approximation to first order in perturbation theory for a quartically perturbed harmonic oscillator [45]. These two terms are proportional to z_{rms}^2, the root-mean-squared displacement of the cantilever from its equilibrium position.

The perturbing Hamiltonian $W(z,t)$ arises from a capacitive coupling between the sample and the cantilever. Here we will assume that during a cantilever oscillation the voltage on the cantilever remains constant, which holds true as long as the RC charging time of the cantilever tip is much shorter than a cantilever period. A scenario where this assumption is relaxed will be discussed in Section 2.5. The electrostatic interaction due to a capacitive coupling between the cantilever tip and a sample separated by a distance z is given by [46, 47],

$$W(z,t) = -\frac{1}{2}C(z(t))\left(V_{\mathrm{t}} - \phi(t)\right)^2 . \tag{2.47}$$

where $\phi(t) = \phi_c + \delta\phi(t)$ is the sample's contact potential, $C(z)$ is the tip-sample capacitance and V_t is the applied tip voltage. The time dependence of $W(z,t)$ may arise either from a time dependent cantilever displacement $z(t)-d$ or from a time dependent surface contact potential $\phi(t)$. Within the harmonic approximation, the static frequency shift Δf_c can be

computed from Eq. 2.45 and Eq. 2.47 as

$$\Delta f_c(d) = -\frac{f_c}{4k_c} C_2(d)^2 \left(V_\mathrm{t} - \phi_c\right)^2 . \tag{2.48}$$

A subscript is used to indicate differentiation with respect to z, i.e $C_n = (\partial/\partial z)^n C(z)$. Since the second derivative of the capacitance, C_2, is positive, the sample-induced frequency shift is always negative. The sign of the frequency shift will be examined in more detail in Section 2.5. To estimate the capacitance $C(z)$ between the cantilever and a metal-backed dielectric sample, the cantilever tip is represented as a cone and as a sphere [48]. The contributions to frequency noise (or frequency shifts) for the conical and spherical cantilever tip are calculated separately and added together. The contribution of the sphere is estimated by modeling the probe tip as a sphere of radius R centered at height $d + R$ over a metal-backed dielectric film of thickness h and dielectric constant $\epsilon(f) = \epsilon_0\epsilon_r$. From Ref. 48, the capacitance is given by

$$\begin{aligned} C(d) =& 4\pi\epsilon_0 R \sum_{n=1}^{\infty} \frac{\sinh\alpha}{\sinh n\alpha}, \\ \alpha =& \cosh^{-1}\left[1 + \frac{d}{R} + \frac{h}{\epsilon_r R}\right]. \end{aligned} \tag{2.49}$$

The above model for capacitance was used for the work presented in this thesis. Prof. Roger F. Loring developed an improved model of the capacitance between a sphere and a

metal-backed dielectric slab,

$$\begin{aligned} C(d) &= 4\pi\epsilon_0 R \sum_{n=1}^{\infty} \eta^{n-1} \frac{\sinh \alpha'}{\sinh n\alpha'} \\ \alpha' &= \cosh^{-1}\left[1 + \frac{d}{R}\right] \\ \eta &= \zeta + (1-\zeta^2)\int_0^{\infty} du\, e^{-u}\left(\frac{e^{-\gamma u}}{1+\zeta e^{-\gamma u}}\right) \\ \zeta &= \frac{\epsilon_r - 1}{\epsilon_r + 1} \\ \gamma &= \frac{h}{d+R}. \end{aligned} \tag{2.50}$$

The above model has the advantage that it reduces to the analytically correct result in the limit of an infinitely thick film, i.e. $h \to \infty$. In this limit, $\eta = \zeta$. It was found that for the films studied, Eq. 2.49 and Eq. 2.50 did not differ significantly. To estimate the contribution of the cone to the tip-sample capacitance we employ a linear line charge density approximation [48]. Within this approximation, the cone has a constant line charge density λ_0,

$$\begin{aligned} \lambda_0 &= \frac{4\pi\epsilon_0 V_{\text{ts}}}{\beta} \\ \beta &= \log\frac{1+\cos\theta}{1-\cos\theta} \end{aligned} \tag{2.51}$$

where θ is the half-angle of the cone. The capacitance of the cone and its first and second derivatives are approximated by [48]

$$\begin{aligned} C^{\text{cone}} &\approx \frac{4\pi\epsilon_0 L}{\beta} \\ C_1^{\text{cone}} &\approx \frac{8\pi\epsilon_0}{\beta^2}\ln\frac{4d'}{L} \\ C_2^{\text{cone}} &\approx \frac{8\pi\epsilon_0}{\beta^2 d'} \\ d' &= d + \frac{h}{\epsilon_r} \end{aligned} \tag{2.52}$$

where L is the length of the cone and d' is the effective distance from the cantilever tip to the dielectric-metal interface.

2.4.1 Cantilever Frequency Noise due to Contact Potential Fluctuations

Having computed the static cantilever resonance frequency shift Δf_c induced by tip-sample interactions, we will now focus on time dependent, or fluctuating, frequency shifts $\delta f_c(t)$. First we will consider frequency shifts induced by a fluctuating contact potential $\phi(t) = \phi_c + \delta\varphi(z,t)$. The fluctuating potential $\delta\varphi(z,t)$ is assumed to act on an effective point charge, equal in magnitude to the total tip charge and located at a height above the interface z_{eff}, equal to the sum of z and a constant displacement. From Eq. 2.47, the time dependent Hamiltonian is

$$\delta W(z,t) \approx V_{\text{ts}}\, C(z)\, \delta\varphi(z_{\text{eff}},t), \tag{2.53}$$

where $V_{\text{ts}} = V_t - \phi_c$ is the tip-sample voltage. The resulting shift in the cantilever resonance frequency is given in Eq. 2.46. In a typical electric force microscope experiment, shifts in the cantilever resonance frequency are of the order of a few to hundreds of Hertz, much smaller than the resonance frequency, which is of the order of tens of kHz. This finding indicates that terms of order W are small (i.e. $\bar{W}_2 \ll k_c$) and it is therefore reasonable to drop the second, third, and fourth terms in Eq. 2.46, which are quadratic in W. We also note that the observed frequency shift is quadratic in tip-sample voltage, which further justifies keeping only the terms with linear dependence on W since $W \propto V_{\text{ts}}^2$. If the observed frequency shift is independent of cantilever amplitude, then one can also drop the last term in Eq. 2.46. The remaining term is the harmonic approximation to $\delta f_c(d,t)$ in Eq. 2.46,

$$\begin{aligned}\delta f_c(d,t) = \frac{f_c V_{\text{ts}}}{2k_c}\,(&C_2(d)\,\delta\varphi(d_{\text{eff}},t) - 2C_1(d)\,\delta\mathcal{E}_z(d_{\text{eff}},t) \\ &- C(d)\;\delta\mathcal{E}_{zz}(d_{\text{eff}},t))\end{aligned} \tag{2.54}$$

with $\delta\mathcal{E}_z(z,t) \equiv -\partial\delta\varphi(z,t)/\partial z$ the fluctuation of the electric field component along the probe coordinate and $\delta\mathcal{E}_{zz}(z,t) \equiv -\partial^2\delta\varphi(z,t)/\partial z^2$ the fluctuation in electric field gradient.

The coordinate of the effective point charge z_{eff} at $z = d$ is denoted d_{eff}. In Eq. 2.54, the probe frequency fluctuation is expressed as the sum of terms proportional to the electrostatic potential, to the electric field, and to the electric field gradient. From Eq. 2.7 and Eq. 2.13, the power spectrum of the frequency noise can be expressed in terms of equilibrium auto- and cross-correlation functions of these quantities,

$$\begin{aligned} P_{\delta f_c}(f) = \left(\frac{f_c V_{\text{ts}}}{2k_c}\right)^2 [&C_2^2(d)\, P_{\delta\varphi}(f) \\ &-4C_1(d)\, C_2(d)\, P_{z,\varphi}(f) - 2C(d)C_2(d)\, P_{\varphi,zz}(f) \\ &+ 4C_1^2(d)\, P_{z,z} - 4C(d)\, C_1(d)\, P_{z,zz}(f) \\ &+ C^2(d)\, P_{zz,zz}(f)]. \end{aligned} \tag{2.55}$$

In Eq. 2.55 the subscripts z and zz refer respectively to $\delta\mathcal{E}_z(d_{\text{eff}})$ and $\delta\mathcal{E}_{zz}(d_{\text{eff}})$. Eq. 2.55 can be written more compactly as

$$P_{\delta f_c}^{\text{sphere}}(f,d) = \frac{f_c^2(V_{\text{ts}}-\phi)^2}{4k_c^2}\partial_{z_1}^2\partial_{z_2}^2\left[C(z_1)\, C(z_2) P_{\delta\phi(z_1+d_{\text{eff}}-d),\delta\phi(z_2+d_{\text{eff}}-d)}(f)\right]|_{z_1=z_2=d}. \tag{2.56}$$

If the effective charge is located at the cantilever tip ($d = d_{\text{eff}}$), Eq. 2.56 simplifies to

$$P_{\delta f_c}^{\text{sphere}}(f,d) = \frac{f_c^2(V_{\text{ts}}-\phi)^2}{4k_c^2}\partial_{z_1}^2\partial_{z_2}^2\left[C(z_1)C(z_2) P_{\delta\phi(z_1),\delta\phi(z_2)}(f)\right]|_{z_1=z_2=d}, \tag{2.57}$$

The integrated frequency noise, or jitter J, is calculated by integrating the frequency noise spectra $P_{\delta f_c}(f,d)$ over a given frequency range.

Having computed frequency noise for a spherical cantilever tip, we now discuss a conically shaped cantilever tip. The contribution of a cone to the tip-sample capacitance can be approximated using a linear density of image charges at z' given a tip-sample distance z [48],

$$\lambda(z',z) = \lambda_0 u(z'-z), \tag{2.58}$$

$$\lambda_0 = \frac{4\pi\epsilon_0 V_{\text{ts}}}{\ln\dfrac{1+\cos\theta}{1-\cos\theta}} \tag{2.59}$$

where $u(z'-z)$ is the Heaviside step function and θ is the half-angle of the cone. The fluctuating tip-sample energy resulting from the interaction of a potential fluctuation with this charge density is

$$\delta W(z,t) = \int dz' \delta\varphi(z',t)\, \lambda(z',z). \tag{2.60}$$

We note that Eq. 2.60 is a more general form of Eq. 2.53. In fact, for the case of a single point charge located at $z = z_{\text{eff}}$, i.e. if $\lambda(z',z) = CV_{\text{ts}}\delta(z'-z_{\text{eff}})$, Eq. 2.60 reduces to Eq. 2.47. Within the harmonic approximation to $\delta W(z,t)$ given by the first term in Eq. 2.46, the fluctuating cantilever frequency generated by this interaction is

$$\delta f_c(d,t) = -\frac{f_c\lambda_0}{2k_c}\delta\mathcal{E}_z(d,t). \tag{2.61}$$

The resulting frequency power spectrum is

$$P_{\delta f_c}(f) = \left(\frac{f_c\lambda_0}{2k_c}\right)^2 \partial_{z_1}\partial_{z_2} P_{\delta\phi(z_1),\delta\phi(z_2)}(f)|_{d=z_1=z_2}. \tag{2.62}$$

We will see in Chapter 3 that the cone contribution to sample-induced frequency noise is in practice negligible compared to the contribution of the spherical cantilever tip.

In the calculations leading to Eq. 2.55 and Eq. 2.62, we have assumed that the cantilever only passively observes the fluctuations $\delta\varphi(t)$. In other words, we are assuming that the measurement does not affect the sample. If the measurements do affect the sample, then $\delta\varphi(t)$ is voltage dependent and the power spectra in Eq. 2.55 and Eq. 2.62 are no longer quadratic in V_{ts}. Conversely, a quadratic dependence of the observed frequency noise on V_{ts} indicates that the cantilever is only passively observing the sample and not altering the fluctuations it is aiming to measure.

2.4.2 Cantilever Frequency Noise due to Mechanical Vibrations

In order to analyze the contribution to measured frequency noise from external mechanical vibrations, we add to the equilibrium tip-sample separation d a stochastic fluctuation $\delta d_{\rm ex}(t)$, i.e $d \to d + \delta d_{\rm ex}(t)$. Making this substitution in Eq. 2.45 and linearizing in $\delta d_{\rm ex}(t)$ gives a frequency fluctuation quadratic in applied voltage,

$$\delta f_{\text{vib in z}}(d,t) = \frac{f_c}{2k_c}\overline{W}_3(d)\,\delta d(t) = -\frac{f_c}{4k_c}C_3(d)V_{\rm ts}^2\,\delta d(t). \tag{2.63}$$

Since these fluctuations are uncorrelated with the fluctuations in $\delta\varphi(z,t)$ considered previously, we can separately determine the contribution to the power spectrum from external vibrations. This power spectrum is proportional to the power spectrum of mechanical fluctuations in d and is given by [1, 49]

$$P_{\delta f_c}^{\text{vib in z}}(f) = \left(\frac{f_c C_3(d) V_{\rm ts}^2}{4k_c}\right)^2 P_{\delta d}(f). \tag{2.64}$$

In Figure 2.10 we show such vibration-induced frequency noise. Lateral mechanical fluctuations $\delta x(t)$ also lead to frequency noise. Proceeding as before, the frequency shift and frequency power spectrum are given by

$$\delta f_c^{\text{vib in x}}(d,t) = \frac{f_c}{2k_c}\frac{\partial\overline{W}_2(d)}{\partial x}\delta x_{\rm ex}(d,t) = \frac{f_c}{2k_c}C_2(d)V_{\rm ts}\frac{\partial\phi_c(x)}{\partial x}\delta d_{\rm ex}(d,t), \tag{2.65}$$

$$P_{\delta f_c}^{\text{vib in x}}(f) = \left(\frac{f_c C_2(d) V_{\rm ts} E_x}{2k_c}\right)^2 P_{\delta x_{\rm ex}}(f) \tag{2.66}$$

where $E_x = -\partial\phi_c(x)/\partial x$ is the electric field along x. From Eq. 2.66 it can be seen that in the presence of a lateral electric field, lateral mechanical vibrations lead to frequency noise.

2.4.3 Thermo-Mechanical Cantilever Frequency Noise

We have seen so far that both fluctuations in the contact potential $\delta\varphi(t)$ as well as mechanical vibrations affect the cantilever resonance frequency. There are other types of noise, such as

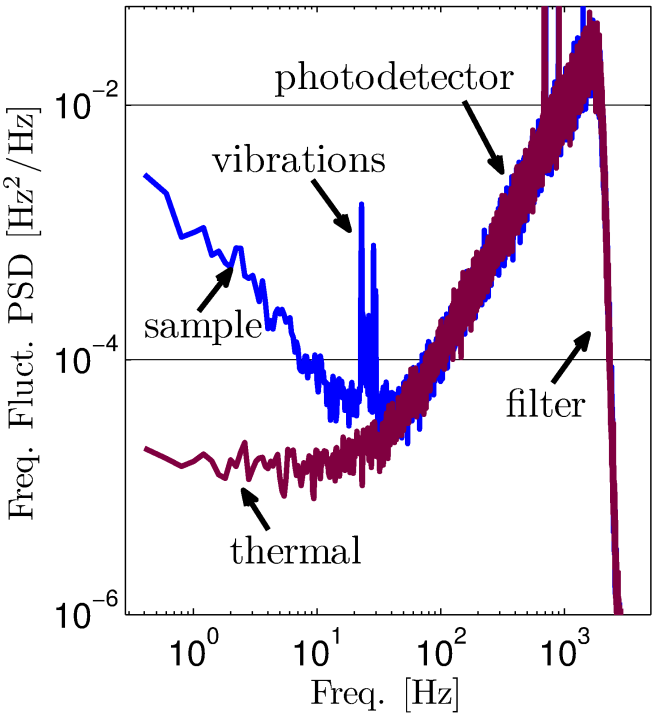

Figure 2.10: Various contributions to cantilever frequency noise at a height $d = 240$ nm over a 90 nm thick poly(vinylacetate) film at a tip sample voltage of $V_{\rm ts} = -1.9$ V (upper blue curve). The lower purple curve shows the frequency noise for $d = 90$ nm and $V_{\rm ts} = -0.1$ V. Also shown are the various contributions to the noise. In Chapter 3 we demonstrate that the low-frequency noise visible in the upper curve arises from fluctuations in the surface potential, which are generated by fluctuations in the electric polarization in the sample.

thermo-mechanical fluctuations and instrumentation noise, which do not alter the resonance frequency, but which instead obscure the measurement of the resonance frequency. These types of noise give rise to displacement noise, which results in noise in the observed cantilever resonance frequency. By adding a small amount of displacement noise $\delta z(t)$ to the cantilever oscillation, i.e. $z(t) = z_0 \cos(2\pi f_c t) + \delta z(t)$, taking a Hilbert transform to $z(t)$ in order to compute the resonance frequency $f(t)$, one can show that for $\delta z(t) \ll z_0$ the displacement noise and frequency noise are related by

$$P_{\delta f_c}(f) = \frac{f^2}{2z_{\text{rms}}^2} \left(P_{\delta z}(f_c + f) + P_{\delta z}(f_c - f)\right) \tag{2.67}$$

where $P_{\delta z}(f)$ is the power spectrum of the cantilever displacement z and $z_{\text{rms}} = z_0/\sqrt{2}$ is the root-mean-square cantilever displacement. The thermo-mechanical or Brownian motion spectrum $P_{\delta z}(f)$ in Eq. 2.39 is

$$P_{\delta z}^{\text{therm}}(f) = \frac{2k_B T}{\pi k_c Q f_c \left[\left(1 - \left(\frac{f}{f_c}\right)^2\right)^2 + \frac{f^2}{Q^2 f_c^2}\right]}. \tag{2.68}$$

In the limit $Q \gg 1$ and near the resonance frequency, i.e. $|f/f_c - 1| \ll 1$, we can approximate

$$P_{\delta z}^{\text{therm}}(f) \approx \frac{k_B T f_c}{2\pi k_c Q (f - f_c)^2}. \tag{2.69}$$

Substituting into Eq. 2.67, we see that the frequency dependence cancels and that the resulting frequency noise is given by [17, 38, 50, 51]

$$P_{\delta f_c}^{\text{therm}}(f) = \frac{k_B T f_c}{2\pi x_{\text{rms}}^2 k_c Q}. \tag{2.70}$$

We note that thermo-mechanical fluctuations result in white frequency noise, as shown in Figure 2.10. The prediction in Eq. 2.70 is typically within about 20% of the obsereved noise. Reasons for this deviation are an inaccurate estimate of the cantilever amplitude or of the cantilever spring constant, as discussed at the end of Section 2.3.

2.4.4 Cantilever Frequency Noise due to Noise in the Photodetector

Apart from thermo-mechanical fluctuations, the instrumentation also contributes to noise in frequency by injecting apparent displacement noise. The dominant contribution to this noise comes from the interferometer's photodetector. Assuming that the apparent displacement noise $P_{\delta z}^{\text{instr}}$ due to the photodetector is white at or near the cantilever resonance frequency, we calculate the resulting frequency noise from Eq. 2.67 to be [38, 52]

$$P_{\delta f_c}^{\text{instr}}(f) = \frac{f^2 P_{\delta z}^{\text{instr}}}{z_{\text{rms}}^2}. \tag{2.71}$$

The frequency noise scales as f^2, as shown in Figure 2.10. Let us now investigate if shot noise can account for the noise in Eq. 2.71. For simplicity, we assume that each incident photon generates current in the photodetector. By Shottky's theorem, the shot noise in the current is

$$P_I(f) = 2q\bar{I} \tag{2.72}$$

where $\bar{I}$ is the average current. The shot noise in Eq. 2.72 decreases with increasing current and that it is white. The current generated in the photodetector is read as a displacement $\Delta z(t) = G\Delta I(t)$. Because detector current and cantilever displacement are proportional to one another, we have from 2.71

$$P_{\delta f_c}^{\text{instr}}(f) = \frac{f^2 P_I^{\text{instr}}}{I_{\text{rms}}^2}. \tag{2.73}$$

We now approximate $\bar{I} \approx I_{\text{rms}}$, which amounts to equating the root mean voltage at the photodetector to the average voltage. Dropping factors of order one, we then have from Eq. 2.72,

$$P_{\delta f_c}^{\text{instr}}(f) \approx \frac{f^2}{\bar{r}} \tag{2.74}$$

where $\bar{r} = \bar{I}/q$ is the average rate of photons hitting the detector. For a laser wavelength of $\lambda = 1310$ nm and a power incident to the photodetector of $P = 3$ μW, we have

$$r = \frac{P\lambda}{hc} = 2 \times 10^{13} \text{ Hz} \tag{2.75}$$

where h is Planck's constant and c the speed of light. Comparing the predictions in Eq. 2.74 and Eq. 2.75 with the data in Figure 2.10, we see that shot noise is five orders of magnitude too small to account for the observed frequency noise.

2.5 The Sign of the Static Cantilever Frequency Shift

When computing frequency shifts, we have thus far assumed that the tip-sample voltage remains constant during a cantilever oscillation period. In this section we will drop this requirement and instead use Kirchoff's rules to determine how much charge moves on or off the cantilever. As before, we model the cantilever sample interaction with the tip-sample capacitance $C(z)$ where z is the displacement of the cantilever. A voltage source V_0 and a stray resistor R complete the circuit, as shown in Figure 2.11. The time dependence of the cantilever displacement $z(t)$ results in a time dependent tip-sample capacitance $C(t) = C_0 + \delta C(z(t))$. First we will investigate how fluctuations in capacitance result in both a fluctuating voltage $\delta V(t)$ and a fluctuating charge $\delta Q(t)$ at the tip-sample capacitor. We will then examine how the charge $\delta Q(t)$ alters the equations of motion of the cantilever.

From the definition of capacitance, the voltage and charge on the capacitor is

$$Q(t) = C(t)V(t). \tag{2.76}$$

In general, one should use $V(t) - \phi$ in place of $V(t)$ in the above equation where ϕ is the contact potential difference that arises for example when the work function of the cantilever is

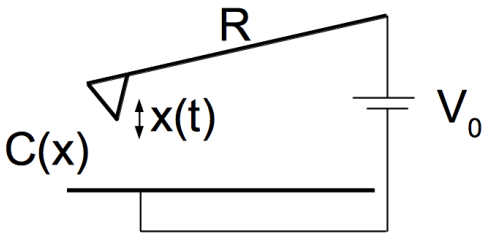

Figure 2.11: A sketch of the coupled oscillator. V_0 is the applied voltage, C the tip-sample capacitance, and R a stray resistance that together with C forms an RC-circuit.

different from that of the sample. In order to simplify the analysis, we set $\phi = 0$. Separating charge and voltage into time dependent and time independent parts, i.e. $Q(t) = Q_0 + \delta Q(t)$ and $V(t) = V_0 + \delta V(t)$ where V_0 the voltage applied by the voltage source, we have

$$Q_0 + \delta Q(t) = [C_0 + \delta C(t)]\,[V_0 + \delta V(t)]\,. \tag{2.77}$$

Keeping fluctuating terms to first order, we obtain

$$\delta Q(t) = V_0 \delta C(t) + C_0 \delta V(t). \tag{2.78}$$

Taking a Fourier transform (time dependance $\propto e^{2\pi i f t}$) and a time derivative, we have

$$\widetilde{\delta I} = 2\pi i f V_0 \widetilde{\delta C} + 2\pi i f C_0 \widetilde{\delta V}. \tag{2.79}$$

We can relate the current $\widetilde{\delta I}$ to $\widetilde{\delta V}$ by applying Kirchoff's laws. The voltage drop across the capacitor and resistor have to add up to the applied voltage V_0, or

$$(V_0 + \widetilde{\delta V}) + R\widetilde{\delta I} = V_0, \tag{2.80}$$

which implies that $\widetilde{\delta V} = -R\widetilde{\delta I}$. Substituting this expression into Eq. 2.79, we have

$$\widetilde{\delta V} = -2\pi i f V_0 R \widetilde{\delta C} - 2\pi i f R C_0 \widetilde{\delta V}. \tag{2.81}$$

or, upon rearranging,

$$\widetilde{\delta V} = V_0 \frac{-i\alpha}{1+i\alpha} \frac{\widetilde{\delta C}}{C_0} \tag{2.82}$$

where

$$\alpha = 2\pi f R C_0. \tag{2.83}$$

From Eq. 2.78 and Eq. 2.82, the fluctuating charge $\widetilde{\delta Q}$ is

$$\widetilde{\delta Q} = Q_0 \frac{1}{1+i\alpha} \frac{\widetilde{\delta C}}{C_0}. \tag{2.84}$$

Having established relationships between capacitance, voltage, and charge fluctuations, we now investigate how these fluctuations alter the equations of motion of the cantilever. The force between two conductors (i.e. the cantilever and the substrate) is given by [46, 53]

$$F = \frac{1}{2} C' V^2. \tag{2.85}$$

An equivalent expression was derived in Silveira's thesis [47] for the case where the potentials are held constant. Somewhat surprisingly, this expression is valid *no matter if the potentials are held fixed or not*. The force between the two plates arises from a Coulomb attraction between charges on the cantilever and charges on the conductor. This force depends on capacitance and charge only, and not on the external circuitry, such as the battery, the resistor, or anything else. Since $C' < 0$, the force is attractive, which makes physical sense because the cantilever and the conductor are oppositely charged.

Silveira showed that for fixed potentials, the energy with the *potential held fixed* is given by [47]

$$W = -\frac{1}{2} C (V - \phi)^2., \tag{2.86}$$

where ϕ is the contact potential. We see that for $\phi = 0$, the corresponding force $F = -W'$ is consistent with Eq. 2.85. If instead the *charges are held fixed*, the energy is

$$W = \frac{Q^2}{2C}. \tag{2.87}$$

The corresponding force $F = -W'$ is, once again, consistent with Eq. 2.85. We see that while the force is the same no matter if the potentials or charges are held fixed, the energy is of opposite sign in the two scenarios. Rewriting Eq. 2.85 in terms of the voltage $V(t) = V_0 + \delta V$ and charge $Q(t) = Q_0 + \delta Q(t)$ and keeping only the fluctuating terms to first order, we have

$$F(t) = \frac{1}{2}Q_0 V_0 + \frac{1}{2}Q_0 \delta V(t) + \frac{1}{2}V_0 \delta Q(t). \tag{2.88}$$

Taking a Fourier transform, and using Eq. 2.82 and Eq. 2.84 to eliminate δV and δQ in favor of δC, we obtain for non-zero frequencies ($f \neq 0$),

$$\widetilde{\delta F} = \frac{1}{2}Q_0 V_0 \frac{-i\alpha}{1+i\alpha}\frac{\widetilde{\delta C}'}{C_0} + \frac{1}{2}V_0 Q_0 \frac{1}{1+i\alpha}\frac{\widetilde{\delta C}'}{C_0}, \tag{2.89}$$

which simplifies to

$$\widetilde{\delta F} = \frac{1}{2}\frac{Q_0 V_0}{C_0}\frac{1-i\alpha}{1+i\alpha}\widetilde{\delta C}'. \tag{2.90}$$

Using a Taylor expansion of $\widetilde{\delta C}'$, i.e. $\widetilde{\delta C}'(\tilde{z}) \approx \widetilde{\delta C_0'} + \widetilde{\delta C_0''}\tilde{\delta z}$, we have

$$\widetilde{\delta F} = \frac{1}{2}Q_0 V_0 \frac{1-i\alpha}{1+i\alpha}\frac{C_0''}{C_0}\tilde{\delta z} \tag{2.91}$$

We proceed by investigating how the force $\widetilde{\delta F}$ alters the equations of motion of the cantilever. Modeling the cantilever as a harmonic oscillator with spring constant k_c, mass m_c, resonance frequency f_c, and friction Γ_c, we can write its equation of motion as

$$-m_c(2\pi f)^2\tilde{\delta z} = -k_c\tilde{\delta z} - 2\pi i f\Gamma_c\tilde{\delta z} + \frac{1}{2}Q_0 V_0 \frac{1-i\alpha}{1+i\alpha}\frac{C_0''}{C_0}\tilde{\delta z}. \tag{2.92}$$

Separating the real and imaginary parts and using $Q_0 = C_0 V_0$, the equation of motion near the cantilever resonance frequency ($f \approx f_c$) can be written as

$$-m_c(2\pi f)^2 \widetilde{\delta z} = -(k_c + \delta k_c)\widetilde{\delta z} - 2\pi i f(\Gamma_c + \delta\Gamma_c)\widetilde{\delta z} \tag{2.93}$$

where

$$\delta k_c = -\frac{1}{2} C_0'' V_0^2 \frac{1-\alpha_c^2}{1+\alpha_c^2} \tag{2.94}$$

$$\delta\Gamma_c = \frac{C_0'' V_0^2}{2\pi f} \frac{\alpha_c}{1+\alpha_c^2} \tag{2.95}$$

$$\alpha_c = 2\pi f_c RC. \tag{2.96}$$

From Eq. 2.95 it is evident that the external RC circuit increases the friction of the cantilever. Physically, the increased friction can be viewed as the energy dissipated in the resistor. The dissipated power across the resistor is proportional to the product of δV and δI and is maximized when $\alpha_c = 2\pi f_c RC = 1$.

The astute reader may wonder whether Johnson noise in the resistor will further increase cantilever friction. This effect is negligibly small. Johnson noise can be incorporated into the model with the substitution $V_0 \to V_0 + \delta V_J(t)$. Because Johnson-noise-induced voltage fluctuations $\delta V_J(t)$ do not depend of the displacement of the cantilever, Johnson noise enters the force on the cantilever only when multiplied with the distance dependent capacitance $\delta C'(z)$. Since $\delta C'(z) \cdot \delta V_J$ is small compared to $\delta C'(z) \cdot V_0$, we conclude that Johnson noise will not significantly alter the equation of motion of the cantilever.

We now relate the shift in the cantilever spring constant to the shift in its resonance frequency $f_c + \delta f_c$,

$$f_c + \delta f_c = 2\pi \sqrt{\frac{k_c + \delta k_c}{m}}. \tag{2.97}$$

To first order in the fluctuating terms, we have

$$\delta f_c = \frac{f_c \delta k_c}{2k_c}. \tag{2.98}$$

Applying Eq. 2.94, we arrive at

$$\delta f_c = -\frac{f_c C_0'' V_0^2}{4k_c} \frac{1-\alpha_c^2}{1+\alpha_c^2}. \tag{2.99}$$

Let's estimate δf_c and $\delta \Gamma_c$ in a typical electric force microscope experiment. Using typical tip-sample capacitance of $C_0 \approx 1$ aF, $f_c = 50000$ Hz, $C_0 = 10^{-18}$ F, $V_0 = 10$ V, and $R = 100\ \Omega$ (estimated resistance through the cantilever), we have

$$\begin{aligned} \alpha_c &= 2\pi f_c R C_0 \\ \alpha_c &= (2\pi\ 5000\ \text{Hz})(100\,\Omega)(10^{-18}\ \text{F}) \\ \alpha_c &= 10^{-11}. \end{aligned} \tag{2.100}$$

We are in the low-frequency limit since $\alpha_c = 2\pi f_c R C_0 << 1$. In this limit, Eq. 2.95 and Eq. 2.99 simplify to

$$\delta f_c = -\frac{f_c C_0'' V_0^2}{4k} \tag{2.101}$$

and

$$\begin{aligned} \delta\Gamma_c &= \frac{C_0'' V_0^2}{2\pi f_c} \alpha_c \\ \delta\Gamma_c &= C_0'' C_0 V_0^2 R. \end{aligned} \tag{2.102}$$

Physically speaking, the low frequency limit ($\alpha_c \ll 1$) corresponds to the case where the capacitor can easily charge or discharge within a cantilever cycle. Since the charge has ample time to equilibrate, we expect the tip-sample voltage (i.e. voltage across the capacitor) to be nearly constant in time (see Eq. 2.82) and equal the applied voltage V_0. In Figure 2.12, we plot the observed frequency shift versus voltage along with the prediction from Eq. 2.101. In agreement with Eq. 2.101, the frequency shift is negative (since $C_0'' < 0$) and quadratic in voltage.

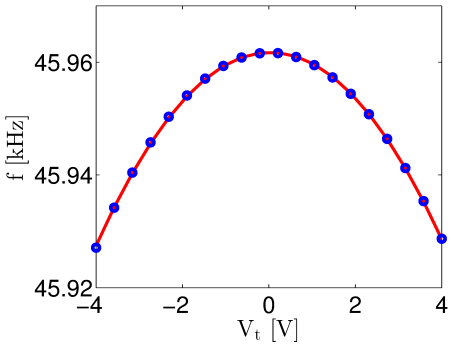

Figure 2.12: Observed cantilever frequency shift (circles) as a function of tip voltage 90 nm above a 63 nm thick metal-backed film of poly(vinylacetate), prepared as described in Chapter 3. Also shown is a fit to $A(V_t - \phi)^2 + B$ with $A = -2.1$ Hz/V^2, $B = 45.962$ kHz, and $\phi = -0.03$ V (solid line). From the fit we compute the second spatial derivative of tip-sample capacitance to be $C'' = -\frac{4Ak_c}{f_c} = 1.5 \times 10^{-4}$ F/m^2. Parameters: cantilever spring constant $k_c = 0.85$ N/m, resonance frequency $f_c \approx 46.0$ kHz, and tip radius $R = 40$ nm.

Let's determine if the predicted change in friction is observable. Estimating $C_0'' = 10^{-4}$ F/m^2, we have from Eq. 2.102

$$\begin{aligned} \delta\Gamma_c &= \frac{1}{2} C_0'' C_0 V_0^2 R \\ \delta\Gamma_c &= \frac{1}{2}(10^{-4}\text{ F/m}^2)(10^{-12}\text{ F})(10\text{ V})^2(100\,\Omega) \\ \delta\Gamma_c &= 5 \cdot 10^{-13}\text{ Ns/m}. \end{aligned} \tag{2.103}$$

The friction induced by the dissipation in the resistor is smaller than a typical thermally limited friction of $\Gamma_c = 10^{-11} Ns/m$ and can be neglected for most experiments.

Let's consider the high frequency limit, where $\alpha_c \gg 1$. In that case Eq. 2.95 and Eq. 2.99 simplify to

$$\delta f_c = \frac{f_c C_0'' V_0^2}{4k} \tag{2.104}$$

and

$$\delta\Gamma_c = \frac{C_0'' V_0^2}{(2\pi f_c)^2 RC}. \tag{2.105}$$

Interestingly, the frequency shift has the opposite sign of the frequency shift in the low frequency limit. In the high frequency limit, the capacitor does not have ample time to charge and discharge, so that we can assume that the charge on the capacitor is constant and equal to Q_0 (see Eq. 2.84). For this reason we refer to the limit $\alpha_c \gg 1$ as the constant charge limit. In this limit, the force on the cantilever in Eq. 2.85 reduces to

$$F(z) = \frac{Q_0^2}{2C'(z)}, \tag{2.106}$$

whereas in the constant voltage limit ($\alpha_c \ll 1$), we instead have

$$F(z) = \frac{1}{2} C'(z) V_0^2. \tag{2.107}$$

The force in the constant voltage and constant charge limits is of the same sign. Upon differentiating with respect to z, a negative sign is introduced in the constant charge, but not in the constant voltage limit. As a result the frequency shift is of opposite sign in the two limiting cases.

So far, the effects of stray capacitance, which is of the order of a few pF was ignored. It can be shown that the effects of stray capacitance (or any other capacitance added externally) can be ignored as long as the RC charging time associated with the stray capacitor is short compared with the cantilever period. One may attempt to move into a regime where $\alpha_c \ll 1$ and so change the sign of the resonance frequency shift by externally introducing a sufficiently large capacitor or resistor. However, in this case the DC tip sample voltage drop across the cantilever decreases substantially and so does the observable frequency shift. It may therefore be impossible to observe a change in the sign of the frequency shift by externally introducing

capacitors or resistors. Rather than adding external capacitors or resistors, one may wonder if it is possible to change to sign of the cantilever frequency shift by introducing an inductor L between the tip-sample capacitor and ground.

Rather than re-deriving the frequency shift and friction in the presence of the inductor from scratch, we start with Eq. 2.92 and introduce the inductor by making the substitution $R \to R+2\pi i f L$. This substitution amounts to replacing α_c by $\alpha_c+i\beta_c$ where $\beta = (2\pi f)^2 LC$. With this replacement, the frequency shift and friction are

$$\delta f_c = -\frac{f_c}{4k} C_0'' V_0^2 \frac{1-\beta_c^2-\alpha_c^2}{(1-\beta_c)^2+\alpha_c^2} \tag{2.108}$$

and

$$\delta\Gamma_c = \frac{C_0'' V_0^2}{2\pi f_c} \frac{\alpha_c}{(1-\beta_c)^2+\alpha_c^2}. \tag{2.109}$$

Let us consider the case where $\beta_c = LCf_c^2 = 1$, which is to say that the inductor and capacitor are tuned to the cantilever resonance frequency. For $C_0 \approx 1$ aF, $f_c = 5000$ Hz, this implies an inductance of $L = 10^6$ H, an unphysically large inductance. Proceeding anyway, the frequency shift and friction become

$$\delta f_c = +\frac{f_c}{4k_c} C_0'' V_0^2 \tag{2.110}$$

$$\delta\Gamma_c = \frac{C_0'' V_0^2}{(2\pi f_c)^2 RC} \tag{2.111}$$

Interestingly, these two expressions are equivalent to Eq. 2.104 and Eq. 2.105, which were obtained in the high frequency limit ($\alpha_c = 2\pi f_c RC \gg 1$). Eq. 2.110 and Eq. 2.111 are, however, valid at all frequencies. While we have shown that it is theoretically possible to change the sign of the frequency shift using an inductor, this scenario is in practice difficult to achieve due to the large inductance required.

Chapter 3

Dielectric Induced Frequency Noise

3.1 Introduction

Scanned probe microscopy has enabled nanometer-resolution imaging of surfaces with contrast based on topography [4], chemical forces [4–6], magnetization [5, 7], capacitance [8, 9], and electrostatic potential [8, 10]. Scanned probe microscopy also has the capacity to image a surface by probing dynamical fluctuations. Such fluctuations can be probed indirectly in measurements of sample-induced dissipation by applying the fluctuation-dissipation theorem. A charged Atomic Force Microscope (AFM) cantilever has been used to observe dissipation due to free and trapped carriers in semiconductors [11–13, 54], atomic defect motion at metal and semiconductor surfaces [14], and image currents in metals [15, 55]. A magnetic-tipped AFM cantilever has been used to probe dissipation associated with domain wall motion in ferromagnets [56, 57], eddy currents in metals [58, 59], and thermomagnetic fluctuations in submicron magnetic particles [60, 61]. Sample fluctuations also give rise to stochastic force gradients and, thereby, cantilever frequency noise.

In order to study the cooperativity of molecular motion near the glass transition, Israeloff and coworkers introduced the use of the charged tip of an AFM cantilever to observe *electric polarization fluctuations* in a thin polymer film [19–24]. In these experiments, a polymer sample is spun onto a conducting substrate, and the cantilever oscillates with its body parallel to the surface and its tip parallel to the sample's surface normal — the usual AFM geometry. The sample's polarization fluctuations lead to observable cantilever frequency noise which, they proposed, could be understood by considering the interaction of the charged cantilever

tip with voltage fluctuations arising from the sample.

Motivated by measurements of attonewton forces near surfaces [62], Kuehn *et al.* examined the force noise induced by thermal dielectric fluctuations in a thin polymer film acting on a charged cantilever [16, 63]. In these experiments — carried out with a custom-fabricated high-compliance silicon cantilever [64, 65] — the cantilever body is oriented parallel to the sample's surface normal, and the cantilever tip maintains a nearly constant tip-sample separation as the cantilever oscillates. A linear-response theory was developed, which quantitatively predicts the observed dependence of non-contact friction [16, 63] and frequency noise [17, 50] on the sample's complex dielectric function, the sample thickness, and the tip-sample separation. A key finding of this analysis was that, within a point charge model for the tip, frequency noise arises from a coupling of the cantilever's tip charge with electric field gradient fluctuations generated by the sample.

Here we extend our previous analysis [17, 50] of the interaction of a charged AFM tip with a dielectric surface to the case in which the tip moves perpendicular to the surface in the usual AFM geometry. In contrast to the case in which the tip moves parallel to the surface, we find that computing the cantilever frequency noise requires determining auto- and cross-correlations of stochastic fluctuations in voltage, electric field, and electric field gradient, with the dominant term containing the autocorrelation function of field gradient fluctuations. In the low-frequency limit, our analysis confirms the frequency dependence predicted by Israeloff and coworkers [19–24], but provides a complete quantitative description of the dependence of the power spectrum on experimental parameters. Here we probe dielectric fluctuations over poly(vinyl acetate) in the vicinity of 1 Hz at room temperature; these fluctuations have been assigned by bulk dielectric spectroscopy [66, 67] and NMR spectroscopy [68] as due to orientational dynamics of the polymer backbone, the α-relaxation associated with the

glass transition. We carry out systematic measurements of the power spectrum of cantilever frequency fluctuations as a function of frequency, tip-sample distance, and tip voltage using a commercial AFM cantilever over a thin poly(vinyl acetate) film. Our theory quantitatively describes these data; the only inputs to the calculation are the sample thickness, sample dielectric spectrum, and the diameter and cone angle of the cantilever tip. By connecting the information content of cantilever frequency fluctuations over a molecular sample to its dielectric spectrum, this work provides a basis for dielectric loss imaging over thin films.

3.2 Experimental Methods

For the electric force microscope measurements, we used a commercial cantilever (Mikro-Masch, NSC19 Ti/Pt) with resonance frequency $f_c \approx 46.0$ kHz and quality factor $Q \approx 2500$, as determined from ringdown measurements. The cantilever spring constant, $k_c = 0.85$ N/m, was obtained from its Brownian motion spectrum, as described in Chapter 2. The experiment was conducted in Physical Sciences Building, room B19, which has a lower vibration noise floor than Baker Lab 146 (see Chapter 2). More experimental detail on the elecric force microscope meaurements is provided in Chapter 2.

A polyvinyl acetate (PVAc) sample was prepared by dissolving 21.7 mg of PVAc (Sigma-Aldrich, no. 387924, used as received, $M_W = 140000$) in 2 mL of toluene and spin casting at 2000 rpm for 30 s onto a gold-covered silicon substrate. After spin casting, the sample was vacuum annealed for 12 h at 45°C to drive off water and any remaining solvent. The resulting sample thickness and rms-roughness were $h = 63$ nm and $h_{\mathrm{rms}} = 1.3$ nm, as measured by profilometry and atomic force microscopy, respectively.

To determine the dielectric spectrum of PVAc, a top contact of aluminum was thermally

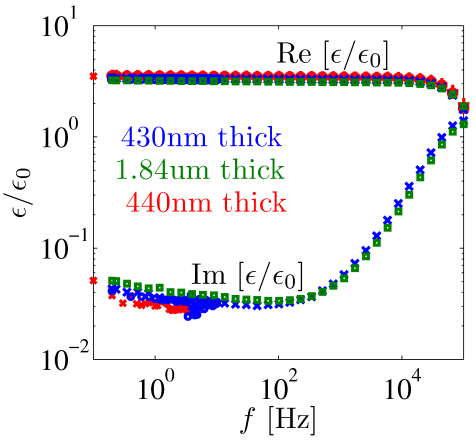

Figure 3.1: Dielectric spectrum of PVAc as determined by dielectric spectroscopy for a PVAc films of various thicknesses h. Reprinted with permission from Ref. [1]. Copyright [2011], American Institute of Physics.

evaporated over 1.4 cm^2 area of a PVAc film, and electrical contact was made by silver-paint. We performed impedance measurements on the resulting capacitor using a broadband dielectric spectrometer (Turnkey Concept N40). The observed dielectric function $\epsilon(f)$ in Figure 3.2 was determined from the observed capacitance, which is modeled as a parallel plate capacitor,

$$C = \frac{\epsilon(f)A}{h} \tag{3.1}$$

where A is the area of the capacitor and h the thickness of the insulating PVAc film, as determined by profilometry. This method is detailed in [40].

3.3 Calculating Dielectric-Induced Fluctuations in the Electrostatic Potential

The sample is represented as a continuum dielectric slab of thickness h and relative dielectric function $\epsilon(f)$, backed by a grounded conductor at $z = -h$, and the probe is taken to move in one dimension along z, perpendicular to the polymer-vacuum interface, as shown in Figure 3.2. An artist's rendering of the thermal dielectric fluctuations in the sample is shown in Figure 3.3. As discussed in Chapter 2, the tip-sample capacitance can be modeled by representing the tip as the superposition of a cone and a sphere (see Eq. 2.52 and Eq. 2.49). The contributions to cantilever frequency noise from sample-induced fluctuations in the electrostatic potential are calculated separately for a conical and spherical cantilever tip from Eq. 2.62 and Eq. 2.55, respectively, and added together. A key assumption in our calculation is the harmonic approximation, i.e. a quadratic dependence of the frequency noise on tip-sample voltage. As shown in Figure 3.7, the measured sample-induced frequency noise is, in fact, quadratic in V_{ts}, thereby validating the harmonic approximation.

Evaluation of the power spectra in Eq. 2.55 and Eq. 2.62 require calculating equilibrium correlation functions involving the potential, the electric field, and the electric field gradient as functions of distance above the sample surface in the absence of the charged probe. Previous studies in the Marohn group of noncontact friction [16, 63] and frequency jitter [17, 50] with a probe oscillating parallel to the surface required the calculation of autocorrelation functions of $\delta\mathcal{E}_x$ and $\delta\mathcal{E}_{xx}$. These quantities were determined from linear response theory along with two equivalent approaches: a quasistatic approximation to electrodynamics [16, 17, 50, 63] or a full electrodynamic calculation [17] in the limit as $c \to 0$. Here, we employ the quasistatic approximation of Refs. 16, 17, and 63. We consider the sample in the absence

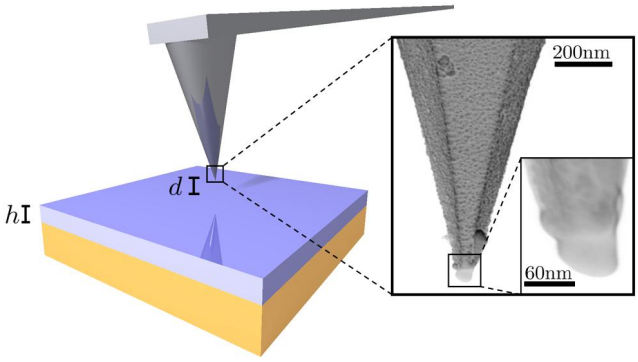

Figure 3.2: A charged cantilever tip is positioned a distance d above a dielectric sample of thickness h. Inset: A scanning electron microscope (SEM) image of the cantilever tip, from which we infer a tip radius of 40 nm. Reprinted with permission from Ref. [1]. Copyright [2011], American Institute of Physics.

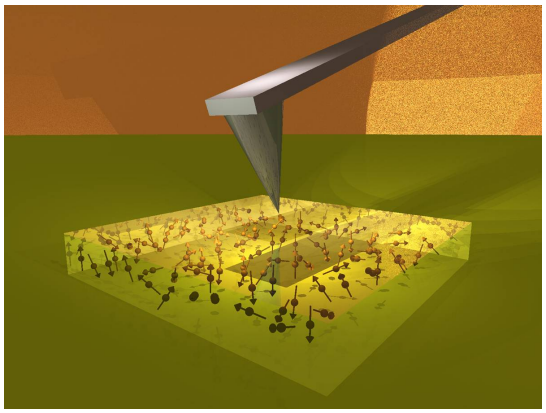

Figure 3.3: An artists rendering of thermal dielectric fluctuations in a thin-film sample along with the electric force microscope cantilever. Reprinted with permission from Ref. [1]. Copyright [2011], American Institute of Physics.

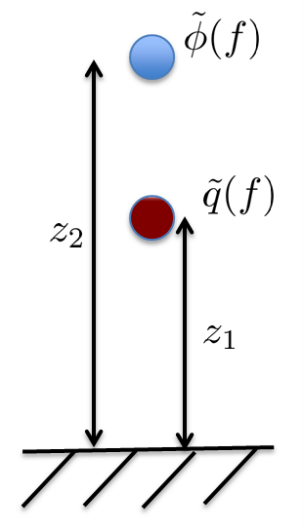

Figure 3.4: An artist's drawing of the electrostatic potential $\tilde{\phi}(z_2, f)$ induced by the sample due to the presence of a charge $\tilde{q}(z_1, f)$.

of the probe but with a fictitious time-varying point charge $q(t)$ at a distance z_1 above the interface. This perturbing charge is an artifice chosen because it couples to the fluctuating electrostatic potential generated by the sample $\phi(t, z_2)$, as sketched in Figure 3.4.

Classical linear response theory yields the following relation between the mean electrostatic potential at another location z_2, the magnitude and frequency-dependence of the perturbing point charge, and the correlation function of electrostatic potential fluctuations at different locations,

$$P_{\delta\phi}(z_1, z_2, f) \equiv 4 \int_0^\infty dt \cos(2\pi f t) \times \langle \delta\phi(z_1, t) \delta\phi(z_2, 0) \rangle \tag{3.2}$$

$$P_{\delta\phi}(z_1, z_2, f) = \frac{-4k_B T}{2\pi f} \mathrm{Im}\left(\frac{\tilde{\phi}(z_2, f)}{\tilde{q}(z_1, f)}\right) \tag{3.3}$$

$$\tilde{\phi}(z, f) \equiv \int_0^\infty dt e^{-i2\pi f t} \langle \phi(z, t) \rangle. \tag{3.4}$$

The autocorrelation function $P_{\delta\phi}(z_1, z_2, f)$ has a more general form than the correlation function $P_{\delta\phi}(z, f)$ in Eq. 2.55, which is restricted to the case $z_1 = z_2 = z$. The mean potential $\tilde{\phi}(z_2, f)$ in Eq. 3.3 is calculated in terms of the perturbing charge $\tilde{q}(z_1, f)$ from the quasistatic approximation to macroscopic electrodynamics for a linear dielectric using the method of images. This calculation yields an explicit expression for the power spectrum of potential fluctuations,

$$P_{\delta\phi}(z_1, z_2, f) = \frac{4k_B T \zeta''(f)}{(4\pi\epsilon_0)2\pi f} L_0(z_1, z_2, f) \tag{3.5}$$

$$\begin{aligned} L_n(z_1, z_2, f) = &\int_0^\infty ds s^n e^{-s(z_1+z_2)} \\ &\times \frac{1 - e^{-4sh}}{|1 + \zeta e^{-2sh}|^2} \end{aligned} \tag{3.6}$$

$$\zeta(f) = \frac{\epsilon(f) - 1}{\epsilon(f) + 1} = \zeta'(f) + i\zeta''(f). \tag{3.7}$$

The correlation functions required to compute the frequency noise for the case of a spherical cantilever tip (Eq. 2.56) may then be computed from Eq. 3.5 by taking coordinate derivatives, such as

$$P_{zz,zz}(f) = \frac{\partial^4}{\partial^2 z_1 \partial^2 z_2} P_{\phi,\phi}(z_1, z_2, f)|_{z_1=z_2=d_{\text{eff}}}. \tag{3.8}$$

As an alternative to the approach presented here, the correlation functions can also be calculated from a stochastic electrodynamics approach [17]. The starting point of this calculation is the relationship between polarization fluctuations and dielectric function, given by

$$\langle P_\alpha(\vec{q}', \omega') P_\beta(\vec{q}, \omega) \rangle = \delta_{\alpha\beta} \delta(\vec{q} + \vec{q}') \delta(\omega + \omega') \left[\frac{\epsilon''(\omega) k_B T}{\pi^3 \omega} \right]. \tag{3.9}$$

Using the dipole fluctuations in Eq. 3.9 and the boundary conditions for a dielectric slab backed by a conductor, one can use Maxwell's equations to compute the correlation functions of the the electric potential and derivatives of the electric potential. The result is identical to the one in Eq. 3.5. [17]

3.4 Calculating Dielectric-Induced Cantilever Frequency Noise

Having computed the correlation function of the electric potential in Eq. 3.5, we proceed by calculating the resulting frequency noise. For a spherical cantilever tip, the spectra are evaluated at the location of the effective point charge $z = d_{\text{eff}}$. From Eq. 2.55 the frequency noise is then given by

$$\begin{aligned} P_{\delta f_c}(f) = \frac{f_c^2 V_{\text{ts}}^2}{k_c^2} \frac{k_B T \zeta''(f)}{2\pi(4\pi\epsilon_0) f} \{ & C_2^2(d) K_0 - 4 C_2(d) C_1(d) K_1 \\ & + (2 C_2(d) C(d) + 4 C_1^2(d)) K_2 - 4 C(d) C_1(d) K_3 \\ & + C^2(d) K_4 \} \end{aligned} \tag{3.10}$$

with

$$K_m \equiv L_m(z_1, z_2, f)|_{z_1 = z_2 = d_{\text{eff}}}. \tag{3.11}$$

The power spectrum of probe frequency fluctuations arising from electrostatic interactions with the sample is seen in Eq. 3.10 to contain contributions from a variety of dynamical correlations. As shown in Eq. 2.54, the terms proportional to C_2^2, C_1^2, and C^2 are associated with autocorrelations of fluctuations in electrostatic potential, electric field, and electric field gradient, respectively. The remaining terms derive from cross-correlations among these fluctuations. In our previous study of ultrasensitive cantilevers oscillating parallel to the sample surface [50], only the autocorrelation function of field gradient fluctuations contributed to the probe frequency jitter since the capacitance could be assumed to remain constant over the course of the cantilever period. [50]

The cantilever frequency noise for a conical cantilever tip can be calculated in a similar fashion from Eq. 2.52 and Eq. 2.62 and from coordinate derivatives of Eq. 3.5. The resulting

jitter power spectrum is given by

$$P_{\delta f_c}(f) = \left(\frac{\lambda_0^2 f_c^2 k_B T \zeta''(f)}{k_c^2 4\pi\epsilon_0 (2\pi f)} \right) K_2$$
$$\lambda_0 = \frac{4\pi\epsilon_0 V_{\rm ts}}{\ln \dfrac{1+\cos\theta}{1-\cos\theta}} \tag{3.12}$$

with K_2 defined as in Eq. 3.11, but with $d_{\rm eff}$ replaced by d. We have computed the frequency noise in Eq. 3.12 and found it to be roughly two orders of magnitude smaller than the noise in Eq. 3.10. In contrast to the case of a spherical cantilever tip, the frequency noise of a conically shaped tip with uniform line charge does not depend on K_4, i.e. on electric field gradient fluctuations. Because $K_4 \gg K_2$, the contribution to frequency noise from a conical cantielver tip is negligible compared to that from a spherical tip. For this reason, the cone contribution is not included in Figure 3.9 and Figure 3.11.

Israeloff and coworkers [19–24] interpreted their measurements of cantilever frequency fluctuations over polymer films in terms of voltage fluctuations driven by polarization fluctuations in the sample. We next compare their analysis to our results given here. Their analysis is based on two steps: the relation of cantilever frequency fluctuations to voltage fluctuations, and the determination of voltage fluctuations from linear response theory. The power spectrum of cantilever frequency fluctuations is related to that of voltage fluctuations by Eq. 2 of Ref. 20, which in our notation is

$$P_{\delta f_c}(f) = \left(\frac{\partial \Delta f_c(d)}{\partial V_{\rm ts}} \right)^2 P_{\delta\phi}(f) \tag{3.13}$$

where $\Delta f_c(d)$ is the static cantilever frequency shift in Eq. 2.45. The result in Ref. 20 includes on the right-hand side of the equality a dimensionless factor G stated to be of order unity, which is omitted here. The power spectrum of voltage fluctuations is then related to the complex capacitance by Eq. (2) of Ref. 69, which in our notation is

$$P_{\delta\phi}(f) = -\frac{4kT}{2\pi f} {\rm Im} \left(\frac{1}{\tilde{C}(f)} \right). \tag{3.14}$$

We evaluate these two expressions for the point charge model of sample-tip interactions that we employ here. Our linear response expression in Eq. 3.3, when evaluated at $z_1 = z_2 = d_{\text{eff}}$ contains the voltage to charge ratio $\tilde{\phi}(d_{\text{eff}}, f)/\tilde{q}(d_{\text{eff}}, f)$. Equating this ratio to the inverse of the complex capacitance $1/\tilde{C}(f)$ reduces our Eq. 3.3 to Eq. 3.14. Substituting this result into Eq. 3.13 and evaluating the voltage derivative with Eq. 2.45 gives

$$P_{\delta f_c}(f) = \left(\frac{f_c V_{\text{ts}}}{2k_c}\right)^2 C_2^2(d) P_{\delta\phi}(f) \tag{3.15}$$

which is the first term in Eq. 2.55. However, our result in Eq. 2.55 also includes contributions to the jitter power spectrum from auto- and cross-correlations from fluctuations in electric field and electric field gradients. We show below that the contribution of the voltage fluctuations in Eq. 3.15 is small compared to other terms in Eq. 2.55. Our analysis is based on the same basic physical picture employed by Israeloff, *et al.*,[19–24] that states that cantilever frequency fluctuations are driven by dielectric fluctuations in the sample. However, our treatment generalizes the implicit assumption in Eq. 3.13 that in the limit of a point charge interaction, the tip couples only to fluctuations in electrostatic potential by including the coupling to fluctuations in gradients of the potential.

3.5 Results and Discussion

In Figure 3.5, we show the observed frequency noise spectra over PVAc for tip-sample distances $d = 90$ nm and $d = 240$ nm and for a range of tip voltages from -4 V to $+4$ V. Each of the frequency noise spectra in Figure 3.5 is generated by averaging twenty 5 s frequency transients (i.e. twenty 5 s long measurements of the cantilever frequency shift). The spectra show three distinct features: a $1/f$ component at low frequencies, spikes near 25 Hz, and a regime proportional to f^2 at large frequencies. The latter, which is only significant beyond

10 Hz, stems from noise in our instrumentation, primarily in the photo detector, and does not interfere with measurements of the frequency noise spectrum below 10 Hz. We are able to attribute this noise to our instrumentation because of its characteristic $\propto f^2$ frequency dependence [17, 38, 51] and because of it being independent of both tip-sample distance and tip voltage. By contrast, both the spikes near 25 Hz and the $1/f$ portion of the noise depend on the tip voltage and increase with increasing proximity to the sample. We conclude that these two sources of noise originate from an electrostatic tip-sample interaction. To quantify their voltage dependence, we integrate the power spectra in Figure 3.5 over a well defined frequency bandwidth. The result of this integration is a mean-squared frequency noise, which we shall henceforth call jitter. In Figure 3.7, we show jitter as a function of tip voltage for a range of tip-sample distances. In Figure 3.7A, we have integrated over the $1/f$ portion of the spectrum (0.4 Hz to 3 Hz) while, in Figure 3.7B, we have integrated over the noise spikes (23 Hz to 25 Hz). The jitter in these frequency regimes, which we designate as J_{L} for the $1/f$ regime and J_{H} for the noise spikes respectively, shows different voltage dependence. While J_{L} in Figure 3.7A scales as V_{ts}^2, a quartic voltage dependence V_{ts}^4 of J_{H} is shown in Figure 3.7B. In both panels of Figure 3.7, the respective voltage dependence is maintained for tip-sample distances ranging from 50 nm to 240 nm, a range over which jitter changes by three orders of magnitude. We conclude that there are two distinct processes responsible for the observed frequency noise in Figure 3.5 and Figure 3.7.

The quartic voltage dependence in Figure 3.7B suggests that the frequency noise is induced by stage vibrations as predicted in Eq. 2.64. To verify this interpretation, we measured the stage vibration spectrum, $P_{\delta d_{\mathrm{ex}}}(f)$, by laser interferometry. The vibration noise spectrum does, in fact, also show characteristic spikes near 25 Hz (Figure 3.6). To quantitatively test Eq. 2.64, we require the third spatial derivative of the tip-sample capacitance $C_3(d)$. Following Cherniavskaya *et al.* [48], we model the cantilever tip as a cone with a sphere at

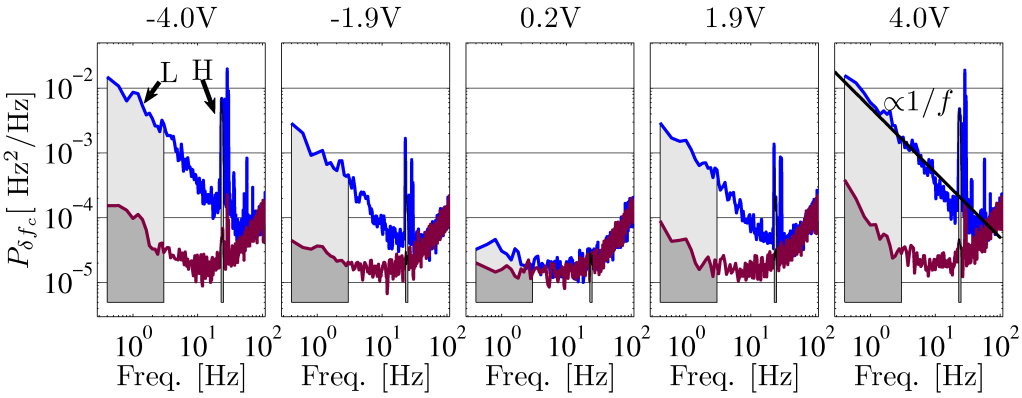

Figure 3.5: Frequency noise spectra for tip voltages ranging from −4 V to +4 V and tip-sample distances of $d = 90$ nm (upper line) and $d = 240$ nm (lower line). Each spectrum was generated by averaging 20 frequency transients, each lasting 5 s. A 1/f guideline is shown. Reprinted with permission from Ref. [1]. Copyright [2011], American Institute of Physics.

its tip (see Eq. 2.49 and Eq. 2.52). From scanning electron microscope (SEM) images as in Figure 3.2, we infer a tip radius of $R = 40$ nm. We validate the cone-sphere model by comparing the second derivative of the modeled $C(d)$ to the measured value we infer from Eq. 2.45. We extract from Eq. 2.45 the measured $C_2(d)$ using the known resonance frequency f_c, spring constant k_c, and measurements of resonance frequency as a function of tip-sample voltage. In Figure 3.8, we compare $C_2(d)$ from the cone-sphere model with the measured result for various tip-sample distances. We find that, for a cone half-angle of 16 deg, the measured $C_2(d)$ is in close agreement with the cone-sphere model. If we instead use the manufacturer's nominal value of 20 deg for the half-angle, the model slightly overestimates $C_2(d)$. We attribute this disagreement to the octagonal pyramid shape of the cantilever. Because a cone half-angle of 16 deg better reproduces the observed capacitance, we will use that angle to estimate $C_3(d)$ in Eq. 2.64 and to interpret the data in Figure 3.7B. The jitter data in Figure 3.7B can be fit to the form $J_{\mathrm{H}} = c\, V_{\mathrm{ts}}^4$, with c a constant. A predicted

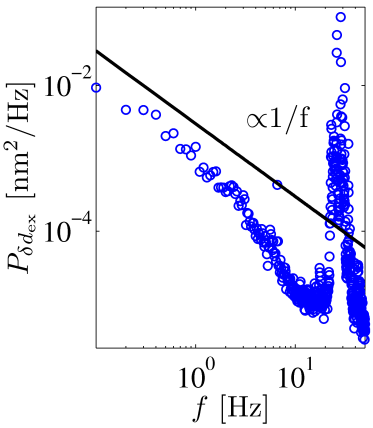

Figure 3.6: External mechanical vibration noise spectrum of the stage as measured by laser interferometry. Reprinted with permission from Ref. [1]. Copyright [2011], American Institute of Physics.

value for c can be determined from Eq. 2.64 by integrating the power spectrum $P_{\delta d_{\rm ex}}$ from 23 Hz to 25 Hz, and using the cone-sphere model predictions for $C_3(d)$. A comparison of the measured and predicted fit coefficients as a function of tip-sample distance is shown in the inset of Figure 3.8. From the data in Figure 3.7B, we see that Eq. 2.64 correctly predicts the distance dependence, $V_{\rm ts}$ dependence, frequency dependence, and magnitude of $P_{\delta f_{\rm ex}}$. The excellent agreement further validates the accuracy of the cone-sphere model.

Having identified the origin of the higher frequency jitter in Figure 3.7B as mechanical vibrations and having established the validity of our capacitance model, we return to the low-frequency jitter data in Figure 3.5 and Figure 3.7A. The observed noise at low frequencies is quadratic in voltage, as predicted by Eq. 3.10, and has a $1/f$ frequency noise spectrum [19–22, 50, 70]. Eq. 3.10 predicts the frequency dependence of the jitter spectrum from $\epsilon(f)$, the complex-valued relative dielectric function. In the low frequency limit, Eq. 3.10 yields a frequency spectrum proportional to $\epsilon''(f)/f$. Dielectric measurements of PVAc films shown

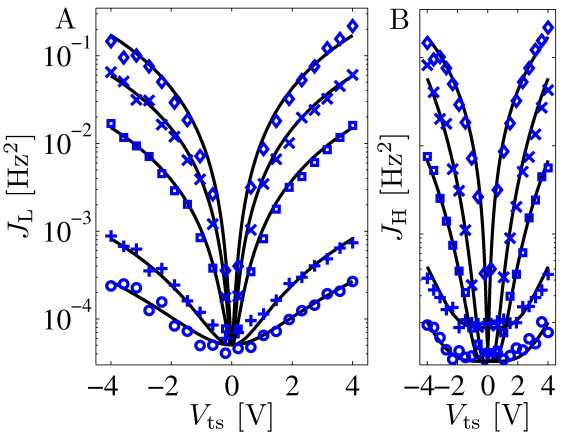

Figure 3.7: The frequency noise spectra in Figure 3.5 integrated from 0.4 to 3 Hz (A) and 23 to 25 Hz (B) as a function of tip voltage at various tip-sample separations (50 nm - ◊, 62 nm - ×, 90 nm - □, 180 nm - +, 240 nm - ○). Continuous curves are fit to $\propto V_{ts}^2$ (A) and $\propto V_{ts}^4$ (B), plus a noise floor. Reprinted with permission from Ref. [1]. Copyright [2011], American Institute of Physics.

in Figure 3.2 demonstrate that the dielectric spectrum $\epsilon''(f)$ is nearly constant over the frequency range 0.4 Hz to 3 Hz. For this case, Eq. 3.10 predicts a $1/f$ noise dependence, in agreement with the data in Figure 3.5. To test the distance dependence and the magnitude of the noise predicted by Eq. 3.10, we have measured jitter in a 0.4 Hz to 3 Hz bandwidth as a function of tip-sample separation d. At each distance point, we measured the resonance frequency versus voltage to determine the surface potential. We then applied a tip voltage of 3 V below the contact potential and averaged four 5 s long frequency transients to obtain jitter in a 0.4 Hz to 3 Hz bandwidth. Figure 3.9 compares these data to the predictions of Eq. 3.10 plus a thermal noise floor from Eq. 2.70. To calculate jitter from Eq. 3.10, we require the capacitance $C(d)$ and its first two spatial derivatives $C_1(d)$ and $C_2(d)$. Figure 3.8 demonstrates the validity of the cone-sphere model in representing $C_2(d)$. We find that the contribution to the jitter spectrum from the cone capacitance in Eq. 2.62 is negligible.

We therefore show in Figure 3.9 jitter calculations using only the sphere capacitance in Eq. 2.49. Evaluating Eq. 3.10 requires the dielectric function $\epsilon(f)$, and measured values are used (Figure 3.2). The tip-sample interaction is modeled in Eq. 3.10 by representing the tip charge as localized at a point with equilibrium tip-sample distance d_{eff}. The charge may be taken to be located between the lowest point on the tip and the sphere center, or $d < d_{\text{eff}} < d + R$. The resulting range of predictions is indicated by the shaded area in Figure 3.9, with the upper boundary of the shaded area indicating $d_{\text{eff}} = d$ and the lower boundary $d_{\text{eff}} = d + R$. The data are well represented by $d_{\text{eff}} \approx d$, which is most likely due to the cantilever's leading edge deviating from a spherical geometry (Figure 3.2). An alternative explanation is that, when summing over tip charge to compute the total jitter, the strong distance dependence of the fluctuating surface-induced potentials disproportionally weights the charges closest to the sample. In Figure 3.9, we also include a calculation of the lowest-order anharmonic correction to tip-sample interaction, which was computed from the terms in Eq. 2.46 that are linear in the applied voltage, and from Eq. 2.47, Eq. 2.7, and Eq. 2.13. This anharmonic correction term introduces a dependence on oscillation amplitude z_{rms}^2 and is given by

$$\begin{aligned} P_{\delta f_c}^{\text{anharm}}(f) =& \frac{z_{\text{rms}}^2}{2}[K_0 C_4(d) C_2(d) - K_1(2C_1(d)C_4(d) + 4C_2(d)C_3(d)) \\ &+ K_2(C(d)C_4(d) + 6C_2(d)^2 + 8C_1(d)C_3(d)) \\ &- K_3(4C(d)C_3(d) + 16C_1(d)C_2(d)) + K_4(7C(d)C_2(d) \\ &+ 8C_1(d)^2) - 6K_5 C(d)C_1(d) + K_6 C^2(d)]\}. \end{aligned} \tag{3.16}$$

In Figure 3.9 we show that the this term only represents a small correction to the frequency noise in Eq. 3.10 . To further test Eq. 3.16 and to assess the dependence of jitter on cantilever amplitude, we have measured jitter for a range of cantilever amplitudes with the tip held 90 nm from the surface. Figure 3.10 demonstrates that jitter does increase with amplitude and that the amplitude dependence is of the same order of magnitude as predicted by

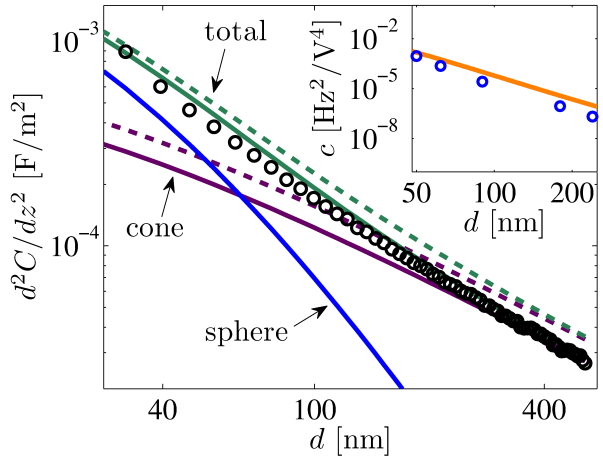

Figure 3.8: Observed second derivative of capacitance , C_2, versus tip-sample height ($\circ$). The solid lines are the predicted contributions from a 40 nm sphere, a cone with a half angle of 16 deg, and both sphere plus cone. The dashed lines show predictions for a cone angle of 20 deg. Inset: Fit coefficient c in $J_{\rm H} = c\, V_{\rm ts}^4$ from Figure 3.7B (circles) and prediction (line) from vibration noise determined by interferometry (Figure 3.5). Reprinted with permission from Ref. [1]. Copyright [2011], American Institute of Physics.

Eq. 3.16.

The jitter spectrum is decomposed in Eq. 2.55 into terms associated with auto- and cross-correlations among fluctuations in electrostatic potential, electric field, and electric field gradient. The jitter data (circles) and the calculation with $d_{\rm eff} = d$ (solid curve) from Figure 3.9 are reproduced in Figure 3.11. Also shown in Figure 3.11 are the contributions listed in Eq. 3.10 to the total calculated jitter. The power spectrum of the electric field gradient fluctuations is by far the dominant term whereas the contribution from voltage fluctuations is negligibly small. The contribution from voltage fluctuations is shown in Eq. 3.15 to result from applying the analysis of Israeloff and coworkers [20, 69] to our point charge model. The contribution from voltage fluctuations in Eq. 3.15 reproduces the frequency de-

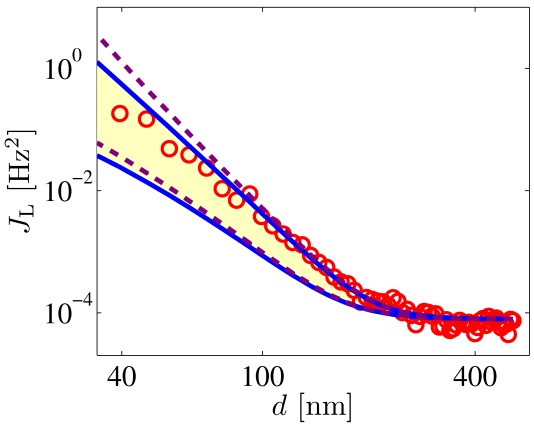

Figure 3.9: Measured jitter (∘) as a function of tip-sample height and the prediction from integrating Eq. 3.10 (solid lines). The bottom (top) solid line is based on the assumption that all of the charge is located at the center (bottom) of the sphere. The dashed lines include contributions from anharmonic tip-sample interactions. Reprinted with permission from Ref. [1]. Copyright [2011], American Institute of Physics.

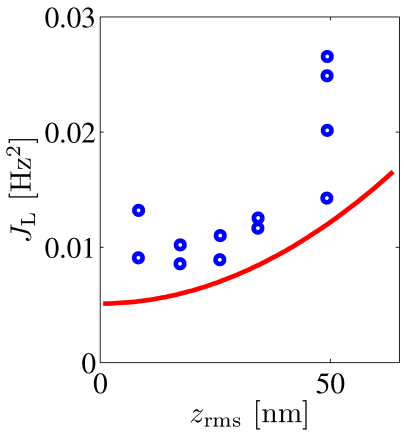

Figure 3.10: Observed low-frequency jitter (∘) as a function of cantilever amplitude 90 nm from the surface along with the prediction from Eq. 3.16 (solid line). Reprinted with permission from Ref. [1]. Copyright [2011], American Institute of Physics.

pendence $\epsilon''(f)/f$ of the complete jitter spectrum and has a comparable though not identical dependence on tip-sample separation. However, Figure 3.11 shows that this term is not the dominant contribution to the measured spectrum, which arises primarily from fluctuations in electric field gradient.

The measured jitter in Figure 3.9 was determined by integrating the frequency noise spectra in Figure 3.5 between 0.3 and 4 Hz, and the calculated jitter in Figure 3.9 was determined using measured dielectric spectra over the same frequency range to compute the frequency spectrum from Eqs. 2.49, 3.6, 3.7, 3.10, and 3.11. The agreement between calculated and measured jitter in Figure 3.9 demonstrates that cantilever frequency noise over a specified frequency range reflects dielectric fluctuations in the PVAc sample over that frequency range. The calorimetric glass transition temperature of high molecular weight PVAc is 300 K, [66] so that our PVAc sample is slightly below T_g. For the particular case of PVAc below its glass transition temperature, dielectric fluctuations in the frequency range 0.3 to 4 Hz arise from the α-relaxation process, [66] whose dramatic slowing down with temperature is associated with the glass transition. These dynamics in PVAc reflect cooperative, hindered reorientational motions of the polymer backbone. [68, 71] More generally, the agreement between calculated and measured jitter in Figure 3.9 shows that the cantilever frequency noise spectrum over a dielectric film probes the same molecular motions that contribute to the dielectric spectrum in the measured frequency range.

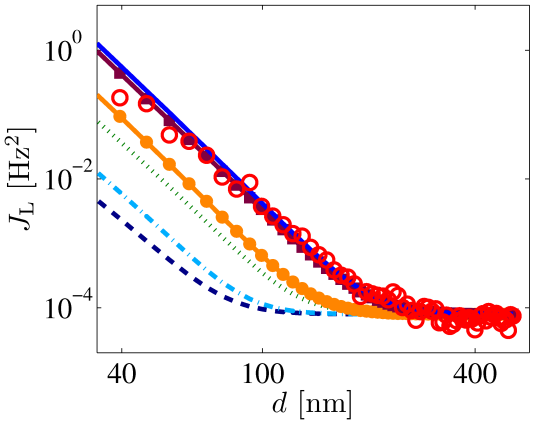

Figure 3.11: The jitter data (circles) and a calculation obtained by integrating Eq. 3.10 with $d_{\text{eff}} = d$ (solid curve). The contributions listed in Eq. 3.10 to the total calculated jitter are listed separately. In order of increasing magnitude, they are: a term proportional to K_0 (dashed line), terms proportional to K_1 (dot-dashed line), K_2 (dotted line), K_3 (solid line with $\circ$), and a term proportional to K_4 (solid line with $\square$). While K_0 arises from voltage fluctuations, K_1 arises from cross-correlations of the electric field and the voltage, K_2 arises from both the autocorrelation function of the electric field and cross-correlations between the electric field gradient and the voltage, K_3 arises from cross-correlations between the electric field and the electric field gradient, and K_4 is a contribution from the autocorrelation function of field gradient fluctuations. The latter is shown to be by far the dominant term and the contribution from voltage fluctuations is shown to be negligibly small. Reprinted with permission from Ref. [1]. Copyright [2011], American Institute of Physics.

Chapter 4

Light Induced Frequency Noise

4.1 Introduction

The highest efficiency organic solar cells demonstrated to date employ bulk heterojunctions created in phase-separated blends of conjugated polymers [72–74] or in blends of conjugated polymers and small molecules [72, 73, 75]. Optimizing vertical [76] and lateral [77] morphology of such bulk heterojunction solar cells is critical to achieving high device efficiency, yet detailed design rules for organic solar cells are still being debated and researched [73, 78–88]. Validating solar-cell design principles through independent microscopic measurements of the structure and function of bulk heterojunction films has been challenging [74]. Scanning probe microscopy has proved to be a valuable tool for the imaging of device *function* at submicron resolution [77, 89]. Scanning Kelvin probe microscopy, for example, has been used to image photovoltage [90–93]; time-resolved electric force microscopy has been used to study charge generation [92, 94, 95]; and photoconductive atomic force [77, 86, 96–101] and scanning photocurrent microscopy [102, 103] have been used to visualize transport networks. In addition, Raman microscopy [104], fluorescence microscopy [104], electron microscopy [104], and X-ray spectroscopy [105] have been used to image the structure of blends and determine the phase composition. Near-field scanning optical microscopy has been used to image exciton quenching and thereby map charge-carrier generation efficiency [106].

J. Luria probed *fluctuations* in the photoinduced carrier density in a bulk heterojunction solar cell film comprised of phase-separated poly(9,9-dioctyluorene-co-benzo-thiadiazole) (F8BT) and poly(9,9-dioctyluorene-co-bis-N,N-(4-butylphenyl)-bis-N,N-phenyl- 1,4-phenylene-

diamine) (PFB) by measuring light-induced cantilever frequency noise [3]. Here we present these meaurements along with a theory that quantitatively describes the frequency noise observed by this technique [3]. The theory is based on a charge trapping and detrapping model and relies only on a single free parameter, the occupation fraction of the trapping sites. We find that the trapping and detrapping model correctly describes the observed cantilever frequency noise spectra over a PFB:F8BT film as a function of irradiation wavelength, height, frequency, and tip voltage. From a comparison to the data, we are able to extract the occupation fraction of the trapping sites, equal to ≈ 0.995. In both the PFB-rich and the F8BT-rich phases, the observed fluctuation spectra track the absorption spectrum of F8BT, which demonstrates that F8BT absorption generates trap-clearing photocarriers in *both* PFB-rich and F8BT-rich regions. When combined with studies of photopotential [3], our findings suggest a microscopic mechanism by which intermixing of phases leads to charge trapping, a general efficiency-loss mechanism considered in previous analyses of intermixing [90, 107–109].

Charge-induced noise has been observed in other materials as well. Bulk voltage-noise measurements have been used to study trapping and detrapping fluctuations [110] and percolation transport [111] in organic semiconductor films while cantilever dissipation and frequency noise have been used to study charge blinking [112, 113], and generation-recombination noise in inorganic semiconductor heterojunctions [114]. Here we apply our charge trapping and detrapping model to the frequency noise observed near individual charge trapping sites in a InP/InGaAs heterostructure [38]. While our theory overestimates the observed noise by more than an order of magnitude, we are able to ascribe the discrepancy between theory and experiment to uncertainties in inputs to the theory, mainly the tip-sample distance, which was not reported in Ref. 38.

We also investigated the possibility of observing excitons, rather than trapped charge in an organic solar cell by watching cantilever frequency noise. Studying exciton motion in organic solar cells is important as the diffusion constant of the excitons forms a bottleneck for the performance in these devices. In order to estimate the size of the exciton-induced noise, we used a modified version of the charge trapping and detrapping model. We found that the frequency noise induced by excitons is many orders of magnitude too small to be observable in an electric force microscope experiment.

4.2 Fluctuations over a PFB:F8BT Film

4.2.1 Experimentally Observed Frequency Noise

Here we study a PFB:F8BT film — a prototypical bulk heterojunction solar cell material. Initial studies of device performance, luminescence, and topography as a function of blend ratio indicated that charge was generated at the interfaces between micron-scale PFB- and F8BT-rich domains in this film [107]. This conclusion was corroborated by an early scanning Kelvin probe microscopy study of photovoltage [90]. Subsequent work has called into question the simple picture that charge is generated at the apparent phase boundaries. Time-resolved electrostatic force microscopy (tr-EFM) [94] and photocurrent microscopy [103, 108] studies indicate that the majority of the photocurrent is instead generated in the center of the PFB- and F8BT-rich domains. X-ray microscopy studies [105] of PFB:F8BT films indicate significant intermixing of PFB and F8BT; the PFB-rich domain contains approximately 30% F8BT while the F8BT-rich domain contains 10% or less PFB.

Justin Luria has carried out spectroscopic measurements of surface photopotential *fluctu-*

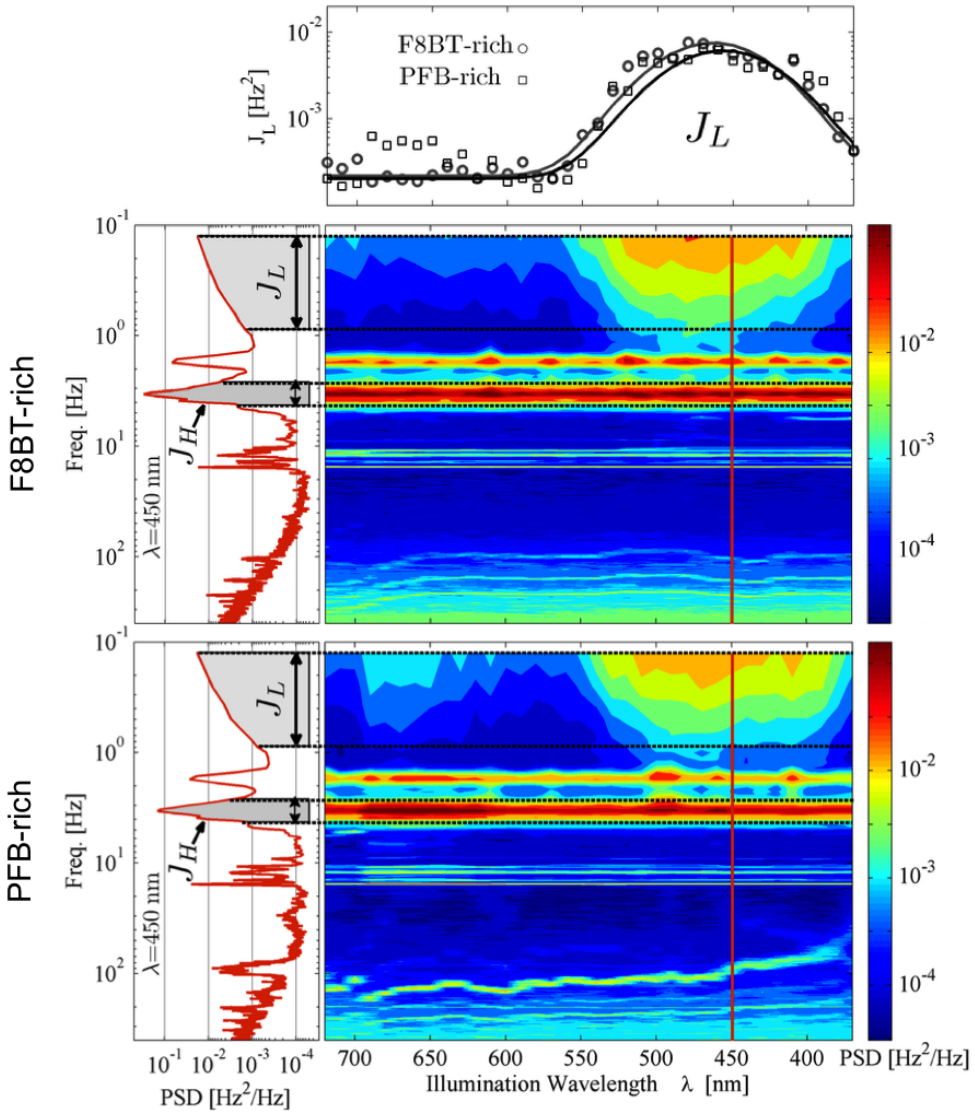

Figure 4.1: Power spectral density (PSD) of cantilever frequency fluctuations, $P_{\delta f_c}(f)$, versus illumination wavelength and frequency, f, recorded over a PFB-rich region (bottom-right panel) and over an F8BT-rich region (center-right panel). The panels on the left show the frequency noise spectrum at an illumination wavelength of 450 nm. The shaded areas in the left panels indicate the low-frequency (0.125 to 0.876 Hz) and high-frequency (2.63 to 4.25 Hz) fluctuations, J_L and J_H , respectively. Top panel: Low-frequency fluctuations, J_L, as a function of illumination wavelength over F8BT-rich (circles) and PFB-rich (squares). Parameters: $d = 90\,\text{nm}$, $z_{0\text{p}} = 15\,\text{nm}$, $V_{\text{ts}} + \phi = 5\,\text{V}$, and $N_{\text{avg}} = 30$. Adapted with permission from Ref. [3]. Copyright [2012], American Chemical Society.

ations over a PFB:F8BT film. Experimental details on the sample preparation, the Electric Force Microscope, and the sample illumination are listed elsewhere [3, 49]. The F8BT-rich and PFB-rich regions in the film were assigned by comparing surface potential images acquired over samples for various PFB:F8BT ratios. These surface potential images are already presented in detail in Refs. 49 and 3, and so will not be discussed further. To measure the photovoltage *fluctuations*, the cantilever was driven into self oscillation via positive feedback, and its instantaneous resonance frequency was recorded with sub-millisecond temporal resolution using a software frequency demodulator as described in Chapter 2. An instantaneous cantilever frequency deviation, $\delta f_c(t) = f_c(t) - f_c$, was computed and a one-sided power spectrum of cantilever frequency fluctuations calculated from Eq. 2.7. Power spectra of cantilever frequency fluctuations over F8BT-rich and PFB-rich regions were recorded as a function of irradiation wavelength. The resulting spectra exhibit low-frequency fluctuations ("J_L" in Figure 4.1), which show a strong wavelength dependence, and higher-frequency fluctuations ("J_H" in Figure 4.1), which are essentially wavelength independent.

To study the dependence of cantilever frequency fluctuations on irradiation wavelength, tip voltage, and distance, we will find it convenient to display an integrated frequency noise or "jitter":

$$J \equiv \int_{f_l}^{f_u} P_{\delta f_c}(f)\, df \tag{4.1}$$

where f_l and f_u are the lower and upper frequency cutoffs, respectively. To capture the low-frequency fluctuations in Figure 4.1, we set $f_l = 0.125\,\text{Hz}$ and $f_u = 0.876\,\text{Hz}$ and call the integrated frequency noise J_L. In a similar fashion, we set $f_l = 2.6\,\text{Hz}$ and $f_u = 4.2\,\text{Hz}$ for the jitter, J_H, associated with higher-frequency fluctuations. We will show later that these higher-frequency fluctuations are induced by vibrations in the sample stage. While vibrations are generated outside of this frequency regime as well, we found that vibrations in the 2.6

Hz to 4.2 Hz regime to be particularly reproducible. Under single-wavelength illumination, J_H is found to be proportional to $V_{\rm ts}^4$, while J_L is proportional to $V_{\rm ts}^2$ (see Figure 4.2). Since jitter is a function of the difference between tip voltage and contact potential, great care was taken to determine ϕ at each wavelength in Figure 4.1 and to adjust the tip voltage accordingly to keep $V_{\rm ts} - \phi = 5\,\mathrm{V}$.

In addition to measuring the dependence of frequency fluctuations on tip voltage, we also examined the dependence on the intensity and wavelength of illuminated light. As shown in Figure 4.3 the observed jitter depends linearly on light intensity at low power and saturates at high power. In Figure 4.1 we display frequency fluctuations versus wavelength and frequency over F8BT-rich and PFB-rich regions. The high-frequency jitter, indicated by J_H and the dashed lines, is wavelength independent. The low-frequency jitter J_L, in contrast, is strongly dependent on wavelength; near its peak at 460 nm, J_L in Figure 4.1 (top) is more than a factor of thirty above the background. The wavelength dependence of the low-frequency jitter J_L over *both* the F8BT-rich and the PFB-rich regions is well described by a single Gaussian with a width of approximately 35 nm and a center wavelength over F8BT-rich and PFB-rich regions of $\lambda_{\rm c}^{\rm F8BT} = 457 \pm 7\,\mathrm{nm}$ and $\lambda_{\rm c}^{\rm PFB} = 463 \pm 4\,\mathrm{nm}$, respectively. These peaks in the jitter spectrum correspond precisely to the low energy peak in the absorption spectrum of F8BT. We conclude that photovoltage fluctuations J_L are induced by light absorption in F8BT exclusively. In contrast, Brenner *et al.* [103] found that while photocurrent over both PFB-rich and F8BT-rich domains arose primarily from F8BT absorption, the PFB-absorption contribution to photocurrent was nevertheless substantial. The spectral shape of the photovoltage *fluctuations* in Figure 4.1 is also distinct from the spectral shape of the (time-averaged) photovoltage in Figure 4.4. We conclude that photovoltage *fluctuations* spectra contain information that is not captured in spectra of photovoltage or photocurrent.

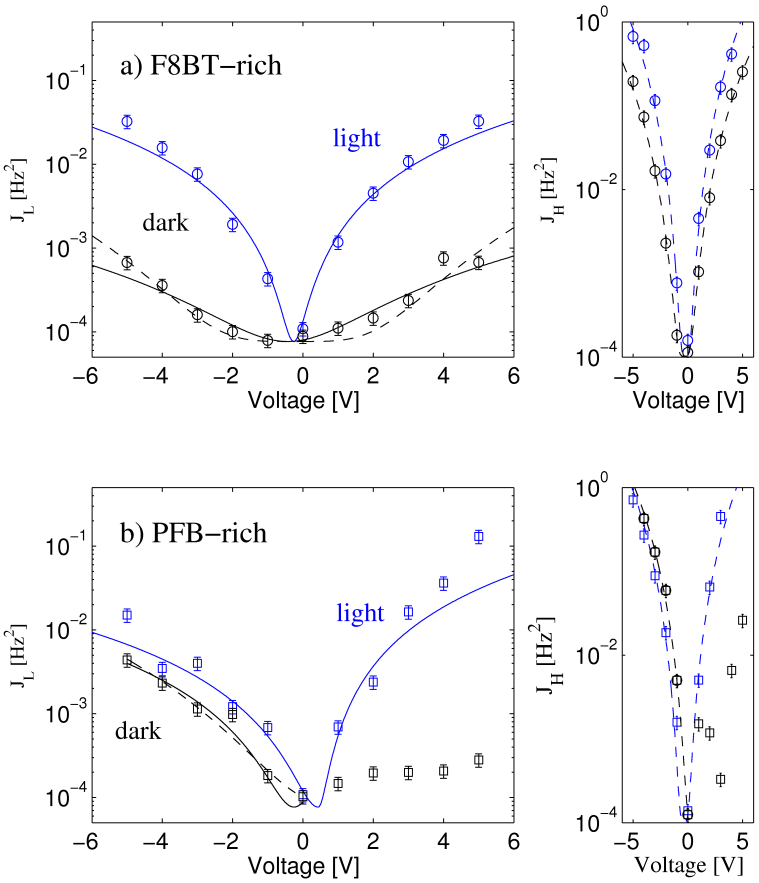

Figure 4.2: Cantilever frequency jitter versus tip voltage over (a) an F8BT-rich region (circles) and (b) a PFB-rich region (squares). Jitter at low frequency J_L and high frequency J_H is plotted on the left and right, respectively, under both illumination ($\lambda = 450\,\text{nm}$; blue, upper curves) and in the dark (black, lower curves). Data was fit to either a $J \propto V^2$ function (solid lines) or a $J \propto V^4$ function (dashed lines). Reprinted with permission from Ref. [3]. Copyright [2012], American Chemical Society.

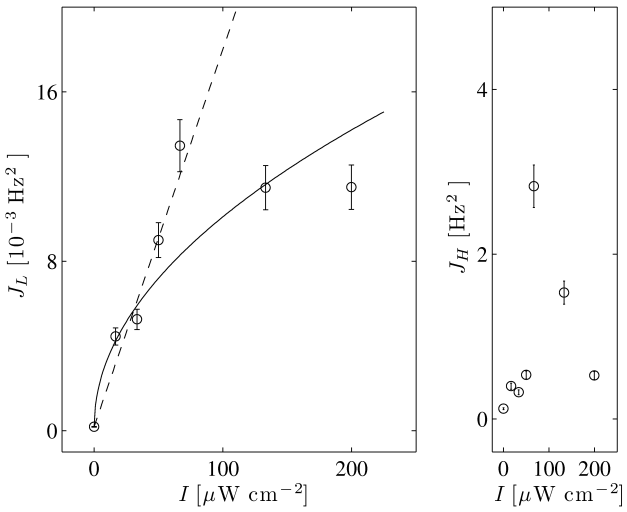

Figure 4.3: Jitter versus laser power 90 nm over the surface of an F8BT-rich region. The solid and dashed lines are fits to $J_0 + aI$ and $J_0 + b\sqrt{I}$, respectively, where $a = 0.18$ Hz^2/mW cm^{-2} and $b = 1.0$ Hz^{2}W$^{-\frac{1}{2}}$ cm. Up to an intensity of 30 μW/cm^2, which was used throughout this work, jitter scales nearly linearly with intensity. We note that the control J_{H} in the right panel, i.e. the vibration-induced frequency noise, is not independent of intensity. This finding suggests that there was some sort of drift, possibly in the tip-sample distance, during the course of the measurement. The intensity dependence in the left panel may be somewhat obscured by this drift. Reprinted with permission from Ref. [3]. Copyright [2012], American Chemical Society.

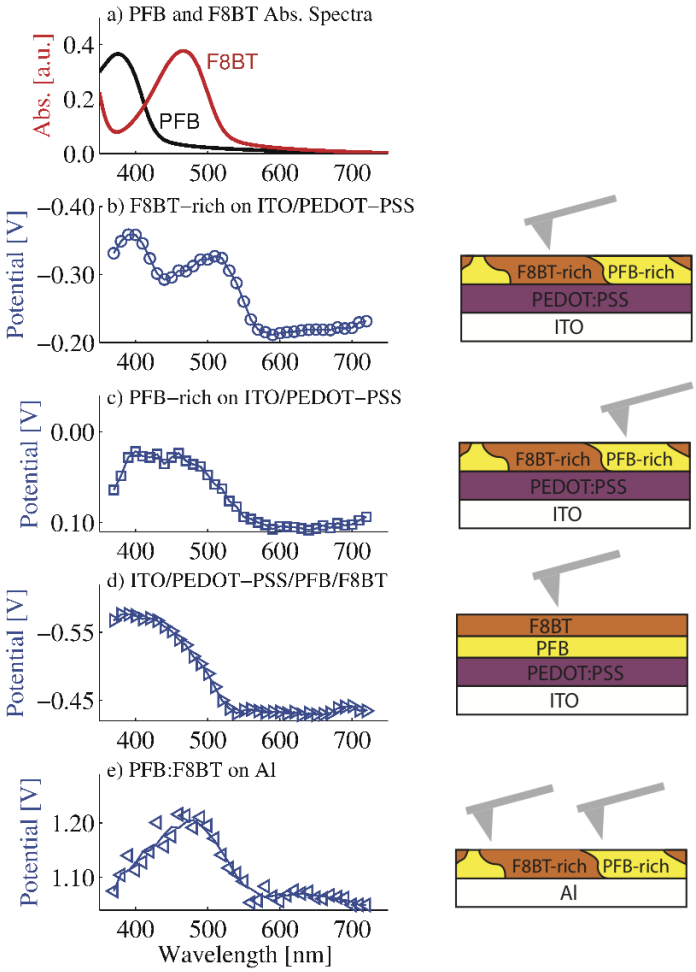

Figure 4.4: Mean contact potential and optical absorption *versus* illumination wavelength. (a) Optical absorption spectra of PFB (black; left) and F8BT (red; right) thin films. Surface photopotential spectra over PFB:F8BT films prepared on ITO/PEDOT-PSS: (b) photopotential spectrum of F8BT-rich regions (open circles) and (c) photopotential spectrum of PFB-rich regions (open squares); (d) photopotential spectrum over an F8BT/PFB bilayer film (right-pointing triangles); and (e) surface photopotential spectrum of a PFB:F8BT bulk heterojunction film prepared on an aluminum substrate (left-pointing triangles). We provide inset Figures to indicate whether donor-rich or acceptor-rich material is being measured. The y-axis has been inverted in (b-d) to facilitate comparing photopotential and absorption spectra. In the case of the aluminum substrate, (e), there is no contact potential contrast between the domains (see fFgure S7 in the Supporting information of Ref. [3]) and the y axis has not been inverted. Reprinted with permission from Ref. [3]. Copyright [2012], American Chemical Society.

4.2.2 Various Sources of Frequency Noise

Cantilever frequency noise is caused by a number of different sources. Here we discuss various sources of cantilever noise in order to explain the observed frequency noise in Figure 4.1. We demonstrate below that the low-frequency fluctuations ("J_L" in Figure 4.1) arise from charge trapping and detrapping in the sample while the higher-frequency spikes ("J_H" in Figure 4.1) are caused by sample vibrations [1]. The frequency fluctuations above 10 Hz arise from detector noise [1, 17, 50] and will not be discussed further.

Frequency Noise due to Charge Trapping

Previous work on F8BT:PFB solar cells has suggested the presence of trapped states, which manifest themselves as a slow decay of the potential in the dark [90]. We likewise observe a slow decay of photopotential over F8BT-rich regions in our sample (Figure 4.5), consistent with slow release of trapped electrons or, alternatively but less likely, slow recombination of electrons with holes in the substrate. In principle the light-induced frequency noise could arise from stochastic motion of free charge carriers (see Section 5.2.2). However, this picture cannot explain the slow decay of photopotential after the light is turned off. We expect most of free charge to diffuse to the electrodes essentially instantaneously after turning off the light source. By contrast, in Figure 4.5 we see that there is no measurable instantaneous change in the photopotential and that the decay of the potential is on the order of seconds to minutes, indicative of a slow release of traps. Moreover, noise due to stochastic motion of free charge is suppressed by charge interactions to the point where they become undetectable, as will be seen in Chapter 5. We do not believe that this suppresssion occurs in the charge trapping and detrapping model, which makes no assumption about interactions of the free

carriers, and expect screening of trapped charge by free carriers to be negligible becuase most charges in our device are trapped rather than free. We therefore regard charge trapping and detrapping as a more reasonable model. Here we develop a mathematical model that links noise from charge trapping to fluctuations in the surface potential and thereby to cantilever frequency noise. By Eq. 2.56, the cantilever frequency noise and fluctuations in the surface potential are related by

$$P_{\delta f_c}^{\text{sphere}}(f,d) = \frac{f_c^2 (V_{\text{ts}} - \phi)^2}{4k_c^2} \partial_{z_1}^2 \partial_{z_2}^2 \left[C(z_1) C(z_2) P_{\delta\phi(z_1),\delta\phi(z_2)}(f) \right] |_{d=z_1=z_2}, \tag{4.2}$$

where $C(z)$ is the capacitance of a spherical cantilever tip, given in Eq. 2.49. In Eq. 4.2 we have assumed that the charge on the cantilever can be treated as an effective point charge located at the cantilever tip, i.e. $d_{\text{eff}} = d$. We found that the contributions from a conically shaped cantilever tip (Eq. 2.62) to be negligible compared to the contribution in Eq. 4.2.

The frequency noise due to contact potential fluctuations in Eq. 4.2 is quadratic in tip-sample voltage V_{ts}, consistent with the observed quadratic tip-voltage dependence of J_L in Figure 4.2. The quadratic dependence of J_L on V_{ts} confirms an assumption made in Eq. 4.2, namely that the cantilever tip is passively observing the sample's electrostatic potential fluctuations. Control experiments also show that J_L is neither due to photoinduced changes in the tip sample capacitance (see Ref. 3, supporting information) nor due to fluctuations in the intensity of the light source, as will be seen in Section 4.2.2

We compute $P_{\phi_1,\phi_2}^{\text{single}}(f)$, the cross-correlation function of the electrostatic potential in Eq. 4.2, due to stochastic charge trapping and detrapping at localized sites. We use subscripts 1 and 2 to indicate that the potentials ϕ_i are to be evaluated at positions z_1 and z_2. The power spectrum of electrostatic potential fluctuations arising from a single trapping site is

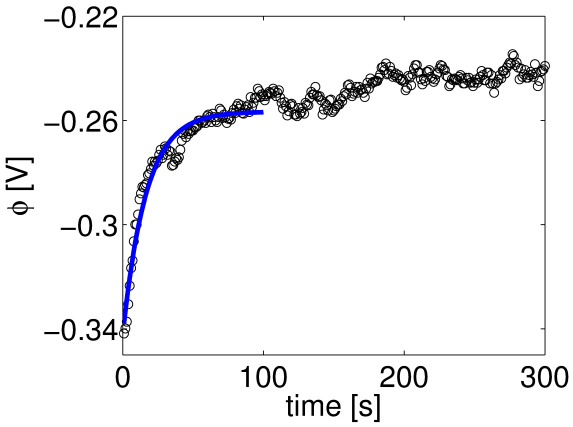

Figure 4.5: Potential decay over an F8BT-rich region after illumination is turned off (circles). A decay constant of 17 s was extracted from a fit of the data in the first 100 s to an exponential decay (solid line). An illumination intensity of 60 nW was used for this experiment. The illuminated spot is of elliptical shape with major and minor axes of 330 μm and 120 μm, respectively. Reprinted with permission from Ref. [3]. Copyright [2012], American Chemical Society.

that of a random telegraph signal, and is given by [115]

$$P^{\text{single}}_{\phi_1,\phi_2}(f) = \frac{4\phi_1\phi_2}{(\tau_f + \tau_v)(\tau^{-2} + 4\pi^2 f^2)} \tag{4.3}$$

where $\phi_i = \phi(\mathbf{r}, z_i)$ is the electric potential due to a filled trap, τ_f^{-1} and τ_v^{-1} are the rates associated with trapping and detrapping, respectively, and $\tau^{-1} = \tau_f^{-1} + \tau_v^{-1}$. Let us assume that the trapping and detrapping rates follow the Arrhenius law, i.e.

$$\tau_i^{-1} \propto e^{-E/k_B T}, \tag{4.4}$$

and let us further assume that there is not a single energy barrier E but a flat distribution of barriers between E_{low} and E_{high} whose rates bracket the observed frequency range: $\tau_{\text{low}}^{-1} \ll f \ll \tau_{\text{high}}^{-1}$. For a trapping site density per unit area of σ, the fluctuations in potential due to all the trapping sites in the film is

$$\begin{aligned} P_{\phi_1,\phi_2}(f) = &\frac{1}{E_{\text{high}} - E_{\text{low}}} \int_{E_{\text{low}}}^{E_{\text{high}}} dE \\ &\times \sigma \int d\mathbf{r} P^{\text{single}}_{\phi_1,\phi_2}(f). \end{aligned} \tag{4.5}$$

Performing the integral over energies, we find that the fluctuations in potential can be written as

$$P_{\phi_1,\phi_2}(f) = \frac{2\pi c_{\text{trap}} k_B T}{f(E_{\text{high}} - E_{\text{low}})} \int d\mathbf{r}\ \phi_2\phi_1 \tag{4.6}$$

where $c_{\text{trap}} \equiv \beta(1-\beta)\sigma$ and $\beta = \tau_f/(\tau_f + \tau_v)$ is the fraction of traps that are occupied. Assuming that the trapping sites lie below the Fermi energy, most traps are occupied, i.e. $\beta \approx 1$, and we can take c_{trap} to be the number of vacant traps per unit area, i.e. $c_{\text{trap}} \approx (1-\beta)\sigma$. The spectral shape of the frequency noise in Eq. 4.6 is $1/f$. If we had not assumed the distribution of barriers to be flat, the spectral shape of the noise would deviate from $1/f$. However, it can be shown from Eq. 4.4 and Eq. 4.5 that as long as the carrier density does not change substantially over an energy bandwidth $k_b T = 26$ meV, the spectral shape

of the noise is $1/f$ and the noise is still given by Eq. 4.6. If there were only a single energy barrier, and by implication only a singly trapping rate, then Eq. 4.6 is replaced by

$$P_{\phi_1,\phi_2}(f) = \frac{4}{(\tau_f + \tau_v)(\tau^{-2} + 4\pi^2 f^2)} \int d\mathbf{r}\ \phi_2\phi_1. \tag{4.7}$$

Eq. 4.7 is independent of frequency at low frequencies, and proportional to $1/f^2$ at high frequencies, with a fairly sharp transition between the two frequency regimes. The frequency dependence of the single barrier model in Eq. 4.7 is inconsistent with the observed $1/f$ dependence of the frequency noise in Figure 4.1. In order to explain the observed $1/f$ dependence, we need to assume a spread of energy barriers.

The integral over the xy-plane in Eq. 4.6 is most easily performed in Fourier space. From Appendix A, the Fourier transform of the electric potential of a point charge q is

$$\tilde{\phi}(k_x, k_y, z) = \frac{q}{2\epsilon_0 k} e^{-2\pi z k}. \tag{4.8}$$

Eq. 4.8 neglects screening due to free carriers, which one could include in a mean-field approach by applying the Poisson-Boltzmann relation to the field a of point charge. We expect such screening to be negligible because there are many more trapped than free charges. Taking a Fourier transform in x and in y of Eq. 4.6 and using Eq. 4.8, we have

$$P_{\phi_1,\phi_2}(z_1, z_2, f) = \frac{2\pi c_{\text{trap}} k_B T}{f(E_{\text{high}} - E_{\text{low}})} \int d\mathbf{k}\ \frac{q^2}{4\epsilon_0^2 k^2} e^{-2\pi(z_1+z_2)k}. \tag{4.9}$$

where z_1 and z_2 are the tip-sample distances at which the potentials ϕ_1 and ϕ_2 are to be evaluated. The integral in Eq. 4.9 is most easily done in polar coordinates. Integrating over the polar angle and changing variables $k' = 2\pi k$, we have

$$P_{\phi_1,\phi_2}(z_1, z_2, f) = \frac{2\pi^2 c_{\text{trap}} q^2 k_B T}{2\epsilon_0^2 f(E_{\text{high}} - E_{\text{low}})} \int_0^\infty \frac{dk'}{k'} e^{-(z_1+z_2)k'}. \tag{4.10}$$

We see that the integral diverges near $k' = 0$. The source of this divergence is that our model violates charge neutrality, and is therefore unphysical. The potential of a uniformly charged

plane diverges unless one introduces equal and opposite counter charges. In order to avoid divergences and to enforce charge neutrality, we assume that image charges are located at the bottom contact (i.e. ITO) of the solar cell. For a charge located a distance h' above the ITO, the potential of the image charge in the ITO is

$$\tilde{\phi}_{\rm im}(k_x, k_y, z) = -\frac{q}{2\epsilon_0 k} e^{-2\pi(z+\frac{2h'}{\epsilon_r})k} \tag{4.11}$$

where $2h'$ is the distance from the charge to its image charge and a factor of ϵ_r is introduced to account of the dielectric constant of the medium. Making the substitution $\tilde{\phi} \to \tilde{\phi} + \tilde{\phi}_{\rm im}$ in Eq. 4.6 and proceeding as before, we arrive at

$$P_{\phi_1,\phi_2}(z_1, z_2, f) = \frac{2\pi^2 c_{\rm trap} q^2 k_B T}{2\epsilon_0^2 f(E_{\rm high} - E_{\rm low})} \int_0^\infty \frac{dk'}{k'} e^{-(z_1+z_2)k'} \left(1 - e^{-\frac{2h'k}{\epsilon_r}}\right)^2. \tag{4.12}$$

From Eqs. 4.2 and 4.12 we find that the induced frequency noise for the sphere model can be approximated by

$$P_{\delta f_c}^{\rm trapping}(f, d) \approx \frac{\pi^2 c_{\rm trap} f_c^2 C^2 (V_{\rm ts} - \phi)^2 k_B T}{k_c^2 (E_{\rm high} - E_{\rm low}) f} \left(\frac{q}{4\pi\epsilon_0}\right)^2 J_4(d, \frac{2h}{\epsilon_r}) \tag{4.13}$$

with

$$J_n(d, \Delta) = (n-1)! \left[(2d)^{-n} - 2(2d + \Delta)^{-n} + (2d + 2\Delta)^{-n}\right] \tag{4.14}$$

where h is the thickness of the film. The corresponding expression for a conical cantilever tip is

$$P_{\delta f_c}^{\rm cone}(f, d) = \frac{\pi^2 c_a f_c^2 B^2 (V_{\rm ts} - \phi_s)^2 k_B T}{k_c^2 (E_2 - E_1) f} \left(\frac{q}{4\pi\epsilon_0}\right)^2 J_2(d, \frac{2d}{\epsilon_r}). \tag{4.15}$$

We found that a trap density per unit energy of $c_{\rm trap}/(E_{\rm high} - E_{\rm low}) = 10^{13}$ m^{-2}eV^{-1} is consistent with the magnitude of the observed frequency noise. Using a trap bandwidth of $E_{\rm high} - E_{\rm low} = 0.125$ eV [116], we find that the corresponding vacant trap density is $c_{\rm trap} = 1.25 \times 10^{12}$m^{-2}. Trapping throughout the film volume was also modeled by integrating Eq. 4.13 over the film (thickness $t = 200$ nm, dielectric constant $\epsilon = 3\,\epsilon_0$). The sphere radius

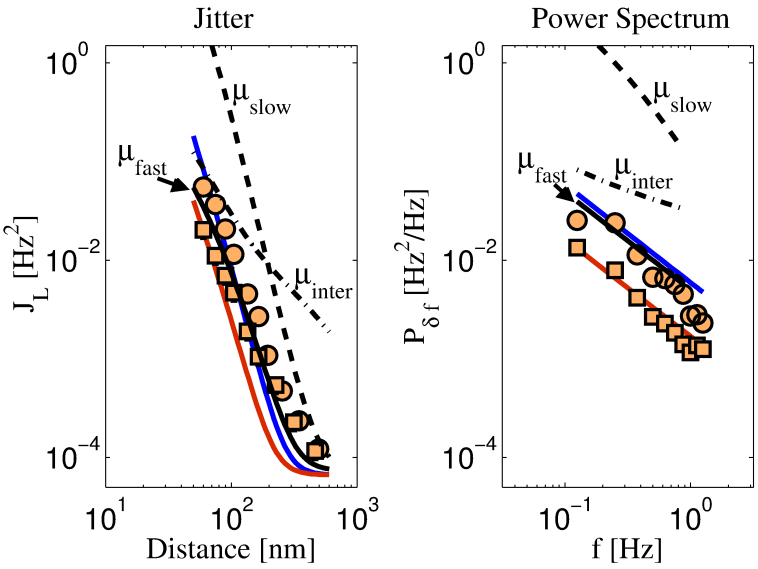

Figure 4.6: A comparison of observed and calculated low-frequency jitter J_L versus d (left) and the power spectrum $P_{\delta f_c}$ versus f at $d = 90$ nm (right). The data were acquired over an F8BT-rich region (circles) and a PFB-rich region (squares). The prediction from the trapping and detrapping model is shown for the case of charges distributed at the top of the film (Eq. 4.13; solid blue line). The solid blue line is a prediction from traps distributed throughout the volume of the film, which was obtained by integrating Eq. 4.13 over the noise from traps within a surface. Also shown is the frequency noise from a 2D sheet of non-interacting (or freely diffusing) charges, calculated from Eq. 5.36. The data were calculated for three different charge mobilities: $\mu_{\text{fast}} = 4 \times 10^{-7}$ cm^2/Vs (solid black line), $\mu_{\text{inter}} = 10^{-10}$ cm^2/Vs (middle dot-dashed black line), and $\mu_{\text{slow}} = 6 \times 10^{-14}$ cm^2/Vs (upper dashed black line). For the non-interacting charge diffusion model we used a charge density of $c_a = 2.5 \times 10^{14}$ m^{-2}, whereas for charge trapping we used a vacant trap density per unit energy of $c_a/(E_{\text{high}} - E_{\text{low}}) = 10^{13}$m^{-2}eV^{-1}. Adapted with permission from Ref. [3]. Copyright [2012], American Chemical Society.

and cone angle were taken to be 40 nm and 20 degrees, respectively. The sphere and cone capacitance were calculated as in Refs. 48 and 50. We can see in Figure 4.6 that the distance dependence and the frequency dependence of the cantilever frequency fluctuations are correctly predicted for both a uniform distribution of charges throughout the film and for charges distributed at the top of the film.

In order to compare the density c_{trap} necessary to reproduce the data to the density of photoinduced charge $\Delta\sigma_{\text{light}}$, we modeled F8BT/PFB as a uniformly charged film with a sheet of counter charge present in the underlying ITO/PEDOT:PSS. In this approximation, the concentration of photoinduced charge is related to the observed photopotential $\Delta\phi_{\text{light}}$ by $\Delta\rho_{\text{light}} = 2\epsilon_s\Delta\phi_{\text{light}}/q_e t^2$, with $t = 200$ nm the sample thickness, ϵ_s the sample dielectric constant, and q_e the charge of the carrier. Taking $\epsilon_s = 3\epsilon_0$ and $\Delta\phi_{\text{light}} = 0.15$ V, we estimate $\Delta\rho_{\text{light}} \approx 1.2 \times 10^{21}\,\text{m}^{-3}$. The corresponding planar density of photoinduced charge is $\Delta\sigma_{\text{light}} = \Delta\rho_{\text{light}} t = 2.5 \times 10^{14}\,\text{m}^{-2}$, and corresponds with estimates from literature [91]. From this estimate we conclude that the fraction β of occupied traps is $\beta \approx 0.995$.

Having established charge trapping and detrapping as a plausible explanation for frequency noise, we now discuss the details of the trapping mechanism. It is observed that over both F8BT-rich and PFB-rich regions the spectral shape of the frequency fluctuations in Figure 4.1 tracks the absorption of F8BT exclusively, indicating that the noise in both regions arises from traps populated and depopulated by photocarriers generated by F8BT absorption. Electron traps agree with the qualitative picture in Figure 4.7 and seem to us a more reasonable hypothesis than hole traps. Figure 4.7(d-e) illustrates how illumination of F8BT, but not PFB, results in photoinduced trapping and detrapping. The key hypothesis is that electrons are trapped in F8BT — in PFB-rich regions, these trapped electrons are cleared by recombination with an F8BT exciton; a PFB exciton simply cannot get into close

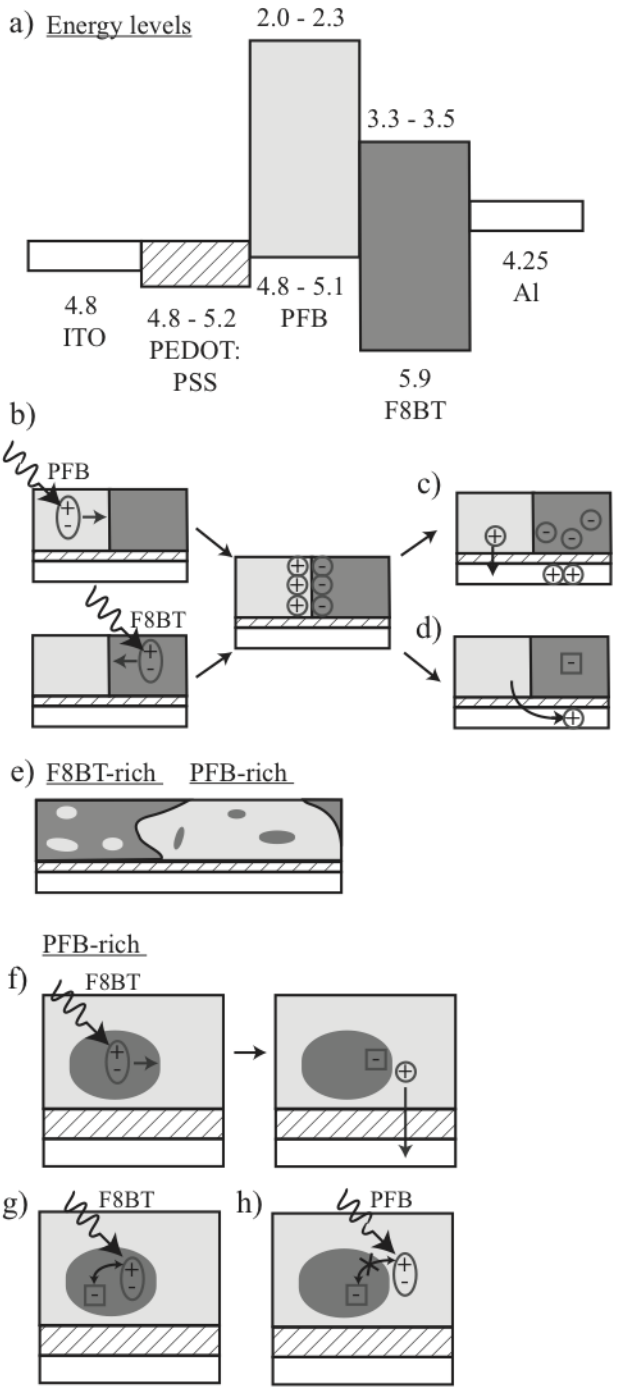

Figure 4.7: ITO/PEDOT:PSS/PFB:F8BT under illumination: (a) Energy level diagram of ITO/PEDOT:PSS/PFB:F8BT/Al. (b)-(e) Scenarios which attempt to explain the negative sign of the photovoltage in Figure 4.4. (b) We first consider pure phases of PFB and F8BT in contact with one another. Excitons (ovals) generated by light absorption in either PFB (light grey) or F8BT (darker grey) lead to separated charges (circles) at the interface. (c) A scenario in which an electron excess is generated in the F8BT phase due to a disparity in the electron and hole extraction rates. Image charges and image dipoles have been omitted for clarity. (d) An alternative scenario in which an excess of electrons in F8BT arises due to trapped electrons (squares) in the F8BT phase. (e) A sketch of a bulk heterojunction containing a phases of mixed composition. (f) Photoexcitation of a minority F8BT inclusion in the PFB-rich phase. Photoinduced detrapping (and subsequent retrapping; not shown) of electrons in F8BT inclusions is facilitated by photoexcitation of (g) F8BT but not (h) PFB. Reprinted with permission from Ref. [3]. Copyright [2012], American Chemical Society.

enough proximity to clear the trapped electrons in the F8BT inclusions. The spectra of Figure 4.1 indicate that the concentration of trapped electrons in F8BT is roughly equal in both the PFB-rich and F8BT-rich domains over ITO/PEDOT:PSS.

Frequency Noise due to Mechanical Vibrations

Mechanical vibrations in the sample stage can induce fluctuations in the tip-sample distance d. These fluctuations in turn lead to cantilever frequency noise. By Eq. 2.64 vibration-induced frequency noise is quartic in tip-sample voltage and is given by

$$P_{\delta f}^{\text{vib in d}}(f) = \left(\frac{f_c C_3(d) V_{\text{ts}}^2}{4k_c}\right)^2 P_{\delta d}(f) \tag{4.16}$$

$$P_{\delta f}^{\text{vib in d}}(f) \propto (V_{\text{ts}} - \phi)^4 \tag{4.17}$$

with f_c the cantilever resonance frequency, k_c its spring constant, C the tip-sample capacitance, and $P_{\delta f}^{\text{vib in d}}$ the power spectrum of tip-sample distance fluctuations. The quartic voltage dependence of mechanical noise provides a means of distinguishing it from noise induced by a fluctuating contact potential, which scales quadratically in tip-voltage.

The quartic voltage dependence of the high frequency noise J_H shown in Figure 4.2 indicates that J_H is due to mechanical vibrations. This conclusion is corroborated by the fact that J_H in Figure 4.1 is independent of the illumination wavelength λ. The absence of a systematic dependence of J_H on λ demonstrates that the wavelength dependence of J_L is not due to a failure to accurately track ϕ.

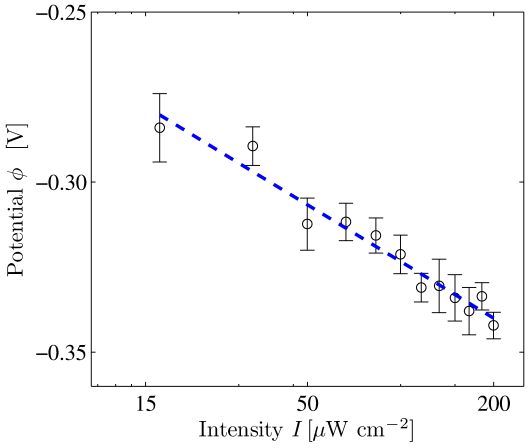

Figure 4.8: Contact potential versus laser power over an F8BT-rich region. The dashed line is a fit to $\phi_0 + A \log\left(I/(\mu\text{W cm}^{-2})\right)$, where $A = (-0.025 \pm 0.004)$ V and $\phi_0 = (-0.21 \pm 0.02)$ V. Reprinted with permission from Ref. [3]. Copyright [2012], American Chemical Society.

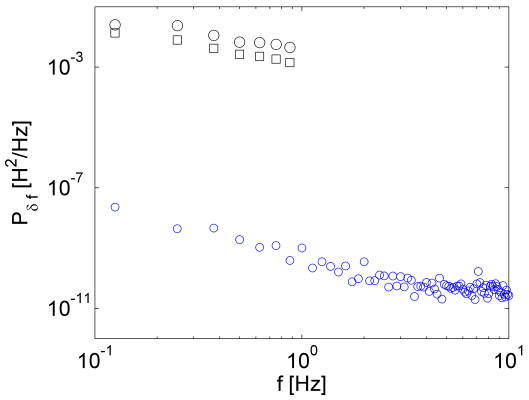

Figure 4.9: Frequency noise spectra predicted from the observed intensity fluctuations at 50 μW/cm^2 (blue circles) and the observed frequency noise over F8BT (black circles) and PFB (black squares). Parameters: $V_{\text{ts}} - \phi = 5$ V. From the data in Figure 4.8 we have estimated $d\phi/dI = 0.73 \cdot 10^{-3}$ V cm$^2/\mu$W at an incident light intensity of $I_0 = 50$ μW/cm^2. The coefficient $\alpha \approx 0.5$ Hz/V^2 was estimated from Ref. [3] (Supplementary Figure S9). Reprinted with permission from Ref. [3]. Copyright [2012], American Chemical Society.

Frequency Noise from Noise in the Light Source Intensity

The observed frequency noise could, in principle, also originate from fluctuations in the intensity of the light source. From Figure 4.8, we see that light intensity and contact potential are linked. Fluctuations in light intensity may therefore contribute to contact potential fluctuations and so lead to frequency noise. To estimate the size of this contribution we have measured the intensity fluctuations $\delta I(t)$, which are related to potential fluctuations $\delta\phi(t)$ by

$$\delta\phi(t) = \frac{d\phi}{dI}\delta I(t) \tag{4.18}$$

where $d\phi/dI$ can be determined from the data in Figure 4.8. From Eq. 2.48 it follows that a shift in potential lead to a frequency shift of

$$\delta f(t) = 2\alpha(V_{\text{ts}} - \phi)\delta\phi(t), \tag{4.19}$$

where $\alpha = \frac{f_c}{4k_c}C_2(d)^2$ is the curvature of a graph of frequency versus voltage, a quantity which can be determined experimentally. Combining Eqs. 4.18 and 4.19 and taking the power spectrum, we have

$$P_{\delta f}(f) = 4\alpha^2(V_{\text{ts}} - \phi)^2 \left(\frac{d\phi}{dI}\right)^2 P_{\delta I}(f). \tag{4.20}$$

In Figure 4.9 we have used Eq. 4.20 and the measured intensity fluctuations at a light intensity of $I_0 = 50\ \mu\text{W/cm}^2$ to predict the resulting frequency noise. An average of ten time transients, each lasting 8 s, was taken to obtain fluctuations in intensity. A 100 Hz low-pass butterworth filter (80 dB/oct) was applied to avoid aliasing. In Figure 4.9 we show that the frequency noise predicted from the observed fluctuations in light intensity and from Eq. 4.20 is many orders of magnitude smaller than what is observed. We conclude that fluctuations in light intensity do not contribute significantly to the observed frequency noise.

4.2.3 Conclusions

Here we have introduced a charge trapping and detrapping model that quantitatively explains the observed photopotential fluctuations as a function of illumination wavelength, frequency, tip-sample distance, and applied tip voltage. From a comparison to the observed data, we have inferred an occupation fraction of the trapping sites of ≈ 0.995. We have demonstrated that photoinduced voltage fluctuations can exhibit a characteristic dependence on illumination wavelength and can be understood quantitatively.

4.3 Light Induced Frequency Noise at an Individual Trapping Site

Previously, we have computed the frequency noise due to a distribution of charge traps. Here we will explore frequency noise due to a single charge trap. Such frequency noise has been observed experimentally. For instance, Grutter *et al.* observed light induced frequency noise over a InP/InGaAs heterostructure [38, 112]. However, to our knowledge, there has been no quantitative study of the frequency noise due to individual charge traps. Here we compute the frequency noise near a charge trapping site and compare our prediction with the observed noise in Ref. 38. From Eq. 4.3 the voltage noise from a single charge trap is given by

$$P^{\text{single}}_{\phi_1,\phi_2}(f) = \frac{4\phi_1\phi_2}{(\tau_f + \tau_v)(\tau^{-2} + 4\pi^2 f^2)} \tag{4.21}$$

where ϕ_i is the electric potential due to a point charge q, τ_f^{-1} and τ_v^{-1} are the rates associated with trapping and detrapping, respectively, and $\tau^{-1} = \tau_f^{-1} + \tau_v^{-1}$. For a cantilever located immediately above the charge trap, we have from Coulomb's law

$$P^{\text{single}}_{\phi_1,\phi_2}(f) = \frac{4q^2}{(4\pi\epsilon_0)^2 z_1 z_2 (\tau_f + \tau_v)(\tau^{-2} + 4\pi^2 f^2)}. \tag{4.22}$$

The frequency noise $P_{\delta f}$ can be computed from $P^{\text{single}}_{\phi_1,\phi_2}$ using Eq. 4.2. The resulting expression for frequency noise contains both capacitance C and spatial derivatives of C. We have found that the term proportional to capacitance C^2 dominates, so that the resulting frequency noise can be approximated as

$$P_{\delta f_c}(f,d) \approx \frac{f_c^2(V_{\text{ts}}-\phi)^2}{4k_c^2} C(z_1)C(z_2)\,\partial_{z_1}^2\partial_{z_2}^2 P_{\delta\phi(z_1),\delta\phi(z_2)}(f)\big|_{d=z_1=z_2}\,. \tag{4.23}$$

From Eq. 4.22 and Eq. 4.23 we estimate the frequency noise due to a single charge trap to be

$$P^{\text{single}}_{\delta f_c}(f,d) \approx \frac{\beta(1-\beta)q^2C^2(d)f_c^2(V_{\text{ts}}-\phi)^2}{k_c^2(4\pi\epsilon_0)^2d^6}\frac{\tau^{-1}}{\tau^{-2}+4\pi^2f^2}. \tag{4.24}$$

where $\beta = \tau_f/(\tau_f+\tau_v)$ is the average occupation fraction of the trap. Note that the noise is at a maximum if the trap is occupied roughly half the time, i.e. $\beta = 0.5$. Using the parameters in Ref. 38 or reasonable guesses of those parameters ($C \approx 10^{-18}$ F, $f_c = 2\cdot 10^5$ Hz, $k_c = 50$ N/m, $V_{\text{ts}}-\phi = 5$ V, $d = 50$ nm, $f = 1$ Hz) and taking $\tau = 2\pi f$, we estimate

$$P^{\text{single}}_{\delta f_c}(f,d) = 2\cdot 10^{-4}\ \text{Hz}^2/\text{Hz}. \tag{4.25}$$

The predicted noise is over an order of magnitude smaller than the observed noise of $\approx 6\cdot 10^{-3} Hz^2/Hz$. The discrepancy can be explained by the uncertainty in the input parameters. The tip-sample distance of $d = 50$ nm, in particular, was only an estimate since Ref. 38 did not provide that number. Because the noise scales as d^{-6}, it is not surprising that the estimated frequency noise differs by an order of magnitude from what we predict.

4.4 Exciton-Induced Frequency Noise

So far, we wave only considered noise induced by charges. However, excitons also generate electric potentials and may potentially also lead to cantilever noise. Studying exciton motion

is important as the diffusion constant of photo-generated excitons is a bottleneck for the performance of organic solar cells. An exciton will only generate current if it can diffuse to an interface between electron and hole transporting materials before decaying. In spite of the crucial role that exciton diffusion plays in organic solar cells, there are only few tools (for example pump-probe spectroscopy [117]) available to study exciton diffusion. In the following we investigate the feasibility of exciton motion as frequency noise in an electric fore microscope experiment.

In the following calculation, which is adapted from the free diffusion model in Chapter 5, we will derive an expression relating the observable frequency noise in an electric force microscope to the exciton propagator and to the field gradient produced by the exciton. We assume that excitons are uniformly distributed along the sample surface, diffuse freely in two dimensions, and are characterized by a lifetime $\tau = 1/\lambda$. Each exciton acts as a point-dipole and so interacts with the charged cantilever placed perpendicular and a distance d above above the sample. The orientation of each dipole is taken to be random and constant in time. The potential felt by the cantilever due to an exciton at location $\mathbf{r}$ is given by

$$\phi_{\text{dip}}(\mathbf{r}) = \frac{\mathbf{p}}{q} \cdot \nabla V_q(\mathbf{r}) \tag{4.26}$$

where $\mathbf{p}$ is the electric dipole of the exciton and $\mathbf{r} = (x, y, h)$ the position vector from the cantilever tip to to the dipole. Exciton motion results in a fluctuating contact potential $P_{\delta\phi(z_1),\delta\phi(z_2)}$ and by Eq. 4.2 in frequency noise. To compute $P_{\delta\phi(z_1),\delta\phi(z_2)}$, we consider an exciton traveling along the sample surface from position $\mathbf{r}_1 = (x_1, y_1)$ to $\mathbf{r}_2 = (x_2, y_2)$ in a time t. The correlation function between the electrostatic potential at heights z_1 and z_2, i.e. $C_{\delta\phi(z_1),\delta\phi(z_2)}$, is given by

$$C_{\delta\phi(z_1),\delta\phi(z_2)}(t) = \left\langle \int d\mathbf{r}_1 d\mathbf{r}_2 \phi_{\text{dip}}(\mathbf{r}_2)\phi_{\text{dip}}(\mathbf{r}_1) \cdot K(\mathbf{r}_2, \mathbf{r}_1, t) N(\mathbf{r}, 0) \right\rangle. \tag{4.27}$$

Here $N(\mathbf{r}_1, 0)$ is the initial exciton (areal) density, $E_{xx}(\mathbf{r})$) is the electric field gradient felt by the tip located a distance z above the surface, and K is the propagator for exciton motion defined by

$$N(\mathbf{r}, t) = \int d\mathbf{r}_1 K(\mathbf{r} - \mathbf{r}_1; t) N(\mathbf{r}_1, 0). \tag{4.28}$$

Assuming that the initial exciton density is uniform, i.e. $N(\mathbf{r}_1, 0) = N_0$, and taking a Fourier transform in x, y, and t, we get

$$P_{\delta\phi(z_1),\delta\phi(z_2)}(f) = N_0 \left\langle \int d\mathbf{k} K(\mathbf{k}, f) \left|\phi_{\text{dip}}(\mathbf{k})\right|^2 \right\rangle. \tag{4.29}$$

From Appendix A, the Fourier transform of the electric potential of a point dipole $\mathbf{p}$ is given by

$$\tilde{V}_{\text{dip}}(k_x, k_y, z) = [\mathbf{p} \cdot (k_x, k_y, -k)] \frac{1}{2\epsilon_0 k} e^{-2\pi z k} \tag{4.30}$$

where $k = \sqrt{k_x^2 + k_y^2}$ is the magnitude of the wavevector $\mathbf{k}$ in the xy-plane. All that is left is to compute the exciton propagator $K(\mathbf{k}, f)$. To compute $K(\mathbf{k}, f)$, we assume that the exciton density $N(\mathbf{r}, t)$ obeys the relation

$$\partial_t N(\mathbf{r}, t) = D \bigtriangledown^2 N(\mathbf{r}, t) - \lambda N(\mathbf{r}, t). \tag{4.31}$$

Here D is the diffusion constant along the sample surface and $\lambda N(\mathbf{r}, t)$ is a decay term accounting for the finite exciton lifetime $\tau = 1/\lambda$. Taking a spatial Fourier transform, we have

$$\partial_t N(\mathbf{k}, t) = -D(2\pi k)^2 N(\mathbf{k}, t) - \lambda N(\mathbf{k}, t). \tag{4.32}$$

The solution to this equation is

$$N(\mathbf{k}, t) = N(\mathbf{k}, 0) e^{-4\pi^2 D k^2 t - \lambda t}. \tag{4.33}$$

The propagator (or Green's function) is the solution $K(\mathbf{r}, t) = N(\mathbf{r}, t)$ subject to the initial condition $N(\mathbf{r}, 0) = \delta(\mathbf{r})$. Inserting the Fourier transform of a delta function for $N(\mathbf{k}, 0)$

gives

$$\begin{aligned} K(\mathbf{k},t) &= e^{-4\pi^2 Dk^2 t-\lambda t}\int d\mathbf{r} e^{2\pi i \mathbf{k}\cdot\mathbf{r}}\delta(\mathbf{r}) \\ &= e^{-4\pi^2 Dk^2 t-\lambda t}. \end{aligned} \tag{4.34}$$

Taking a cosine transform in time, we finally arrive at

$$\begin{aligned} K(\mathbf{k},f) &= 4\int_0^\infty dt\cos(\omega t)K(\mathbf{k},t) \\ K(\mathbf{k},f) &= 4\Re\left[\int_0^\infty dt e^{i\omega t}e^{-4\pi^2 Dk^2 t-\lambda t}\right] \\ K(\mathbf{k},f) &= 4\frac{4\pi^2 Dk^2+\lambda}{(4\pi^2 Dk^2+\lambda)^2+\omega^2} \end{aligned} \tag{4.35}$$

The prefactor of 4 arises because we changed the bounds of integral from $(-\infty,\infty)$ to $(0,\infty)$ and because we restrict ourselves to positive frequencies ($f>0$). This is the same prefactor that appears in the definition of the power spectrum in Eq. 2.7. We note that for small distances (large k), the decay term (λ) becomes negligible. This makes physical sense because we only expect the decay terms to become important on larger length scales, or equivalently, on longer time scales. Using the propagator in Eq. 4.35 and the electric potential in Eq. 4.26, Eq. 4.29 becomes

$$P_{\delta\phi(z_1),\delta\phi(z_2)}(f) = N_0\left\langle\int d\mathbf{k}4\frac{4\pi^2 Dk^2+\lambda}{(4\pi^2 Dk^2+\lambda)^2+\omega^2}\left|[\mathbf{p}\cdot(k_x,k_y,-k)]^2\left(\frac{1}{2\epsilon_0 k}\right)^2 e^{-2\pi(z_1+z_2)k}\right|^2\right\rangle. \tag{4.36}$$

where the angular brackets indicate an average over all orientations of the electric dipoles. The orientation of the dipole is determined by the local electrostatic environment and is taken to be random and constant in time. To take the average over all orientations, we expand the dot product in Eq. 4.36,

$$\left\langle(k_x,k_y,-k)\cdot\mathbf{p})^2\right\rangle = k_x^2\left\langle p_x^2\right\rangle + k_y^2\left\langle p_y^2\right\rangle + k^2\left\langle p_z^2\right\rangle \tag{4.37}$$

where we have used the fact that cross terms, i.e. $< p_x p_y >$, etc. vanish for isotropically distributed dipoles. Since $p_x^2 + p_y^2 + p_z^2 = p^2$, it follows that

$$\langle p_x^2 \rangle = \langle p_y^2 \rangle = \langle p_z^2 \rangle = \frac{p^2}{3} \tag{4.38}$$

for an isotropic distribution of dipoles. Combining Eq. 4.38 and Eq. 4.37 and using $k_x^2 + k_y^2 = k^2$, we have

$$\langle (k_x, k_y, -k) \cdot \mathbf{p})^2 \rangle = \frac{2k^2 p^2}{3}. \tag{4.39}$$

Because the integrand only depends in the magnitude of $\mathbf{k}$, the integral is most easily done in polar coordinates. The integral over the polar angle gives a factor of 2π. Using Eq. 4.39, the power spectrum of the electric potential in Eq. 4.36 becomes

$$P_{\delta\phi(z_1),\delta\phi(z_2)}(f) = 2\pi N_0 \int k dk 4 \frac{4\pi^2 D k^2 + \lambda}{(4\pi^2 D k^2 + \lambda)^2 + \omega^2} \frac{2p^2 k^2}{3} \left(\frac{1}{2\epsilon_0 k}\right)^2 e^{-2\pi(z_1+z_2)k}. \tag{4.40}$$

Changing to dimensionless variables, $\hat{\lambda} = z^2\lambda/D$, $\alpha = zk$, and $\hat{\omega} = 2\pi f z^2/D$ and setting $z = z_1 = z_2$, the power spectrum of the electric potential is

$$P_{\delta\phi,\delta\phi}(z, f) = \frac{4\pi N_0 p^2}{3\epsilon_0^2 D} \int d\alpha \alpha \frac{\alpha^2 + \hat{\lambda}}{(\alpha^2 + \hat{\lambda})^2 + \hat{\omega}^2} e^{-2\alpha}. \tag{4.41}$$

The uniteless integrand in Eq. 4.41 is plotted in Figure 4.10. For Ref. purposes, we also compute the power spectra of the fields and field gradients can be computed by taking spatial derivatives of $P_{\delta\phi(z_1),\delta\phi(z_2)}$, i.e.

$$\begin{aligned} P_{\partial_z^m\phi,\partial_z^n\phi}(z, f) &= \partial_{z_1}^m \partial_{z_2}^n P_{\delta\phi(z_1),\delta\phi(z_2)}(f)\big|_{z_1=z_2=z} \\ P_{\partial_z^m\phi,\partial_z^n\phi}(z, f) &= \frac{4\pi N_0 p^2}{3\epsilon_0^2 D z^{m+n}} \int d\alpha \alpha^{n+m+1} \frac{\alpha^2 + \hat{\lambda}}{(\alpha^2 + \hat{\lambda})^2 + \hat{\omega}^2} e^{-2\alpha}. \end{aligned} \tag{4.42}$$

To estimate the frequency noise from Eq. 4.41, we take the limit where $\hat{\lambda} = \lambda z^2/D \gg 1$. This is the limit in which the diffusion length, $\sqrt{D/\lambda}$ is less than the tip-sample distance

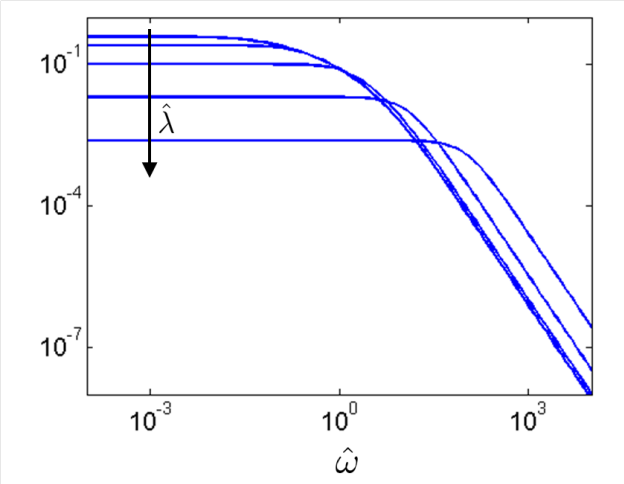

Figure 4.10: The uniteless integral in Eq. 4.41 as a function of $\hat{\omega} = 2\pi f z^2/D$ for a range of values for $\hat{\lambda} = z^2\lambda/D$, i.e. $\hat{\lambda} = 10^{-4}, 10^{-2}, 1, 10^2, 10^4$. The arrow indicates the direction of increasing $\hat{\lambda}$. We see that the noise is white at low frequencies and $1/f^2$ at large frequencies.

z. This is a reasonable assumption in most solar cells where the diffusion length is of the order of ten of nanometers (5 nm in pentacene [118]), compared with a typical tip-sample separation of 100 nm. In this limit Eq. 4.41 becomes,

$$\begin{aligned} P_{\delta\phi,\delta\phi}(z,f) &= \frac{4\pi N_0 p^2}{3\epsilon_0^2 D}\frac{\hat{\lambda}}{\hat{\lambda}^2+\hat{\omega}^2}\int d\alpha \alpha e^{-2\alpha} \\ P_{\delta\phi,\delta\phi}(z,f) &= \frac{\pi N_0 p^2}{3\epsilon_0^2 z^2}\frac{\lambda}{\lambda^2+4\pi^2 f^2}. \end{aligned} \tag{4.43}$$

As one may have expected, the dependance on the diffusion constant cancels. The noise in Eq. 4.43 has a Lorentzian spectrum. In the low frequency limit ($\omega \ll \lambda = 1/\tau$) the noise looks white and takes the form

$$P_{\delta\phi,\delta\phi}(z,f) = \frac{\pi N_0 p^2}{3\epsilon_0^2 z^2 \lambda}. \tag{4.44}$$

We estimate the dipole of an exciton using $p = qa_0'$ where q is the elementary charge and a_0' is the electron-hole separation of the exciton. Taking the effective (reduced) mass of the exciton

to be equal to half the electron mass and assuming that the relative dielectric constant of the medium is $\epsilon_r \approx 3$, we can express p in terms of the Bohr radius a_0 as $p \approx 6ea_0$. The frequency noise can be computed from Eq. 4.2 and Eq. 4.44. The result is much less than the noise in the trapping model. There are two reasons for this. First, charges are much less separated in the exciton diffusion model: The Bohr radius of 0.05 nm is much smaller than a typical separation between charges and their image charges of typically ≈ 100 nm. Second, the mean lifetime for excitons (850 ps in pentacene [118]) is much shorter than the relevant trapping times, which are of the order of a few Hertz. From these considerations, we expect the exciton induced frequency noise to be $(0.05\text{ nm}/100\text{ nm})^2(850\text{ ps}/1\text{ s}) \approx 10^{-16}$ smaller than that due to charge trapping. We conclude that exciton induced frequency noise cannot be detected by electric force microscopy.

Chapter 5

Charge Induced Frequency Noise over Organic Transistors

5.1 Motivation

In recent years, much effort has gone into the development of organic electronics. While the performance of organic electronics does not rival that of silicon based technologies, they hold promise as cheap alternatives to silicon based technologies because they can be processed under ambient conditions, and are inherently physically flexible. A summary of various classes of organic semiconductors is presented elsewhere [36, 119] and will not be repeated here. The figure of merit for organic device performance is the charge mobility μ defined by

$$v = \mu E \tag{5.1}$$

or

$$J = \mu \rho E \tag{5.2}$$

where $J = v\rho$ the current density, v the drift velocity of the charge carriers, and ρ the charge density per unit volume. The charge mobility μ is most commonly extracted from bulk measurements of current and voltage. While obtaining μ from such measurements is straightforward, it has the drawback that it assumes that μ is independent of applied electric field and charge density. This assumption is invalid. There is ample evidence that charge mobility depends on both electric field [28, 31] and charge density [120, 121]. The charge mobility also depends on local properties of the film, such as the film morphology [122] and

on the number of semiconducting monolayers [123]. In amorphous materials, the dependence of carrier motion on carrier density, electric field, and temperature has to date been described using microscopic charge-hopping models [27–33] which largely neglect long-ranged inter-carrier interactions. Recently, it has been shown that inter-carrier interactions greatly enhance the performance of electronic ratchet circuits [34]. Here we propose and demonstrate another dramatic signature of inter-carrier interactions, the suppression of electrostatic potential fluctuations by several orders of magnitude. Before discussing our measurements of potential fluctuations above organic semiconductors, we will review the existing models of charge transport and the relevant experimental techniques used to study transport properties in these materials.

5.1.1 Various Models of Charge Transport in Organics

While charge transport in silicon-based devices is well understood, charge transport in organics remains a topic of research. In organic materials, charge transport is enabled by the delocalization of $\pi-$electrons. In amorphous (or disordered) films of small $\pi-$conjugated molecules, charges are thought to be localized and charge transport mediated by hopping between individual molecules. This picture of localized transport also applies to molecular solids. For instance, it has been shown from optical spectroscopy measurements that charge transport in a pentacene derivative occurs locally, not by band transport [124]. While charge transport in pentacene derivatives has also been described by grain-boundary barrier models [125], we here focus on localized charge hopping models.

Numerous theoretical models have been developed to better understand the dependence of charge mobility on various quantities, in particular the field and charge density dependence.

Models where charge motion occurs in an energy landscape with a Gaussian distribution are called Gaussian disorder models. Here we present a Gaussian disorder model that does not rely on the effective medium approach presented in Ref. 32. We assume that charge transport can be modelled as a hopping process between neighboring sites. In steady state, the hopping rate away from a site equals the hopping rate into that site. This leads the the condition [27]

$$\sum_{j \neq i} [W_{ij} p_i (1 - p_j) - W_{ji} p_j (1 - p_i)] = 0. \tag{5.3}$$

Here the subscripts (i or j) label the location of the sites, p_i is the probability that site i is occupied and W_{ij} is the transition rate from i to j. The factors of $1 - p_i$ account for the fact that the transitions into state i can only occur if the state is vacant. Double occupancy is not allowed because of the prohibitively large Coulomb penalty for placing two carriers on a single site. Apart from this restriction, Coulomb interaction between carriers are ignored in this model. This assumption is, however, questionable because Coulomb interactions drop off only slowly with distance (i.e. as $1/r$) and so could potentially exhibit important long range effects.

The hopping rates are assumed to be thermally assisted and are given by [27]

$$W_{ij} = \begin{cases} \nu_0 e^{-2\alpha R_{ij} - \frac{(\epsilon_j - \epsilon_i) - qE, R_{ij,x}}{k_B T}}, & \epsilon_j >= \epsilon_i \\ \nu_0 e^{-2\alpha R_{ij}}, & \epsilon_j < \epsilon_i. \end{cases} \tag{5.4}$$

where ν_0 is an intrinsic hopping rate, R_{ij} the distance between sites i and j, ϵ_i the energy on site i, α is the inverse localization length of the localized wave functions, and $k_B T$ the temperature. The factor of $e^{-2\alpha R_{ij}}$ accounts for the fact that charge hopping occurs only between sites whose wavefunctions overlap significantly. The term $qER_{ij,x}$ where E is the applied electric field in the x direction, q is the elementary charge, and $R_{ij,x}$ the x component

of the distance between sites i and j, accounts for the energy due to the applied field. It is straightforward to show from Eq. 5.3 and Eq. 5.4 that in the absence of the applied field, the occupational probabilities are given by a Fermi-Dirac distribution [27]. At sufficiently low carrier densities, when the factors of $1 - p_i$ are negligible, the distribution of occupational probabilities approaches a Maxwell-Boltzmann distribution. In the Gaussian disorder model, the site energies ϵ_i are assumed to be independent and Gaussianly distributed, i.e.

$$P(\epsilon_i) \propto e^{-\frac{\epsilon_i^2}{2\sigma^2}}. \tag{5.5}$$

The shape of the density of states has been experimentally verified to be, at least approximately, Gaussian [126]. Hulea *et al.* have obtained the density of states from current-voltage measurements on an electrochemically gated transistor [126]. More recently, the density of states has been determined from Kelvin Probe Force Microscopy (KPFM) measurements of the surface contact potential ϕ as a function of applied gate bias [127]. In the latter, carriers are introduced into the channel by applying a bias voltage to the gate. As charges fill the channel, the chemical potential shifts upwards, and so does the local contact potential. The larger the density of states, the less the energy levels shift upon adjusting the gate bias. By observing shifts on contact potential as a function of gate bias, the authors are able to determine the density of states. Even though deviations from a perfect Gaussian distribution were observed [126, 127], the density of states is nevertheless assumed to be Gaussian, and the energies ϵ_i are randomly drawn from a Gaussian distribution. Once the site energies have been chosen, Eq. 5.3 and Eq. 5.4 are solved in an iterative fashion with the Fermi-Dirac distribution as the starting point [128]. The mobility is computed from the occupational probabilities p_i using

$$\mu = \frac{\sum_{i,j} W_{ij} p_i (1 - p_j) R_{ij,x}}{E \sum_i p_i}. \tag{5.6}$$

Pasveer *et al.* found that the resulting mobility is well described by the following parame-

terization scheme,

$$\mu(\rho, E) = \mu(\rho, T) e^{f(T)\left[\sqrt{1+0.8\left(\frac{Eqa}{\sigma}\right)^2}-1\right]}, \tag{5.7}$$

where a is the lattice spacing. We see from Eq. 5.7 that mobility of the Gaussian disorder model increases with electric field, which makes intuitive sense because in a hopping process, the individual hopping rates depend exponentially on energy barriers, and so also depend exponentially on the electric field.

Competing with the Gaussian disorder model is the Correlated disorder model [30, 31, 129]. While the Correlated disorder model also relies on hopping transport in a Gaussian energy landscape and also predicts mobility to increase with applied field, the dependence on electric field is somewhat different. The underlying reason for this difference is that neighboring site energies ϵ_i are assumed to be correlated. The presence of a correlation between energies makes intuitive sense because neighboring sites should see a similar electrostatic environment. The energy landscape is assumed to arise from randomly oriented dipoles. Since neighboring sites see the same dipoles, they have similar energies. One can show that the resulting correlation function for the site energies is given by [30]

$$C(r) \approx 2\sigma^2 \left(1 - \frac{a}{r}\right). \tag{5.8}$$

Dunlap *et al.* have computed the mobility for such a model analytically in one dimension. As in the Gaussian disorder model, the mobility is computed from Eq. 5.3, Eq. 5.4, and Eq. 5.6, with the difference that R_{ij} is set to zero and that only nearest neighbor hops are allowed. It is further assumed that charges move independently from one another, which implies that the transport properties are assumed to be independent of carrier density. Formally this assumption is introduced by dropping the factors of $1 - p_i$ in Eq. 5.3. With this assumption,

Dunlap found that the field dependence of mobility is

$$\mu(\rho, E) = \mu(T)e^{C\sqrt{E}}. \tag{5.9}$$

The above result, commonly referred to as the Poole-Frenkel law, has been found to hold at least approximately over a broad class of molecularly doped polymers [29]. Eq. 5.9 can also be derived by treating the energy landscape as a continuum, rather than as a set of discrete energy sites. [129]. An intuitive explanation of the field dependence in Eq. 5.9 is given in Ref. 130. The explanation builds on the fact that charge hopping occurs predominantly at a critical hopping distance which depends on the ratio of the disorder parameter σ and on the square root of the electric field. While the analytical result in Eq. 5.9 could not be extended beyond one dimension, Novikov *et al* showed using a 3D Monte Carlo simulation that the analytical result in Eq. 5.9 holds, at least approximately, in three dimensions as well.

The Correlated disorder models in Refs. 30, 31, 129 ignore the density dependence of the mobility, which can be significant. Tanase *et al.* [120] used a percolation hopping model in an exponential density of states [131] to compare charge density and mobility in hole-only diodes and field effect transistors. They found that the higher charge density in field-effect transistors could explain an enhancement of the mobility by two or three orders of magnitude, as compared to hole-only diodes. Kemerink and coworkers [132] have investigated the density dependence of mobility by measuring the charge mobility in the linear regime and the contact potential profiles over an OFET channel. The authors worked in ultra-high vacuum in order to eliminate traces of water, which they found to introduce an additional density dependence of mobility. Their observations of contact potential profiles as a function of temperature and density (i.e. gate voltage) are consistent with the percolation hopping model in Ref. 131.

Guided by evidence that density dependence matters, Bouhassoune *et al.* [28] introduced a density dependence in the Correlated disorder model by leaving the factors of $1 - p_i$ in

Eq. 5.6 in place. The authors then compared the Gaussian disorder and the Correlated disorder models. They found that while the two models predict a different field dependence, they both give excellent fits to the observed current-voltage data of a hole-only diode.

Apart from density and field, the mobility also exhibits a strong dependence on temperature. Craciun *et al.* [121] used the concept of a transport level [133] to find an intuitive explanation for the temperature dependence within the framework of the Gaussian disorder model. The basic idea is that for hopping transport the temperature dependence takes the form

$$\mu(\rho, E) \propto e^{-\frac{\Delta}{k_B T}}, \tag{5.10}$$

where Δ is the energy required to reach the transport level ϵ_t. At low charge densities, the carriers relax into the thermal equilibrium level ϵ_{th}, so that the activation barrier is given by $\Delta = \epsilon_t - \epsilon_{\text{th}}$. Applying a Maxwell-Boltzmann distribution to the Gaussian density of states in Eq. 5.5, one can show that

$$\epsilon_{\text{th}} = -\sigma^2 / k_B T. \tag{5.11}$$

At high carrier densities, the Fermi energy ϵ_F exceeds ϵ_{th}, and the activation energy is given by $\Delta = \epsilon_t - \epsilon_{\text{F}}$. As mentioned previously, the Fermi distribution arises from Coulomb repulsion rather than from quantum mechanical effects. For this reason the Fermi energy is in this context called a *quasi* Fermi energy. The decrease in activation energy with increasing Fermi energy can be explained as follows. As more charge is placed into the channel, the lower lying energy levels are increasingly filled. As a result the available charge is at a higher energy, thereby lowering the energy required to reach the transport level. We note that at high concentrations, the energy barrier $\Delta = \epsilon_t - \epsilon_{\text{F}}$ no longer depends on temperature. Based

on these considerations, one expects

$$\ln \mu \propto T^{-2} \tag{5.12}$$

at low charge concentrations and

$$\ln \mu \propto T^{-1} \tag{5.13}$$

at high charge concentrations. [121]

The models of charge transport discussed thus far are phenomenological models, which do not consider the microscopics of the organic film and which contain several free parameters. Vukmirovic *et al.* [134], by contrast, have developed an ab-initio model for charge transport in amorphous poly(3-hexylthiophene) (P3HT). Their multi-scale approach makes use of both electronic structure calculations at the sub-nanometer scale and of film morphology at larger length scales.

The charge mobility is not the only parameter that governs charge transport. By the drift-diffusion equation , the current is determined by both charge mobility and diffusion constant D,

$$J = \mu \rho E - D \frac{\partial \rho}{\partial x} \tag{5.14}$$

where x the coordinate along the applied field and ρ is the charge density. While the Einstein relation suggests that charge mobility μ and diffusion constant D are related according to

$$\mu = \frac{qD}{k_B T}, \tag{5.15}$$

this relationship has recently been called into question when applied to organic semiconductors [135]. The Einstein relation can be derived from Eq. 5.14, the definition of the electric field ($E(x) = -\partial\phi(x)/\partial x$), charge conservation ($\dot{n} = -\partial J/\partial x$), and from a Maxwell-Boltzmann distribution of the equilibrium charge density ($n \propto e^{-\frac{q\phi(x)}{k_B T}}$). At high carrier

concentrations, the latter assumption breaks down and the Fermi-Dirac distribution must be used instead. Using a Fermi-Dirac distribution, Roichmann *et al.* [135] have generalized the Einstein relation for a Gaussian density of states. Their generalized relation is identical to Eq. 5.15, except that it contains a prefactor that depends on the width of the Gaussian distribution and on the (charge density dependent) chemical potential. They find that the diffusion constant in light emitting diodes is typically an order of magnitude larger than what is predicted by Eq. 5.15. Mensfort and coworkers [28, 136] have made use of the generalized Einstein relation in order to improve the agreement between the observed current and the Gaussian disorder model prediction in an organic light-emitting diode. The authors used results from the Gaussian disorder model to compute charge mobility and the generalized Einstein equation to compute the diffusion constant from the mobility. They then apply Fick's law (see Eq. 5.14) and Poisson's law to compute the current.

A major obstacle in falsifying the various models of charge transport is that the mobility is usually not measured directly, but inferred from current-voltage measurements. It is therefore challenging to distinguish between the Gaussian disorder model and Correlated disorder model. Even though each model predicts a distinct dependence on electric field, both models provide excellent fits to the experimentally observed current-voltage curves. Falsifying various models of charge transport therefore requires techniques other than standard current-voltage measurements. In the following, we will summarize the various experimental techniques used to extract charge mobility.

5.1.2 Existing Experimental Techniques for Measuring Charge Mobility

In a field-effect transistor (FET), the charge mobility is commonly extracted from the current-voltage ($I-V$) characteristics of the device when operated in either the linear or the saturated (or pinch-off) regime. In the saturated regime, the applied source-drain bias V_{SD} typically exceeds the applied gate voltage V_G. Due to the pinch-off effect, the source-drain current I_{ds} is independent of the applied source-drain voltage, and is given by

$$I_{\mathrm{ds}} = \frac{WC_i}{2L}\mu(V_g - V_t)^2 \tag{5.16}$$

where μ is the charge mobility, W is the channel width, L its length, C_i the capacitance per unit area between the gate and the active layer, and V_t the threshold voltage. From measurements of I_{ds} and V_g, the charge mobility μ and threshold voltage V_t can be extracted. The charge mobility can also be extracted by operating the transistor in the linear regime, i.e. at source-drain voltages low enough that current is proportional to the applied source-drain voltage. In that case, the mobility can be computed from

$$I_{\mathrm{ds}} = \frac{WC_i}{L}\mu(V_g - V_t)V_{\mathrm{SD}}. \tag{5.17}$$

The above expression follows from the definition of mobility in Eq. 5.1, $E = V_{\mathrm{SD}}/L$, and $I = \sigma W v$ where $\sigma = C_i(V_G - V_t)$ is the areal charge density. Eq. 5.17 assumes that the electric field and the charge density are constant throughout the channel, which is true only for small applied source-drain voltages, i.e $V_{\mathrm{SD}} \ll V_G - V_t$. The charge mobility can also be extracted by constructing a diode and examining its electrical characteristics. The current J, often referred to as the space charge limited current (SCLC), is measured as a function of applied voltage V. By Mott-Gurney's law the SCLC is given by

$$J = \frac{9}{8}\epsilon_r\epsilon_0\mu\frac{V^2}{L^3} \tag{5.18}$$

where ϵ_r is the relative dielectric constant of the polymer, ϵ_0 the permittivity of free space, and L the thickness (or length) of the organic layer. Recently, this technique has been used to determine the mobility locally by measuring the current with conductive atomic force microscopy. [137]

While obtaining charge mobility from such bulk measurements of current and voltage is straightforward, these methods have the drawback that they ignore the voltage drop (or contact resistance) that occurs at the injecting contact due to a Schottky barrier. The effects of the voltage drop become particularly important at low source-drain bias and at high mobility. Correcting for the voltage drop is somewhat challenging since the size of this effect is a function of the applied electric field. Another disadvantage of these methods is that they (incorrectly) assume the mobility to be constant. Studying the dependence of the charge mobility on applied electric field or charge density therefore requires experimental techniques other than current-voltage measurements.

One such method is time-of-flight (TOF), which was discovered simultaneously by three scientists [138–140]. In this method, a semiconducting layer is sandwiched between two electrodes. Carriers are generated near one of the electrodes. Most commonly, the carriers are generated by photoexcitation with a laser, in which case one of the electrodes must be transparent. The photoexcited carriers drift in an applied field from one electrode to the other. The time it takes for the carriers to reach the other electrode is called the transit time t_{tr}, and is given by

$$t_{\mathrm{tr}} = \frac{L}{v} \tag{5.19}$$

where L is the thickness of the organic layer, and $v = \mu E$ the drift velocity of the charge

carriers. The applied field is given by $E = V/L$. The charge mobility can be computed as

$$\mu = \frac{L^2}{V t_{\mathrm{tr}}}. \tag{5.20}$$

An advantage of the time-of-flight method is that the mobility can be measured as a function of the applied voltage/field. Another advantage is that the mobility of holes and electrons can be measured separately. For instance, if the mobility of the holes is to be measured, a positive voltage is applied to the electrode where the charge is generated. In that case, only the holes are pulled toward the opposite electrode by the applied electric field. A limitation of the TOF method is that the transit time t_{tr} has to be longer than the RC charging time where R and C are the resistance and capacitance across the dielectric layer, respectively. An additional restriction is that the transit time t_{tr} has to be much shorter than the dielectric relaxation time of the sample. If this is not the case, the generated carriers will be neutralized by flow of charge within the organic layer before it reaches the electrode. An all electronic version of time-of-flight, where the carriers are generated electronically rather than by photo-excitation, has recently been demonstrated in a polymer field-effect transistor [141–143].

Juska and coworkers [144] invented a method called *carrier extraction by linearly increasing voltage* (CELIV) to extract carrier mobility. The method is somewhat similar to TOF. In CELIV, one electrode is grounded while a linearly increasing voltage $\dot{V}$ is applied to the other electrode. By solving Poisson's equation and applying charge conservation, one can solve for the resulting transient current response, which peaks after a time t_{max}. In low mobility materials the extracted charge only negligibly changes the electric field and t_{max} is given by

$$t_{\mathrm{max}} = d\sqrt{\frac{2}{3\mu\dot{V}}}. \tag{5.21}$$

The above expression corresponds within a factor of order one to the time it takes a small charge to cross a distance d in a linearly increasing electric field, i.e. from $d = \frac{1}{2}\dot{v}t^2$, $v(t) = \mu E = \mu V(t)/d$, and $V(t) = \dot{V}t$. Unlike TOF, CELIV does not require light to generate the charge carriers, so there is no need for one of the electrodes to be transparent. The main disadvantage of CELIV compared to TOF is that it is unable to determine the sign of the charge carriers. [145].

Another method of extracting carrier mobility is time resolved microwave conductivity (TRMC), which was first developed by P. G. Schouten and coworkers [146]. In this method, the free carriers are generated with a pulse of MeV electrons. The additional carriers induce a transient enhancement in the conductivity of the sample, which is measured via a change in the microwave power reflected by the sample. In terms of the electron and hole mobilities, μ_e and μ_h, the change in the conductivity $\Delta\sigma$ can be written as

$$\Delta\sigma = q(\mu_e n_e + \mu_h n_h) \tag{5.22}$$

where q is the elementary charge, and n_e and n_h are the electron and hole charge densities. The carrier densities are estimated from the amount of light absorbed. One drawback of this method is that contributions from holes and electrons cannot be distinguished. Second, it must be remembered that the conductivity and therefore the mobility are measured at microwave frequencies. At such high frequencies (or short time scales), carriers typically only move a few nm. Therefore TRMC does not measure charge mobility associated with crossing grain boundaries and so usually overestimates charge mobility [145].

Burgi and coworkers [147] have developed a technique based on Kelvin probe force microscopy that enables a local measurement of the charge mobility in a field-effect transistor. In this method, the contact potential $\phi(x)$ is measured as a function of distance along the channel of a field-effect transistor. The current through the device, $I_{\text{ds}} = \sigma W v$, where $\sigma(x)$

is the areal charge density at location x, can be written in terms of the mobility $\mu = v/E$ as

$$I_{\text{ds}} = qW\sigma(x)E(x)\mu. \tag{5.23}$$

The local electric field $E(x)$ is determined by taking a derivative of the electrostatic potential, i.e. $E(x) = -\partial\phi(x)/\partial x$ and the local charge density is computed from the capacitance C_i and voltage drop $V_G - \phi(x)$ across the insulator as $\sigma(x) = C_i(V_G - \phi(x)$. Eq. 5.23 allows for the determination of the mobility as a function of both charge density and electric field.

In inorganic semiconductors, charge mobility is commonly determined by Hall effect measurements. Here a magnetic field B is applied perpendicular to the current I. Due to the Lorentz force, a voltage drop, called the Hall voltage or V_H, occurs perpendicular to the current. If only a single sign of charge carriers is present, the Hall voltage across a slab of thickness d is given by

$$V_H = -\frac{IB}{\rho d}. \tag{5.24}$$

Measurements of the V_H can be used to determine the charge density ρ. Once the charge density is known, the mobility, or Hall mobility, is determined from Eq. 5.2. We note that the sign of V_H reveals the sign of the charge density and therefore the sign charge carriers if only a single charge carrier species is present. The treatment for ambipolar materials, where both holes and electrons conduct, is analogous, though more complicated. While the Hall effect is commonly used to determine mobility in inorganics, the mobility in organic semiconductors is typically too small to be measured. While the Hall mobility has been measured in a single-crystal organic semiconductor [148], this technique has, to our knowledge, not been demonstrated in amorphous organics.

5.1.3 Previous Work on Fluctuations in Organic Devices

Charge transport in organics can also be investigated by looking at fluctuating, rather than static, quantities. Carbone *et al.*, for example, have investigated conductivity noise in organic diodes in the Ohmic, trap-filling, and space charge limited regimes [111, 149]. They observed increased noise in the trap filling region. The authors explain their observations in terms of charge trapping within a continuum percolation model. Observations of fluctuating quantities may also be of practical use. Sampietro and coworkers, for instance, discovered that device degradation in organic light emitting diodes (OLEDs) can be tracked by observing conductivity noise [150]. The authors found their fluctuations technique to be more effective than other means of tracking device degradation, such as measuring the current through the OLED.

Conductivity noise has also been studied in inorganics [151, 152]. In order to explain the $1/f$ resistance noise observed in doped Ge$<$ Ga $>$ and Ge$<$ As $>$ hopping conductors [152], Kozub and coworkers developed a theory based on fluctuators (or modulators) [153]. In their model, the energy barrier for the hopping process is modulated by the electric potential of a nearby charge, as it transitions between two neighboring sites. The terms *fluctuator* here refers to charge hopping between the two states. For an exponentially broad distribution of hopping times, the noise spectrum of the fluctuators is $1/f$. Pokrovskii *et al.* [154] have applied the theory of fluctuators (or modulators) to explain the temperature and concentration dependence of current fluctuations in an electron channel in a metal semiconductor FET (MESFET) structure.

While there have been ample studies of fluctuations in both organic and inorganic devices, these studies all measure bulk, rather than local, quantities. Observing cantilever frequency

noise in an electric force microscope experiment could therefore provide new insight into device performance. In the following, we will discuss measurements of cantilever frequency noise over OFETs. In Section 5.3, we will propose an electric force microscope technique based on time-of-flight to locally determine the charge mobility in OFETs.

5.2 Cantilever Frequency Noise over Organic Transistors

5.2.1 Observed Cantilever Frequency Noise

Here we present cantilever frequency noise measurements over OFETs. A poly(3-hexylthiophene) (P3HT) transistor was chosen as one device of study because P3HT is commonly used in organic electronics. Measurements were also performed over a molecularly doped polymer transistor with N,N'-Diphenyl-N,N'-di(3-tolyl)-4-benzidine (TPD) as the transport molecule. A molecularly doped polymer was chosen because charge transport in this system is well understood and known to be mediated by charge hopping [33]. Another advantage of constructing a TPD transistor is that films spun from a TPD solution are generally very flat with a roughness of ±3 nm, as observed by atomic force microscopy. More detail on charge transport in a TPD transistor can be found in Refs. 40 and 36. Charge transport in P3HT is thought to occur by phonon-assisted hopping. [27, 134]

The transistor substrate was fabricated by growing 315 nm of oxide onto a Si wafer followed by a patterned deposition of 5 nm of Cr (the adhesion layer) and 30 nm of Au, as outlined in Appendix B. The channel length and widths are 5 μm and 0.75 m. From the oxide thickness and the relative dielectric constant of SiO_2 of 4.65 [155], we estimate a capacitance per unit area across the dielectric of $C_i = 4.65\epsilon_0/315nm = 1.3 \times 10^{-4}$ Fm^{-2}. The TPD transistor was prepared by spin casting a solution containing TPD (obtained from Xerox, used as received) and polystyrene (Sigma-Aldrich 327786, M_w 200000, PDI unknown) onto a transistor device structure. In order to minimize exposure to humidity, which was found to detrimentally affect device performance, the TPD solution was prepared using a Schlenk line. The solution was prepared by adding 25 mg of TPD and 17.4 mg of polystyrene to a 15 mL pear flash containing a magnetic stirbar and capped by a 14/20 funnel. The flask

was connected to the Schlenk line and backfilled with nitrogen. With a syringe we added 5 mL of tetrahydrofuran, which was previously dried using molecular sieves. The resulting solution was then stirred for at least 30 min. The transistor substrates were cleaned initially by rinsing them in acetone, isopropyl alcohol (IPA), and then blow drying. A multimeter was used to ensure that the source drain electrodes were not shorted. To clean the transistor substrates, they were sonicated in acetone for 15 min, followed by a 10 min ozone treatment. It was found that the surface cleanliness was further improved by wiping the surface with soap using a cleanroom swab and rising with deionized water. The samples were then spin rinsed with acetone and IPA, followed by hexamethyldisilazane (HMDS), which was left on the surface for at least 10 s. The purpose of HMDS is to passivate dangling oxygen bonds on the hydrophilic SiO surface, rendering the surface hydrophobic and so achieving better adhesion to the organic layer. After the HMDS treatment, the TPD solution was spun onto the substrate. Here a syringe was used to transfer the TPD solution in order to avoid exposure to the moisture in the air. Spin casting at 2000 rpm for 30 s resulted in a film thickness of (70 ± 7) nm. P3HT transistors were prepared in a similar fashion by dissolving 6 mg of regioregular P3HT (Sigma-Aldrich 445703) in 4.8 ml of chlorobenzene. Spin casting at 2000 rpm for 30 s gave 40 nm thick films.

Once fabricated, the transistors were transferred into an electric force microscope and their electrical characteristics were determined in vacuum using two source meters (Keithley 2400 and Keithley 2630). From the current-voltage measurements for the TPD transistor in Figure 5.1 we compute the mobility and threshold voltage in the linear regime using Eq. 5.17. Figure 5.2 shows slopes from Figure 5.1 obtained by performing a linear fit of the source-drain current I_{SD} to the source-drain voltage V_{SD} at each gate voltage. The fit was performed only for voltages $V_{\mathrm{SD}} < 14$ V. The charge mobility $\mu = 2.7 \cdot 10^{-10}$ $\mathrm{m^2V^{-1}s^{-1}}$ and threshold voltage $V_t = -2.9$ V were obtained from the slope and intercept of the best fit

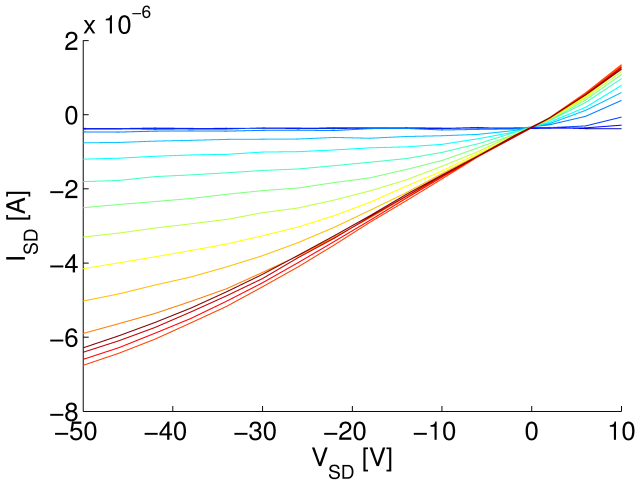

Figure 5.1: Observed source-drain current of a TPD transistor as a function of source-drain voltage for gate voltage ranging from 20 V (light blue) to -50 V (red) in steps of 4 V. The source-drain voltage was swept at a rate of 2 V/s. We computed the charge mobility and threshold voltage in the linear regime from these data by using Eq. 5.17. The transistor current-voltage data were acquired after making several noise measurements. Reprinted with permission from Ref. [2]. Copyright [2012], American Chemical Society.

line in Figure 5.2, respectively. A channel width $W = 75$ cm, a channel length $L = 5$ μm, and a capacitance per unit area of $C_i = 4.65\epsilon_0/315$ nm $= 1.3 \times 10^{-4}$ Fm^2 were used for this calculation.

The cantilever (DPE 18 / AIBS, $f_0 = 64058$ Hz, $k = 3.5$ N/m) was driven by self-oscillation and the frequency noise was measured as described in Chapter 2. A sketch of the OFET and the cantilever is shown in Figure 5.3. When measuring frequency noise power spectra, one must be aware that upon changing either the source-drain, or the gate voltage, the surface contact potential relaxes only slowly to its new equilibrium value, sometimes on the time scale of tens of seconds or more. If a frequency noise spectrum is taken before the

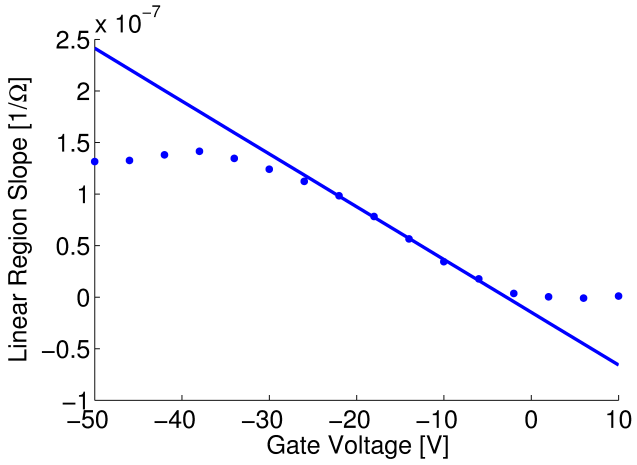

Figure 5.2: Slopes from the current-voltage plots in Figure 5.1 (as discussed in the text) are shown as a function of gate voltage. Also shown is a linear fit to the data at intermediate gate voltages. Reprinted with permission from Ref. [2]. Copyright [2012], American Chemical Society.

contact potential has reached its equilibrium value, the equilibration of the contact potential will result in (apparent) low-frequency noise. In the frequency noise measurements presented here, care was taken to ensure that the observed frequency noise results from equilibrium fluctuations, rather than from such transient effects.

Care must also be taken not to confuse noise induced by stochastic fluctuations from within the transistor with noise induced by vibrations of the sample stage. In Chapter 3 we saw that tip-sample vibrations induced frequency noise is quartic in tip voltage, which enabled us to distinguish vibration induced noise from noise induced by contact potential fluctuations, which we found to be quadratic in tip voltage. Unfortunately, if an electric field is applied, we must also consider frequency noise due to lateral vibrations. From Eq. 2.66

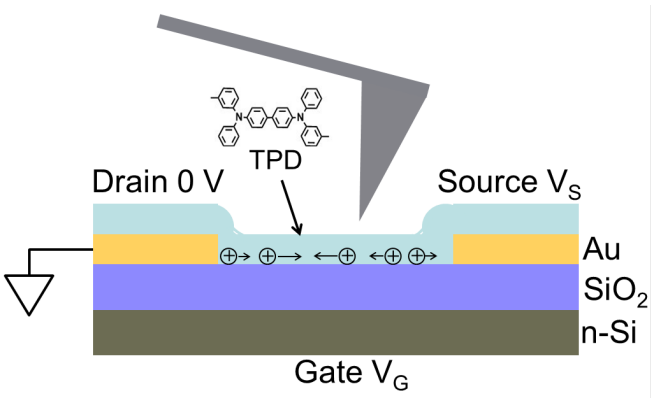

Figure 5.3: A sketch of the cantilever above a TPD transistor. The goal of the experiment is to capture stochastic motion of the charge induced in the transistor channel by electric force microscopy. Adapted with permission from Ref. [2]. Copyright [2012], American Chemical Society.

such frequency induced noise is given by

$$P_{\delta f}^{\text{vib in x}}(f) = \left(\frac{f_c C_2(d) V_{\text{ts}} E_x}{2k_c}\right)^2 P_{\delta x_{\text{ex}}}(f). \tag{5.25}$$

We see that the vibration-induced noise in Eq. 5.25 scales quadratically with tip voltage and can therefore not easily be disentangled from noise due to contact potential fluctuations, which are also quadratic in voltage. Eq. 5.25 also predicts a quadratic dependence of the frequency noise on electric field. In Figure 5.4 we show that quadratic dependence of the noise on both tip voltage and lateral electric field is, in fact, what we observe. Eq. 5.25 also correctly predicts the distance dependence and magnitude of the induced frequency noise. In order to the compute the second derivative of capacitance $C_2(d)$ in Eq. 5.25, we have measured the static frequency shift $\Delta f_c(d)$ as a function of tip-sample voltage. From Eq. 2.48, $\Delta f_c(d)$ is given by

$$\begin{aligned} \Delta f_c(d) &= -\alpha(d) V_{\text{ts}}^2, \\ \alpha(d) &= \frac{f_c}{4k_c} C_2(d). \end{aligned} \tag{5.26}$$

From the observed frequency noise and the curvature $\alpha(d)$ of the frequency versus voltage curves, we have computed the position noise using Eq. 5.25. From the data in Figure 5.5 it is evident that the distance dependence predicted by Eq. 5.25 is consistent with the position noise observed by laser interferometry.

In order to further check if the observed frequency noise is induced by vibrations, we have measured the lateral position noise $P_x(f)$. In Figure 5.6 we show that the observed position noise spectrum agrees in magnitude and spectral shape with what we predict based on Eq. 5.25 and the observed frequency noise. We conclude that the frequency noise in Figure 5.4 indeed arises from vibrations. In order to avoid such vibration-induced frequency noise, measurements must be performed at zero source-drain bias.

Power spectra of cantilever frequency noise at zero-source-drain bias over a TPD transistor are shown in Figure 5.7 for various tip-sample distances d. Each spectrum in Eq. 5.7 shows two frequency regimes: a low-frequency $1/f$ regime with amplitude that increases with decreasing tip-sample distance d and a f^2 regime for $f > 20$ Hz with superposed frequency spikes. The high-frequency regime arises from noise in the photo detector, as discussed in Chapter 2. Because of its dependence on tip-sample distance d, the low frequency noise is assumed to arise from fluctuations in the organic semiconductor. To focus on the dependence of this noise on d and on V_G, we determine the frequency noise, or jitter J, integrated from $f_1 = 0.2$ Hz to $f_{\max} = 3$ Hz, as shown in Figure 5.8. Points show measured jitter for $V_G = 0$ V (circles), -20 V (squares), and -40 V (crosses). The data marked by (x) were taken over the source as a control experiment, and are not significantly different from the other data. These data are expected to agree with the measurements for $V_G = 0$ V and to show the effects of dielectric fluctuations from TPD as well as any residual free charge. Figure 5.8 shows the cantilever frequency noise to be nearly independent of carrier density. Also shown

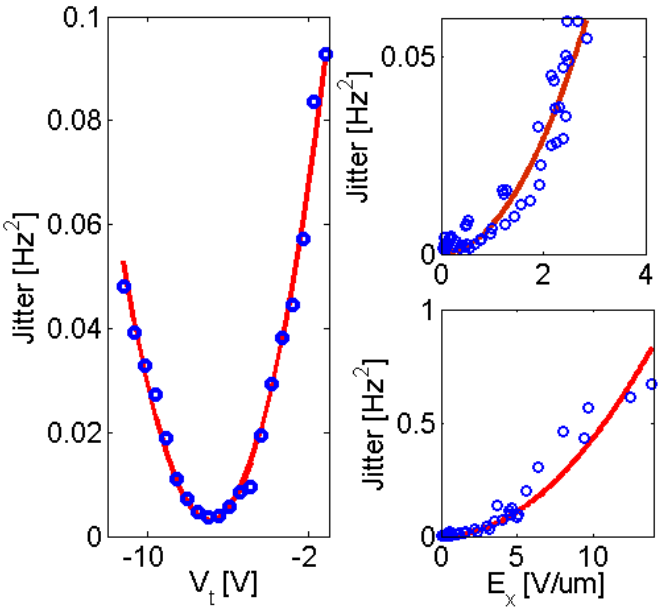

Figure 5.4: In the left panel we show the cantilever frequency noise integrated from 0.2 Hz to 3 Hz as a function of tip voltage V_t 300 nm above the center of the channel of a P3HT transistor. The applied gate and source-drain voltages are $V_G = -20$ V and $V_D = -10$ V, respectively. Also shown is a fit to a parabola (solid line). In the right hand panels we show the integrated frequency noise 300 nm above the P3HT transistor as a function of applied electric field (circles) as well as a fit to a parabola (solid line). The data were acquired at various locations over the channel. The data in the top-right panel were taken at an applied source-drain voltage of $V_D = -10$ V and at gate voltages ranging from -10 V to -40 V. In the bottom right panels drain voltages of -10 V to -40 V were used. For each datum the electric field is determined from the surface contact potential $\phi(x)$ using $E_x = -\partial\phi/\partial x$. Parameters: Cantilever spring constant $k_c = 0.34$ N/m, cantilever resonance frequency $f_c = 58.5$ kHz. The data in the left and right panels were taken in Baker Lab 146 on Oct 18 and Oct 15, 2010, respectively.

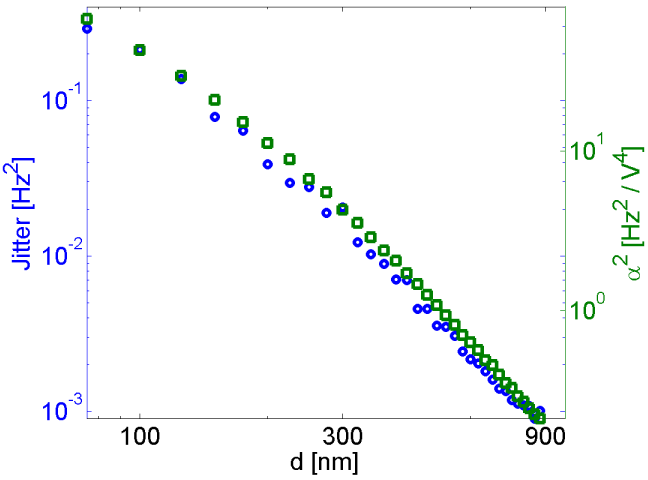

Figure 5.5: The observed cantilever frequency noise integrated from 0.2 Hz to 3 Hz (circles) as a function of distance d above a P3HT transistor. Also shown is the square of the curvature α of the frequency versus voltage curves (squares). Parameters: Cantilever spring constant $k_c = 0.34$ N/m, cantilever resonance frequency $f_c = 58.5$ kHz, and gate voltage $V_G = 0$ V, source-drain voltage $V_{\rm SD} = -40$. The data were taken in Baker Lab on Oct 21, 2010.

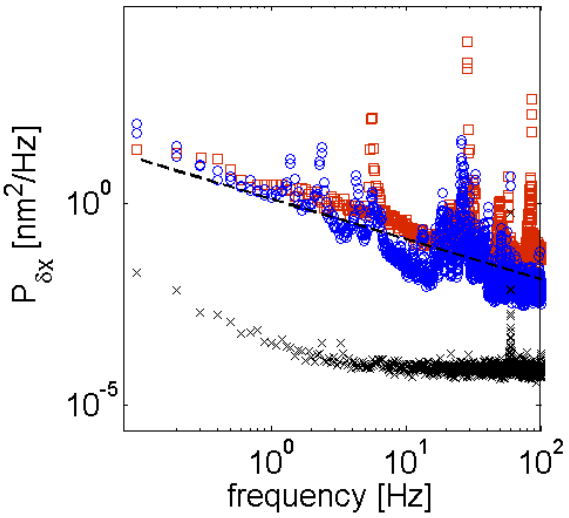

Figure 5.6: Position noise power spectrum observed by laser interferometry with the probe suspended in air (circles). Also shown is the position noise predicted from Eq. 5.25 using the observed frequency noise in vacuum 300 nm above a P3HT transistor (squares). An electric field was generated by applying a source-drain voltage of $V_D = -20$ V across the transistor channel. The electric field $E_x = -\partial\phi/\partial x$ was obtained from the measured contact potential profile $\phi(x)$ and the second derivative of capacitance C_2 in Eq. 5.25 was determined from the curvature $\alpha = f_c C_2/4k_c$ of the frequency parabola. A $1/f$ line is shown as a guide to the eye. The noise from a control experiment (x) where the fiber is not reflected off of anything shows that the noise injected by the laser source and the photo detector are negligible. Parameters: Cantilever spring constant $k_c = 0.34$ N/m, cantilever resonance frequency $f_c = 58.5$ kHz, tip-sample voltage $V_{\rm ts} = -5$ V, . The data were taken in Baker Lab 146 on Nov 4, 2010.

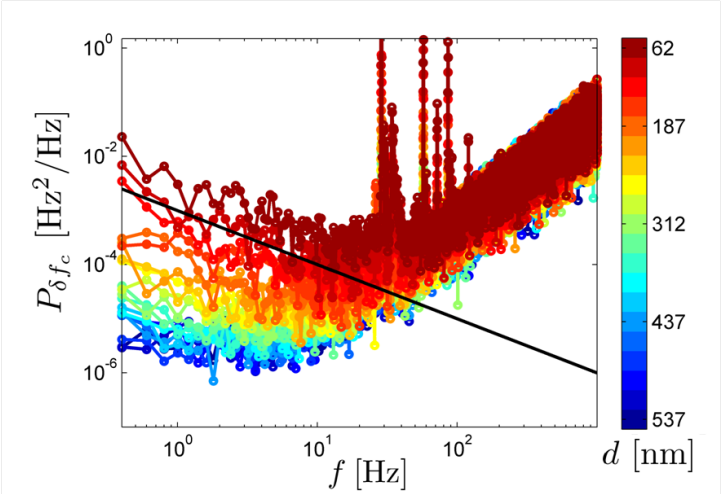

Figure 5.7: The frequency noise spectra over a TPD transistor for various tip-sample distances d, indicated in color. The tip-sample and gate voltage are $V_G = -40$ V and $V_t = -3$ V, respectively. The source and drain electrodes were grounded. These are the spectra corresponding to the integrated noise in Figure 5.8 at $V_G = -40$ V. Also shown is a $1/f$ line as a guide to the eye. The data were taken in the Physical Sciences Building B19 on Nov 8, 2011. Reprinted with permission from Ref. [2]. Copyright [2012], American Chemical Society.

in Figure 5.8 is the frequency noise calculated for a model of freely diffusing charges, which will be discussed in more detail in Section 5.2.2. The calculation greatly overestimates the observed noise. A similar conclusion can be made from the frequency noise observed over a P3HT transistor in Figure 5.10. We conclude that our model of non-interacting carriers is inconsistent with our observations. In Section 5.2.3 we show that including charge interactions results in a suppression of noise by several orders of magnitude, thereby proving that the picture of non-interacting carriers is false. Before discussing the model with charge-charge interactions in place, we will present a calculation based on non-interacting (or freely diffusing) charges.

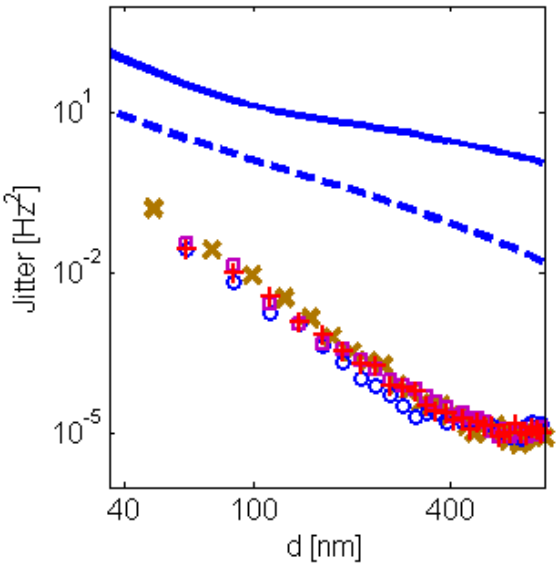

Figure 5.8: Observed cantilever frequency noise (jitter) integrated from 0.2 Hz to 3.0 Hz as a function of tip-sample distance d above the TPD transistor. The frequency noise was measured over the center of the channel at an applied gate voltage of $V_G = 0$ V (circles), $V_G = -20$ V (squares), $V_G = -40$ V (cross), and, as a control experiment, over the electrodes (x). The source and drain electrodes were grounded and the tip voltage was $V_t = -3$ V. The solid line is a calculation based on the free diffusion model (see Eq. 5.36 and Eq. 5.37). The dashed line is a free diffusion calculation that accounts for the presence of image charges (5.36 and Eq. 5.39). For these calculations, we used the Einstein relation to calculate the diffusion constant from the mobility of $\mu = 2.7^{-10}$ m^{2}V^{-1}s^{-1}. The charge density $n_A =$ was calculated from $n_A = C_i(V_t - V_G)/e = 3.0 \times 10^{16}$ m^{-3} with $C_i = 1.3 \times 10^{-4}$Fm^{-2} (see Eq. 5.40) and a threshold voltage of $V_t = -2.9$ V. Both μ and V_t were determined from the current voltage measurements in Figure 5.1 and Figure 5.2. The data were taken in the Physical Sciences Building B19 on Nov 8, 2011. Adapted with permission from Ref. [2]. Copyright [2012], American Chemical Society.

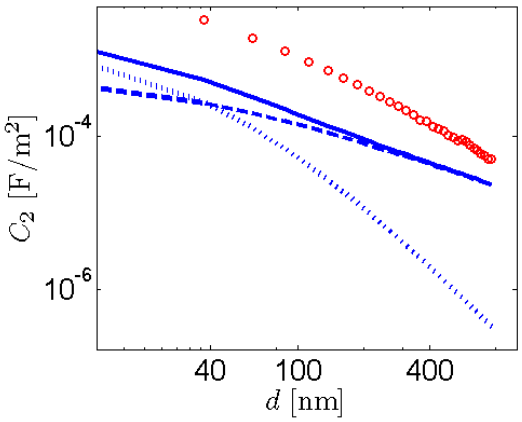

Figure 5.9: Observed second derivative of capacitance as a function of tip-sample distance d above a TPD transistor (circles). The capacitance was calculated from Eq. 5.26 using the observed frequency shift versus tip voltage curve. Also shown is a prediction for a spherical (dotted line) and a conical (dashed line) cantilever tip. The solid line indicates a sum of the sphere and cone contributions. The data were taken in the Physical Sciences Building B19 on Nov 8, 2011. Reprinted with permission from Ref. [2]. Copyright [2012], American Chemical Society.

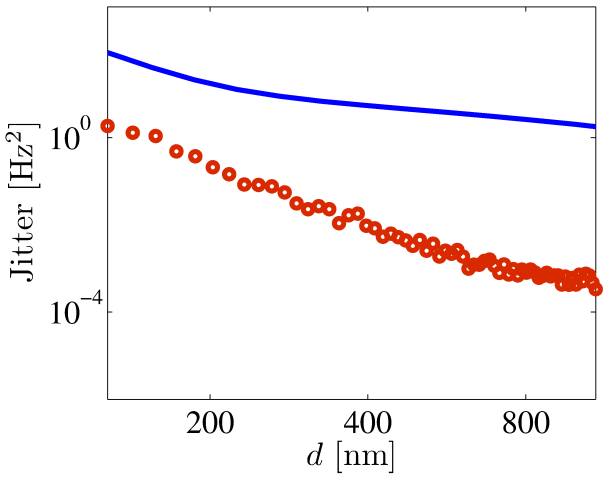

Figure 5.10: Observed cantilever frequency noise (jitter) integrated from 0.2 Hz to 3.0 Hz as a function of tip-sample distance d above P3HT transistor. The frequency noise was measured over the center of the channel at an applied gate and source voltages of $V_G = V_S = -10$ V and at a tip voltage of $V_t = -3$ V. The drain electrode was grounded. The frequency noise was also calculated from the free diffusion model in Eq. 5.36 and Eq. 5.37 (solid line). The data were taken in Baker Lab 146 on Sep 9, 2010.

5.2.2 Frequency Noise due to Non-Interacting Charges

We will now consider cantilever frequency noise induced by non-interacting (or freely diffusing) carriers. The following calculation was adopted from Ref. 156. For simplicity, we will assume that the charges are confined to a 2D plane. This assumption is particularly valid in OFETs, as the charge in the channel is confined to the first few monolayers above the dielectric. To compute the cantilever frequency noise, we first compute the correlation function of the electrostatic potential $\delta\phi(z,t)$ due to charge carrier motion. The potential at two heights z_1 and z_2 will be correlated, and described by the correlation function

$$\langle \delta\phi(z_2,t)\delta\phi(z_1,0)\rangle = c_a \int\int d\mathbf{r}_1 d\mathbf{r}_2 K(\mathbf{r}_2-\mathbf{r}_1,t)\delta\phi(\mathbf{r}_2,z_2)\delta\phi(\mathbf{r}_1,z_1) \tag{5.27}$$

where $\mathbf{r} = (x,y)$, c_a is the number of carriers per unit area, $K(\mathbf{r}_2-\mathbf{r}_1,t)$ is the charge propagator, and $\delta\phi(\mathbf{r},z)$ is the electric potential at the origin due to a charge located at $(\mathbf{r},z)$. The temporal Fourier transform of Eq. 5.27 is the power spectrum $P_{\delta\phi(z_1),\delta\phi(z_2)}(f)$ between the electrostatic potentials at two different heights z_1 and z_2. $P_{\delta\phi(z_1),\delta\phi(z_2)}(f)$ can be written as

$$P_{\delta\phi(z_1),\delta\phi(z_2)}(f) = c_a \int d\mathbf{k}\tilde{K}(\mathbf{k},f)\delta\tilde{\phi}(\mathbf{k},z_2)\delta\tilde{\phi}(-\mathbf{k},z_1) \tag{5.28}$$

where$\tilde{K}(\mathbf{k},f)$ is the temporal and spatial (in x and in y) Fourier transform of $K(\mathbf{r}_2-\mathbf{r}_1,t)$ and $\delta\tilde{\phi}(\mathbf{k},z)$ is the spatial Fourier transform of the electrostatic potential, which from Appendix A is given by

$$\tilde{\phi}_q(k_x,k_y,z) = \frac{q}{4\pi\epsilon_0 k}e^{-2\pi kz}. \tag{5.29}$$

We note that at this point one could account for carrier interactions in a mean-field approach by using the potential of a point charge calculated from the Poisson-Boltzman relation in place of Eq. 5.29. For simplicity, we proceed with the simplified model in Eq. 5.29. A model that treats carrier interactions exactly will be presented in Chapter 5.2.3.

In order to compute the charge propagator $K(\mathbf{k}, f)$, we use Fick's law of diffusion,

$$\partial_t N(\mathbf{r}, t) = D \bigtriangledown^2 N(\mathbf{r}, t). \tag{5.30}$$

where D is the diffusion constant. Taking a spatial Fourier transform in x and in y, we have

$$\partial_t N(\mathbf{k}, t) = -D(2\pi k)^2 N(\mathbf{k}, t). \tag{5.31}$$

where $k = \sqrt{k_x^2 + k_y^2}$. The solution to Eq. 5.31 is

$$N(\mathbf{k}, t) = N(\mathbf{k}, 0) e^{-4\pi^2 D k^2 t}. \tag{5.32}$$

The propagator (or Green's function) is the solution $K(\mathbf{r}, t) = N(\mathbf{r}, t)$ subject to the initial condition $N(\mathbf{r}, 0) = \delta(\mathbf{r})$. Inserting the Fourier transform of a delta function for $N(\mathbf{k}, 0)$ gives

$$\begin{aligned} K(\mathbf{k}, t) &= e^{-4\pi^2 D k^2 t - \lambda t} \int d\mathbf{r} e^{2\pi i \mathbf{k} \cdot \mathbf{r}} \delta(\mathbf{r}) \\ K(\mathbf{k}, t) &= e^{-4\pi^2 D k^2 t}. \end{aligned} \tag{5.33}$$

Taking a temporal Cosine transform, we have

$$\begin{aligned} K(\mathbf{k}, f) &= 4 \int_0^\infty dt \cos(2\pi f t) K(\mathbf{k}, t) \\ K(\mathbf{k}, f) &= 4 \Re \left[\int_0^\infty dt e^{i 2\pi f t} e^{-4\pi^2 D k^2 t} \right] \\ K(\mathbf{k}, f) &= 4 \frac{4\pi^2 D k^2}{(4\pi^2 D k^2)^2 + (2\pi f)^2}. \end{aligned} \tag{5.34}$$

The prefactor of 4 ensures that we are calculating the noise spectrum as defined in Eq. 2.7, which also contains a prefactor of 4. Combining Eq. 5.28, Eq. 5.29, and Eq. 5.34, and integrating from 0 to 2π over the polar angle of $\mathbf{k}$, we obtain an expression for the power spectrum of the potential between heights z_1 and z_2,

$$P_{\delta\phi(z_1), \delta\phi(z_2)}(f) = 8\pi c_a \int \frac{dk}{k} \frac{4\pi^2 D k^2}{(4\pi^2 D k^2)^2 + (2\pi f)^2} \left(\frac{q}{4\pi\epsilon_0} \right)^2 e^{-2\pi k (z_1 + z_2)}. \tag{5.35}$$

Inserting this result into Eq. 2.56, we find that the cantilever frequency noise is given by

$$P^{\text{diff}}_{\delta f_c}(f,d) = \frac{2\pi c_a f_c^2 (V_{\text{ts}}-\phi)^2 d^2}{D k_c^2}\left(\frac{q}{4\pi\epsilon_0}\right)^2 \times \\ [C''^2 I_0 - 4C'C'' I_1 + 4C'^2 I_2 + 2CC'' I_2 - 4CC' I_3 + C^2 I_4] \tag{5.36}$$

with

$$I_n = d^{-n}\int_0^\infty d\alpha \frac{\alpha^{n+1}e^{-2\alpha}}{\alpha^4 + (2\pi f d^2/D)^2} \tag{5.37}$$

where we used the shorthand notation $C = C(d)$ for the capacitance of the spherical cantilever tip. We see that the frequency noise in Eq. 5.36 is proportional to charge density and quadratic in tip-sample voltage. The quadratic dependence on voltage arises because the theory assumes that the cantilever only observes, but does not alter the fluctuations it aims to measure. The proportionality in charge density follows from the assumption that the charger carriers are non-interacting, i.e. that they diffuse freely.

To ensure charge neutrality, we considered the presence of image charges on the other side of the dielectric. Here we assumed that for every charge at $(x, y, 0)$ in the active region of the transistor, there is an equal and opposite charge at $(x, y, -h_{\text{diel}})$ on the other side of the dielectric where h_{diel} is the thickness of the dielectric. To account for the presence of the image charge, we modified the potential in Eq. 5.29 as follows

$$\tilde{\phi}^{\text{im}}(k_x, k_y, z) = \frac{q}{2\epsilon_0 k}\left(e^{-2\pi z k} - e^{-2\pi z_{\text{eff}} k}\right). \tag{5.38}$$

where $z_{\text{eff}} = z + h_{\text{diel}}\epsilon_{diel}^{-1}$ is the effective distance from the cantilever tip to the image charge, and ϵ_{diel} is the dielectric constant of the dielectric layer, here silicon oxide. Using the potential in Eq. 5.38, we reproduce Eq. 5.36, but with a modified I_n,

$$I_n^{\text{im}} = d^{-n}\int_0^\infty d\alpha \frac{\alpha^{n+1}e^{-2\alpha}}{\alpha^4 + (2\pi f d^2/D)^2}\left(1 - e^{-\frac{\alpha h_{\text{diel}}}{\epsilon_{\text{diel}} d}}\right)^2. \tag{5.39}$$

In order to compute the carrier density c_a, we assume that the active region and the back-gate form a parallel plate capacitor with a silicon oxide dielectric between them. The

carrier density can then be computed as

$$\begin{aligned} c_a &= C_i(V_G - V_t)/q \\ C_i &= \frac{\epsilon_{\mathrm{SIO}_2}\epsilon_0}{h_{\mathrm{SIO}_2}}, . \end{aligned} \tag{5.40}$$

where q is the unit charge, C_i is the capacitance per unit area across the dielectric, h_{SIO_2} its thickness, and $\epsilon_{\mathrm{SIO}_2}$ its relative dielectric constant. For a 315 nm thick oxide film, we have $C_i = 4.65\epsilon_0/315 \text{ nm} = 1.3 \times 10^{-4} \text{ Fm}^{-2}$.

5.2.3 Frequency Noise due to Interacting Charges

The lack of agreement between the observed frequency noise and that predicted by free diffusion calls for a theory that takes inter-carrier interactions into account. Swapna Lekkala and Roger F. Loring developed such a theory based on an electrodynamic approach. [2] The field fluctuations are computed for carriers embedded in a semi-infinite dielectric. The calculation is exact and accounts for carrier interactions as well as dielectric screening. To compute the power spectrum of the contact potential between two locations, z_1 and z_2, the same linear response approach is used as in Chapter 3, i.e.

$$P_{\delta\varphi}(z_1, z_2, f) = \frac{-4k_BT}{2\pi f}\mathrm{Im}\left(\frac{\tilde{\phi}(z_2, f)}{\tilde{q}(z_1, f)}\right) \tag{5.41}$$

where

$$\tilde{\phi}(z, f) \equiv \int_0^\infty dt e^{-i2\pi ft}\langle\varphi(z, t)\rangle. \tag{5.42}$$

The electric potential $\tilde{\phi}(z_2, f)$ induced by a test charge $\tilde{q}(z_1, f)$ is calculated from Maxwell's equations,

$$\begin{aligned} \bigtriangledown \times \mathbf{E} &= -2\pi i f \mu_0 \mathbf{H} \\ \bigtriangledown \times \mathbf{B} &= 2\pi i f \epsilon_0 \epsilon_{\mathrm{rel}}(f)\mathbf{E} + \mathbf{J} \\ \epsilon_0\epsilon_{\mathrm{rel}}(f) \bigtriangledown \cdot \mathbf{E} &= n \equiv e(n_+ + n_-). \end{aligned} \tag{5.43}$$

where $\epsilon_{\rm rel}(f) = \epsilon(f)/\epsilon_0$. All quantities are frequency-dependent, resulting from a temporal Fourier-Laplace transform of the form $\int_0^\infty dt e^{-2\pi i f} \dots$. The spatially-varying number densities of positively and negatively charged carriers are $n_\pm$. To construct closed equations for the fields in the medium, we assume that the current is the sum of a term from Ohm's law embodying the interaction among charge carriers and a term from Fick's law representing thermal fluctuations in charge carrier density,

$$\mathbf{J} = \sigma_0 \mathbf{E} - D \bigtriangledown n. \tag{5.44}$$

As a simplifying assumption, the diffusion coefficient is taken to be the same for both species. The statement in Eq. 5.14 represents our model, and introduces parameters σ_0 and D whose definition in terms of microscopic parameters requires the construction of an underlying microscopic model.

Swapna Lekkala and Roger F. Loring have solved Eq. 5.43 and Eq. 5.14 for a point charge q located in vacuum a distance z_1 above a semi-infinite dielectric with dielectric function $\epsilon(\omega)$ in order to compute the electrostatic field $\mathbf{E}$ a distance $z_2 - z_1$ immediately above or below the point charge, as sketched in Figure 3.4. The coordinate system is chosen such that the vacuum-dielectric interface is located in the xy-plane and such that the point charge is at $(x, y, z) = (0, 0, z_1)$. Appropriate boundary conditions were used at the interface between the dielectric and the vacuum to solve for the electric field $\mathbf{E}$. The quantity of interest is the reaction electric field $\mathbf{E}_{\rm rxn} = \mathbf{E} - \mathbf{E}_q$ that is generated by the dielectric. Here $\mathbf{E}$ is the total electric field and $\mathbf{E}_q$ is the field generated by the charge q alone, in the absence of the dielectric. The electrostatic potential is calculated from

$$\tilde{\varphi}(0, 0, z_2, f) = \int_0^\infty dz \mathbf{E}(0, 0, z) \tag{5.45}$$

where we have taken the potential to vanish at $z \to \infty$. The power spectrum of the correlation function of the electrostatic potential at positions z_1 and z_2 is computed from Eq. 5.41

to be [2]

$$
\begin{aligned}
P_{\delta\varphi}(z_1, z_2, f) &= \frac{-4k_BT}{2\pi f(4\pi\epsilon_0)}\mathrm{Im}\int_0^\infty d\alpha e^{-\alpha(z_1+z_2)/d}\left(\frac{\epsilon_{\mathrm{rel}}-\theta}{\epsilon_{\mathrm{rel}}+\theta}\right)\\
\theta &= \left(\frac{1}{1-\eta}\right)\left(1-\eta\left(\frac{\alpha}{\sqrt{\alpha^2+2\pi i f(1-\eta)/\Omega_d}}\right)\right),\\
\eta &= \frac{i\Omega}{2\pi i f\epsilon_{\mathrm{rel}}(f)},\\
\Omega_d &= \frac{D}{d^2},\\
\Omega &= \frac{\sigma_0}{\epsilon_0}.
\end{aligned}
\tag{5.46}
$$

The voltage noise generated above the vacuum-medium interface by interacting charge carriers and dielectric fluctuations is expressed in terms of the conductivity σ_0, the carrier diffusion coefficient D, and the dielectric function $\epsilon_{\mathrm{rel}}(f)$. The voltage noise can also be expressed in terms of three unitless quantities, f/Ω, f/Ω_d, and a complex valued dielectric function ϵ_{rel}. One can express the noise in Eq. 5.46 in terms of the carrier density using

$$
\sigma_0 = 2\bar{n}e\mu \tag{5.47}
$$

where μ is the charge mobility and $\bar{n}$ the constant mean carrier density (in units of 1/Volume) of either charge. The factor of 2 results from counting both species. It is important to note that the noise generated in Eq. 5.46 is a combination of noise generated by dielectric fluctuations and noise generated by charge carrier motion. If the conductivity σ_0 is set to zero, i.e. $\bar{n}=0$ or $\eta=0$, Eq. 5.46 reduces to the noise predicted due to dielectric fluctuations above a semi-infinite slab [1, 17, 50], i.e. the result in Eq. 3.5 in the limit of an infinitely thick film ($h\to\infty$). On the other hand, if we remove the dielectric by setting $\epsilon_{\mathrm{rel}}=1$, and expand the resulting expression to lowest order in carrier density $\bar{n}$, we obtain

$$
\begin{aligned}
P_{\delta\varphi}(z_1, z_2, f) &= \left(\frac{4\bar{n}e\mu}{4k_BT\pi\epsilon_0^2(2\pi f)^2 d}\right)\\
&\times \mathrm{Re}\int_0^\infty dy e^{-y(z_1+z_2)/d}\left(\frac{\sqrt{y^2+2\pi i d^2/D}-y}{\sqrt{y^2+2\pi i d^2/D}}\right),
\end{aligned}
\tag{5.48}
$$

where we have used the Einstein relation, $\mu = eD/k_BT$. Lekkala and coworkers have shown that this result is equivalent to what one obtains from charges of density $2\bar{n}$ freely diffusing in a semi-infinite slab [2]. The two approaches agree only at low carrier densities (when $|\eta| \ll 1$), a regime in which charge interactions can be ignored. The value of $|\eta|$ has a physical interpretation: $|\eta|^{-1}$ is the ratio of the thermal energy k_BT of a single carrier and total Coulomb energy between that carrier and the $N \approx nL^3$ charges located within a diffusion length $L \approx \sqrt{D/f}$. For $|\eta| \ll 1$, the thermal energy k_bT dominates, so that Coulomb interactions can be ignored. Alternatively, one can think of $|\eta|$ as the ratio the Debye screening length $\approx \sqrt{\epsilon_0 k_B T/\bar{n}e^2}$ and the diffusion length L. For $|\eta| \gg 1$ carriers are effectively screened by the neighboring charges.

In Figure 5.11 we show the predicted cantilever frequency noise spectrum induced by semiinfinite slab of interacting as well as non-interacting carriers in vacuum. There are three characteristic frequencies, [2]

$$\begin{aligned} f_1 &\approx \sqrt{\frac{\Omega_d}{\Omega}}\left(\frac{\Omega''}{2pi}\right) \\ , f_2 &\approx \frac{\Omega'}{2\pi}, \\ f_3 &\approx \frac{\Omega^2}{2\pi\Omega''} \end{aligned} \tag{5.49}$$

where

$$\begin{aligned} \epsilon_{\mathrm{rel}}(f) &= \epsilon'_{\mathrm{rel}}(f) - i\epsilon''_{\mathrm{rel}}(f) \\ \Omega'(f) &\equiv \frac{\Omega\epsilon'_{\mathrm{rel}}(f)}{|\epsilon_{\mathrm{rel}}(f)|^2}, \\ \Omega''(f) &\equiv \frac{\Omega\epsilon''_{\mathrm{rel}}(f)}{|\epsilon_{\mathrm{rel}}(f)|^2}. \end{aligned} \tag{5.50}$$

The frequency f_2 is related to the parameter $\eta = f_2/f$ that determines the importance of carrier interactions. For frequencies $f \gg f_2$ ($\eta \ll 1$), carrier interactions can be ignored. This finding is evident in Figure 5.11. At frequencies $f \gg f_2$ the model that takes carrier

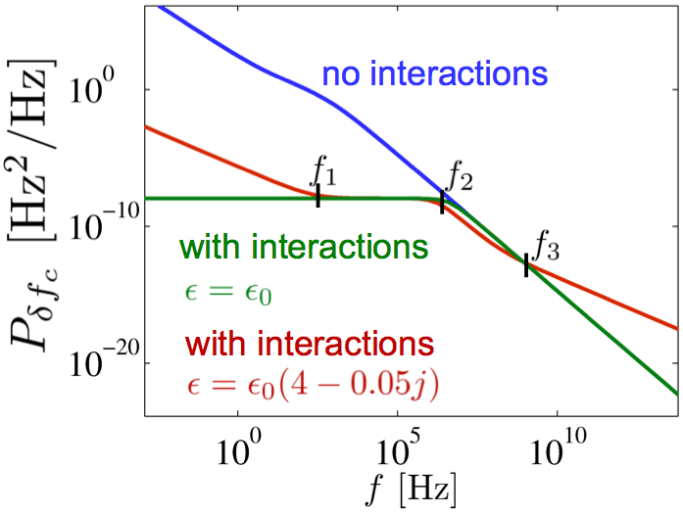

Figure 5.11: Spectral density of cantilever frequency noise 100 nm above a semi-infinite slab of interacting carriers in a dielectric (red; $\epsilon = (4 - 0.005j)\epsilon_0$), interacting carriers in vacuum (green; $\epsilon = \epsilon_0$), and non-interacting carriers in vacuum (blue; $\epsilon = \epsilon_0$). Eq. 5.46 and Eq. 5.48 were used to compute the frequency noise for the interacting and the non-interacting carriers, respectively. A carrier density of 5×10^{24} m^{-3} was used for this calculation. The charge density was obtained by raising the areal charge density estimated above for the transistor to the power 3/2, thus corresponding to a comparable mean inter-carrier separation with the assumption that the carriers in the transistor occupy a rigorously two-dimensional region. The Einstein relation was invoked to compute the diffusion constant from a mobility of $\mu = 10^{-10}$ m^2/Vs. Parameters: $k_c = 0.34$ N/m, $f_c = 58.5$ kHz, $V_{\text{ts}} = -5$ V.

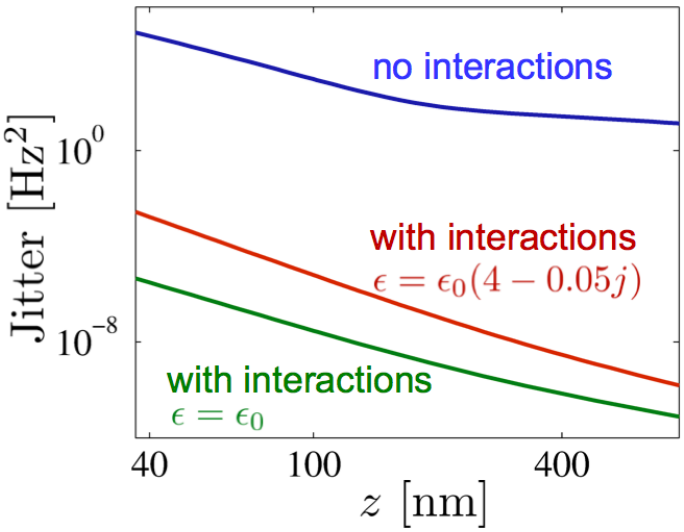

Figure 5.12: Cantilever frequency noise as a function of tip-sample distance above a semi-infinite slab of interacting carriers in a dielectric (red; $\epsilon = (4 - 0.005j)\epsilon_0$), interacting carriers in vacuum (green; $\epsilon = \epsilon_0$), and non-interacting carriers in vacuum (blue; $\epsilon = \epsilon_0$). The frequency noise was integrated from 0.2 Hz to 3 Hz. The parameters used in this calculation can be found in the caption of Figure 5.11.

interactions into account agrees with the simplified model in Eq. 5.48. At frequencies $f \ll f_2$, on the other hand, the two models disagree. Inclusion of carrier interactions in this regime is found to reduce the frequency noise by several orders of magnitude. In Figure 5.12 we show the frequency noise integrated over an experimentally relevant frequency range (0.2 Hz to 3.0 Hz) as a function of distance above a slab of charge carriers. We find that carrier interactions suppress frequency noise by several orders of magnitude in the experimentally relevant frquency regime.

In Figure 5.11 we show the frequency noise due to interacting carriers in a dielectric. We see that the presence of a dielectric significantly contributes to frequency noise for $f \ll f_1$ and $f \gg f_3$. We interpret the additional noise as arising form dielectric fluctuations. For $f \gg f_3$, dielectric-induced noise dominates over carrier-induced noise because charge carriers are essentially frozen into place on sufficiently short time scales. For $f \ll f_1$ carrier-induced noise is negligible because it is suppressed by carrier-interactions. Somewhat surprisingly, dielectric fluctuations are suppressed by the presence of charge carriers as well, at least in the regime $f < f_1$. In this regime, the observable noise decreases with increasing carrier density.

In order to observe stochastic motion of charge carriers as a frequency noise, one must be able to detect the predicted fluctuations at a frequency $f_1 < f < f_3$, or more ideally at $f_2 < f < f_3$. Looking at Figure 5.11, we conclude that such a measurement may be impossible because the experimentally accessible frequencies are of the order $f \approx 1$ Hz $\ll f_1$. Moreover, the comparatively-large thermal noise floor of a commercial cantilever of typically $P_{\delta f_c} \approx 10^{-5}$ Hz^2/Hz prohibits measuring carrier-induced noise. Instead of observing frequency noise, one may consider measuring friction, which is sensitive to fluctuations at the cantilever resonance frequency f_c, thus enabling access to motion in a much higher frequency

regime. While more work is needed on this subject, we suspect that such a measurement would still suffer from insufficient signal-to-noise.

The dielectric constant $\epsilon = (4 - 0.005j)\epsilon_0$ used to generate Figure 5.11 is only a rough guess and does not equal the actual dielectric constant in either P3HT and TPD. In principle, the dielectric function in these conducting materials could be measured using an impedance spectrometer by sandwiching either P3HT or TPD between two metal plates, as described in Chapter 3. In practice, however, such a measurement would be obscured by background charge carriers present in either P3HT or TPD. With or without such background carriers present, such a measurement would by the dissipation-fluctuation theorem yield exactly the necessary information to calculate voltage fluctuations accross such a sandwiched device. Unfortunately, such a calculation does not contain the parameter d and thus cannot be used to compute, nor estimate, cantilever frequency noise a distance d above the semiconductor.

The theory presented in Eq. 5.46 models the material as a semi-infinite slab, and so is not directly applicable to the transistor data in Figure 5.8 and Figure 5.10. We can, however, use the electrodynamic calculation as a qualitative guide to show that at the charge densities present in our experiment charge carrier interactions are indeed responsible for the suppression of chage-induced noise by several orders of magnitude. While in Figure 5.11 we see that the low frequency dielectric noise is suppressed by carrier interactions as well, this need not be the case for a transistor geometry. Dielectric fluctuations over the transistor are generated throughout the organic film, whereas the charge carriers are confined to the first few monolayers near the bottom of the film. We therefore do not expect dielectric fluctuations over an organic transistor to be significantly suppressed by carrier interactions. This finding suggests that the observed fluctuations over both TPD and P3HT transistors may be explained entirely in terms of dielectric fluctuations alone - in the absence of charge

carriers. A purely dielectric origin of the noise would explain why the data in Figure 5.8 are independent of charge carrier density (i.e gate voltage). From Chapter 3, we saw that as long as the dielectric function $\epsilon(f)$ is frequency independent, the dielectric-induced frequency noise is $1/f$, consistent with the data in Figure 5.7. While the theory presented here does not directly apply to the geometry of the transistor, it does explain why a model of non-interacting charge carriers grossly overestimates the observed noise.

5.2.4 Conclusions

The observed cantilever frequency noise over an OFET is several orders of magnitude smaller than what is predicted by a model of freely diffusing carriers, and thus at odds with microscopic models of charge transport that ignore charge-charge interactions. In Section 5.2.3 we have established a theoretical framework for studying electrical noise in molecular organic semiconductors with a model that includes inter-carrier interactions. The electrodynamic theory presented here qualitatively explains the observed noise over a TPD transistor, suggesting that charge carrier interactions can indeed suppress the noise spectrum induced by carrier motion. The quantitative analysis of cantilever frequency noise from a thin semiconductor film must await the application of the model analyzed here to that geometry. The previous quantitative treatment of cantilever frequency noise [1, 17, 50] from dielectric fluctuations in the absence of mobile charges supports the prospect that a quantitative treatment of this observable in the presence of free charge can also be achieved.

5.3 Determination of the Charge Mobility by Electric Force Microscopy using Time-of-Flight

We here propose using cantilevers to measure the charge mobility in an organic field effect transistor (OFET) by combining time-of-flight (TOF) with electric force microscopy. While cantilevers have, to our knowledge, not yet been used in TOF experiments, the idea of introducing cantilevers into bulk measurement techniques is not new. For example, it has been demonstrated that mass spectrometry can be done locally with cantilevers [157]. Using cantilevers to study charge transport in both organic (see Section 5.1) and inorganic electronics is also not new either. The challenge for performing such measurements in inorganic electronics is the high frequencies involved, which are typically a few GHz. This challenge is commonly overcome by heterodyning the high frequency signal by applying a high frequency voltage to the cantilever tip. With this technique Leyky and other authors have analyzed electronic circuits at frequencies near 100 GHz in an electric force microscope experiment [158–160]. More recently, Coffey and coworkers introduced a time-resolved electric force microscopy technique that does not rely on heterodyning and have achieved a 100 μs time resolution while at the same time maintaining a spatial resolution of 100 nm in a polymer solar cell [94]. Electronic circuits have also been analyzed using near-field-scanning-optical microscopy (NSOM). Using modified cantilevers, Weide and coworkers have extended the operating regime of NSOM, which is usually in the visible regime, down to DC - 0.1 THz, thus enabling them to study electronic circuits [161, 162]. Given the effort that has been expended to study charge motion in electronics with cantilevers and given that there is already precedent for combining cantilever measurements with bulk measurement techniques, it is quite surprising that cantilevers have not yet been used to measure charge mobility by TOF.

Our proposed experiment builds on prior work on organic electronic ratchets by Roeling and coworkers [34, 163, 164] who demonstrated that charge in an OFET can be funneled from the source to the drain electrodes without applying a source-drain bias. The charge is displaced laterally by applying a cyclic series of voltages to underlying interdigitated gate electrodes. The time scale for charge to equilibrate in such an experiment is given by [163, 165]

$$\tau = \frac{L^2}{V_G \mu} \tag{5.51}$$

where μ is the charge mobility, V_G the voltage on the gate electrodes and L is a length scale as indicated in Figure 5.14. Measuring τ amounts to determining the charge mobility μ. While Roeling and coworkers only measured the net current from the source to the drain electrodes, we here propose to observe the induced lateral charge motion locally using an electric force microscope. To this means, we have fabricated transistor substrates with two underlying gate electrodes (see Figure 5.13). More detail on the fabrication of these devices can be found in Appendix B. A sketch of the proposed experimental setup is shown in Figure 5.14. Initially, a non-uniform charge density is placed in the channel by a applying a set of voltages V_{G1} and V_{G2} to the gate electrodes. At time $t = 0$ the voltages on the gate are set equal to one another, i.e. $V_{G1} = V_{V2}$. We then observe the resulting displacement of charge in an electric force microscope experiment as a transient shift in the cantilever resonance frequency. The time scale of this transient response can be estimated from Eq. 5.51. For a length scale $L = 3.5$ μm, a mobility for TPD of $\mu = 10^{-10}$ m^2/Vs, and a gate voltage $V_G = 10$ V, we estimate the time scale of the transient response to be $\tau = 12$ ms. The length scale $L = 3.5$ μm is that of a prototype device. L was chosen to be much shorter than the fine scan range of 25 μm of our nanopositioners. To estimate the magnitude of the frequency shift, we take the instant change in the contact potential to be equal to instant change in

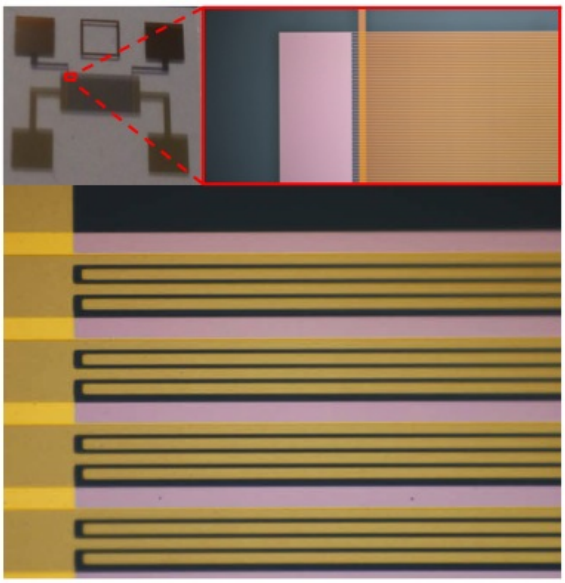

Figure 5.13: Images of the fabricated transistor substrate with top Au source and drain electrodes (pink) and underlying Pt gate electrodes (yellow). The gate electrodes are 2.25 m long and spaced by only 1 μm. The four square pads in the top-left image are 3 mm wide on each side.

the gate voltage, i.e. $\Delta\phi = \Delta V_G$. The frequency shift is quadratic in voltage, i.e.

$$\Delta f_c = \alpha(V_t - \phi)^2. \tag{5.52}$$

From the data in Figure 5.9 we estimate $\alpha \approx 5$ Hz/V^2 for a cantilever ≈ 100 nm above a TPD transistor. For a shift in the contact potential of $\Delta\phi = \Delta V_G \approx 10$ V, we expect the cantilever resonance frequency to change by

$$\Delta f_c \approx 500 \text{ Hz}. \tag{5.53}$$

For the experiment to be feasible, we must be able to measure the cantilever resonance frequency several times, say $N \approx 10$ times, within a time τ. From Eq. 2.29, the signal-

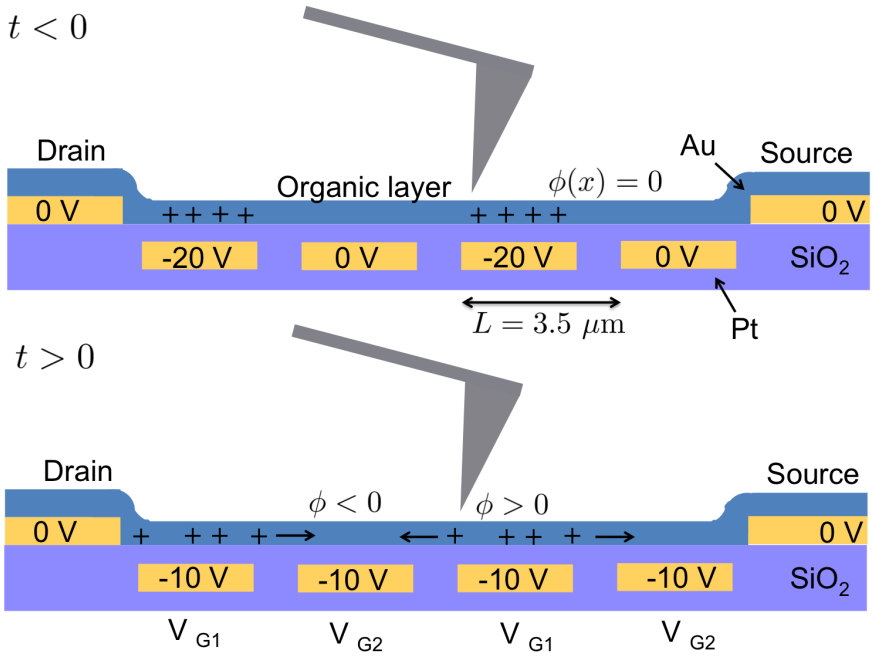

Figure 5.14: A sketch of the proposed experiment. At time $t < 0$, the applied gate voltages, V_{G10} and V_{G20}, are different. At steady state, the electric potential in the channel is constant and equal to zero, and the charge distribution is inhomogeneous. At $t = 0$, we set $V_{G1} = V_{G2} = (V_{G10} + V_{G20})/2$. As a result, charge moves laterally away from the initially highly charged regions until a new steady state is reached. The magnitude of the final gate voltages are chosen to minimize charge injection at the source/drain electrodes. We propose to measure the transient shift in the electrostatic potential by recording the frequency shift of a electric force microscope cantilever.

to-noise ratio (SNR) for resolving the cantilever resonance frequency in a time $T = \tau/N$ is

$$SNR = \frac{\Delta f_c}{\sqrt{2\int_0^{\frac{N}{2\tau}} df P_{\delta f_c}(f)}} \tag{5.54}$$

where $P_{\delta f_c}(f)$ is the cantilever frequency noise. From the data in Figure 5.7 we see that the frequency noise near $f = N/\tau \approx 1$ kHz is dominated by the instrumentation and is given by $P_{\delta f_c}(f) \approx cf^2$ where $c \approx 10^{-7}$ Hz^{-1}. The signal-to-noise ratio (SNR) can then be estimated as

$$\begin{aligned} SNR &\approx \alpha V_G^2 \sqrt{\frac{12(\frac{\tau}{N})^3}{c}} \\ SNR &\approx \frac{\sqrt{12}\alpha V_G^2 \tau^{3/2}}{c^{1/2} N^{3/2}} \\ SNR &\approx \frac{\sqrt{12}\alpha V_G^{1/2} L^3}{\mu^{3/2} c^{1/2} N^{3/2}} \\ SNR &\approx 235. \end{aligned} \tag{5.55}$$

The large SNR ratio demonstrates the feasibility of the experiment. Because the SNR ratio decreases with increasing mobility, this technique is most suitable for low mobility OFETs. We note that the SNR can be increased further by fabricating a device with a larger channel length L. Another way to increase the SNR is to use to a lock-in detection scheme in which a sinusoidal voltage of frequency f_m is applied to the gate electrodes. The resulting oscillatory electrostatic potential can be detected as a function of f_m and the mobility determined from the shape of the frequency response. In order to avoid detector noise, which usually dominates at high frequencies, one can apply a sinusoidal voltage to the cantilever at frequency $f_m/2$, thereby mixing (or heterodyning) the signal down to DC. Apart from avoiding detector noise, the lock-in method also enables performing measurements for an extended period of time rather than trying to obtain signal from a single transient measurement.

The charge mobility can only be extracted from such measurements if a model is in place that accurately describes charge motion within the transistor. In order to solve the electrostatics within the transistor, we make use of charge conservation, Fick's law of diffusion, and Poisson's law. If motion takes place in only one dimension, we have [34]

$$\frac{\partial \rho_A}{\partial t} = -\frac{\partial J_A}{\partial x} \tag{5.56}$$

$$J_A = -D\frac{\partial \rho_A}{\partial x} + \mu \rho_A E_x \tag{5.57}$$

$$\frac{\partial E_x}{\partial x} = \frac{\rho_A}{\epsilon_r \epsilon_0} \tag{5.58}$$

where J_A is the areal current density, ρ_A the areal charge density, E_x the electric field along x, and ϵ_r the relative dielectric constant. Roeling and coworkers have solved Eq. 5.56, Eq. 5.57, and Eq. 5.58 with the appropriate boundary conditions at the back gate electrodes. Efforts of solving Eq. 5.56, Eq. 5.57, and Eq. 5.58 with similar boundary conditions appropriate for our device are ongoing in our laboratory. Once these calculations are completed, we believe we will have the necessary theoretical framework to extract the charge mobility in the organic layer from the time scale of the charge response.

Chapter 6

Fabrication of Radio-Frequency Cantilevers for Scanned Probe Microscopy

6.1 Motivation

Scanning probe microscopy is a valuable technique for studying properties of thin organic films, such as charge trapping in organic field-effect transistors (OFETs) [155] or dielectric fluctuations above thin polymer surfaces [1, 50]. The cantilevers used in such measurements typically have frequencies of no more than a couple hundred kilohertz. Unfortunately, many phenomena such as charge trapping in OFETs occur on a sub-microsecond timescale, too short to be easily imaged in real-time by the cantilevers conventionally used in scanning probe microscopy.

Switching to radio-frequency (RF) cantilevers, which have resonance frequencies in the MHz to GHz range, would enable studying these processes in real time. There is ample precedent for scanning probe microscopy using RF cantilevers [166–168]. While fast time resolution imaging has been achieved using lower-frequency (e.g. sub-MHz) cantilevers as well, for example by heterodyning [158–160] or by signal-averaging many time-transients [169], we believe that RF cantilevers enable a more direct measurement of fast processes. Another advantage of RF cantilevers is that we expect them to experience less surface induced friction Γ: Since Γ scales with resonance frequency f_c as $\Gamma \propto \epsilon''(f_c) f_c^{-1}$ [63], where ϵ'' is the imaginary part of the dielectric function, we expect less friction at a larger cantilever resonance frequency. RF cantilevers could also be used in magnetic resonance force microscopy (MRFM)

[18, 170–172]. MRFM using 0.8 MHz nanowires has already been achieved [173]. Performing MRFM with a MHz cantilever would facilitate detecting electron spin relaxation in real time using the cantilever-enabled-readout-of-magnetization-inversion-transients (CERMIT) protocol on nitroxide spin probes attached to proteins that have spin relaxation times of $T_{1,\rho} \approx 1$ ms -100 ms. [170, 174]

A number of different schemes exist to drive or detect the motion of an RF cantilever. The most extensively used techniques are magnetomotive, capacitive, piezoresistive detection, piezoelectric detection, and electron tunneling [175]. In the magnetomotive scheme, the cantilever is actuated (or driven) with a Lorentz force and its motion is transduced (or detected) as an electromotive force. The technique is broadband, but has the drawback that it requires large magnetic fields and suffers from sensitivity degrading backaction, as shown below. The capacitive technique is also capable of actuating and driving cantilevers, but does not require a magnetic field. The efficiency of this technique is impeded by parasitic impedances. The piezoresistive and piezoelectric methods provide a means to detect the motion of a cantilever. They make use of the change in the electrical properties due to the strain induced in the cantilever as it is deflected. The electron tunneling sensor detects a change in the tunneling current between the cantilever and a nearby electrode as the cantilever is deflected. The signal-to-noise-ratio of this technique is limited by shot noise in the current, by the instrumentation at low tunneling currents, and by a back-action force at large tunneling currents [175, 176]. The source of the back-action is the momentum imparted by the tunneling electrons. Optical detection of RF cantilevers is challenging due to their small size, which results in less reflected light. Optical techniques that overcome this challenge are Michelson interferometry [177] and Fabry-Perrot interferometry [178]. The latter makes use of an optical cavity, and the former uses the interference pattern of light reflected at the cantilever with that from a Ref. beam. Michelson interferometry was used by

J. Nichol and coworkers to observe silicon nanowires. [179] Using polarized light, the authors were able to enhance the signal-to-noise of their detection protocol.

6.2 Fabrication of Radio-Frequency Cantilevers

Radio-frequency cantilevers were fabricated at the Cornell Nanofabrication Facility (CNF). To fabricate doubly-clamped nitride cantilevers for magnetomotive detection, 600 nm of silicon dioxide was grown by thermal oxidation onto a $\langle 1\ 0\ 0 \rangle$ silicon wafer, followed by a low-pressure chemical vapor deposition of 250 nm of silicon nitride (see Figure 6.1a). Electron beam lithography was used to pattern the cantilevers as well as the allignment marks with a stack of metals (Cr 5 nm/ Au 35 nm/ Cr 10 nm/ Al 20 nm), as shown in Figure 6.1b. A similar stack of metals (Cr 5 nm/ Au 100 nm/ Cr 10 nm/ Al 20 nm), which functions as the electrical interconnect to the off-chip measuring apparatus, was patterned using optical lithography (see Figure 6.1c). A drawing of the electrical interconnects is shown in Figure 6.4. A layer of XHRi-16 was used to protect the aluminum from the developer. Using aluminum as an etch mask, the nitride cantilevers were defined by a reactive ion etch (nitride etch CHF_3/O_2, 8 min), as shown in Figure 6.1d. Finally, the cantilevers were released by removing the underlying oxide in a buffered hydrofluoric acid solution (BOE 6:1, 7 min), followed by a critical point drying process (see Figure 6.1d). The doubly-clamped cantilevers with adjacent electrodes for capacitive driving and detecting were also fabricated using the same recipe. Images of the resulting devices are shown in Figure 6.2. A typical cantilever is a few micrometers long and 100 nm wide. The nanofabrication recipe can be found in Appendix B.

The above recipe was also used to fabricated doubly-clamped cantilevers with tunnel

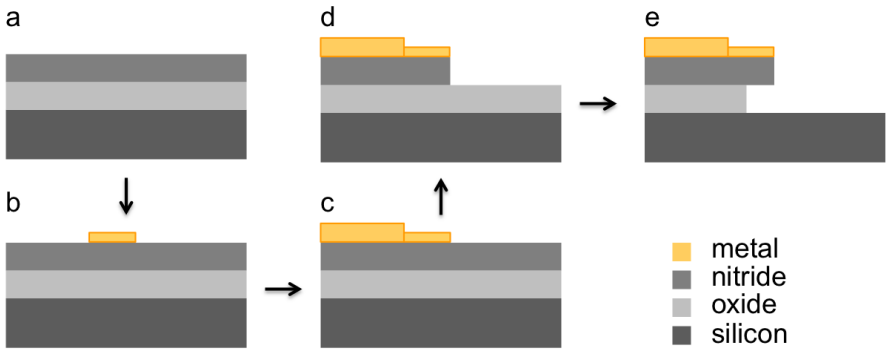

Figure 6.1: An illustration of the key steps for fabricating doubly-clamped nitride cantilevers.

junctions to adjacent electrodes (see Figure 6.3). While the fabrication of the cantilevers themselves was successful, problems were encountered when trying to fabricate tunnel junctions. Because the tunneling current drops off rapidly with distance, the junctions need to be very narrow (i.e. a few nanometers or less) in order for there to be sufficient tunneling current. Park *et al.* have demonstrated the fabrication of such junctions using a process called electromigration, whereby a small voltage is applied across a nanowire [180]. At voltages of typically a few hundred mV, Au atoms migrate across the nanowire and cause it to break at its narrowest point, producing a gap of a few nanometers or less [180]. The problems encountered with the fabrication of the tunnel junctions were twofold. First, we found that some of the cantilevers bent or buckled during the release process, which made it difficult to control the electrode cantilever distance precisely. The buckling occurred most likely due to internal stresses in the nitride, but may also have resulted from improper critical point drying. Second, we encountered difficulties removing the nitride immediately below the junctions using an isotropic nitride etch (BOE or SF_6).

Singly-clamped nitride cantilevers with adjacent electrodes were fabricated using a similar procedure, as outlined in Figure 6.5. The cantilevers are 100 nm wide and a few microme-

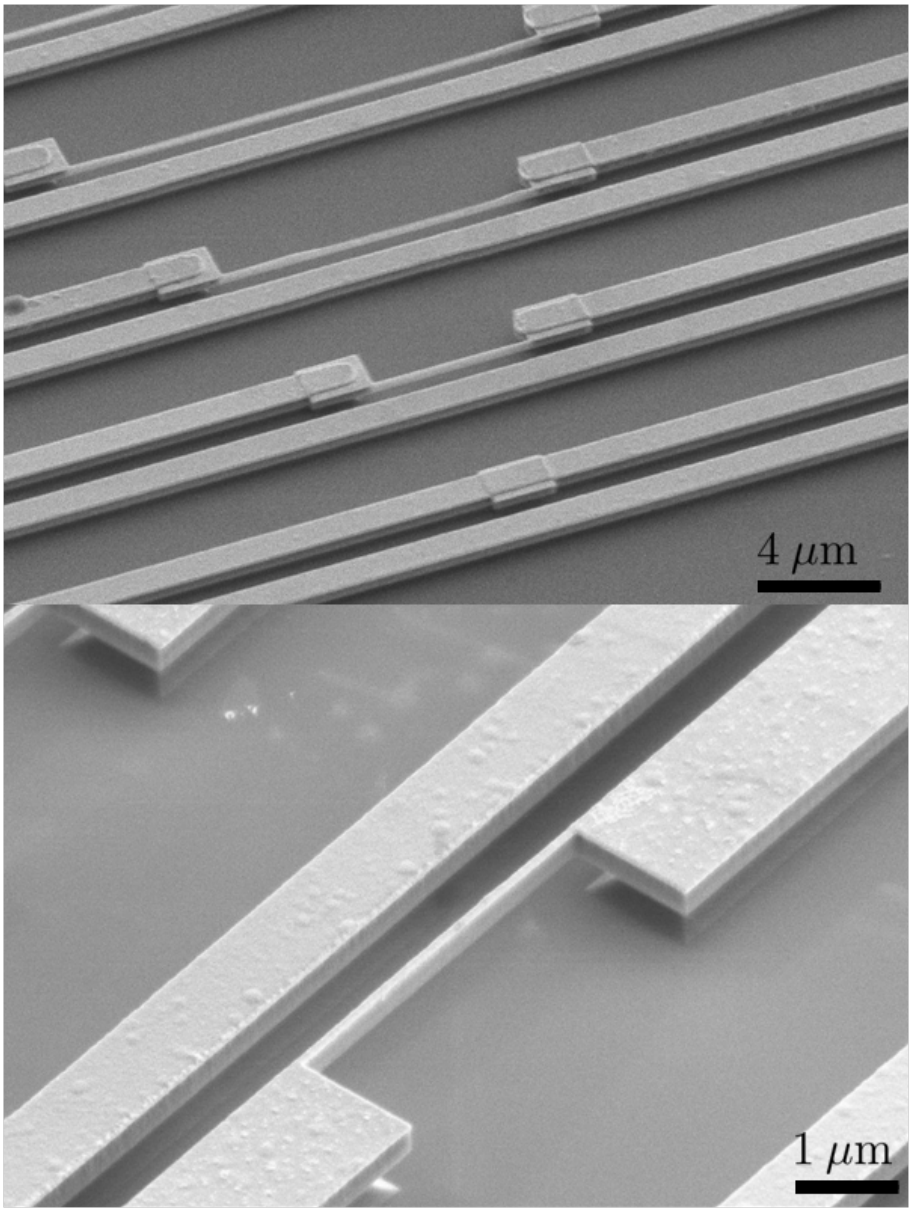

Figure 6.2: Scanning electron micrographs (SEM) of doubly-clamped RF cantilevers for magnetomotive actuation and detection. Top panel: Longer style cantilevers along with the optically patterned electrical interconnects. The electrodes near the cantilevers were originally designed to drive and detect the cantilevers capacitively. Unfortunately, the cantilever electrode distance is too large to make this experiment feasible. Bottom panel: A shorter style doubly-clamped cantilever. The material immediately underneath the electrodes is the oxide that remains after a wet etch in a buffered oxide etch (BOE) solution. Underneath the cantilever, this oxide is entirely removed.

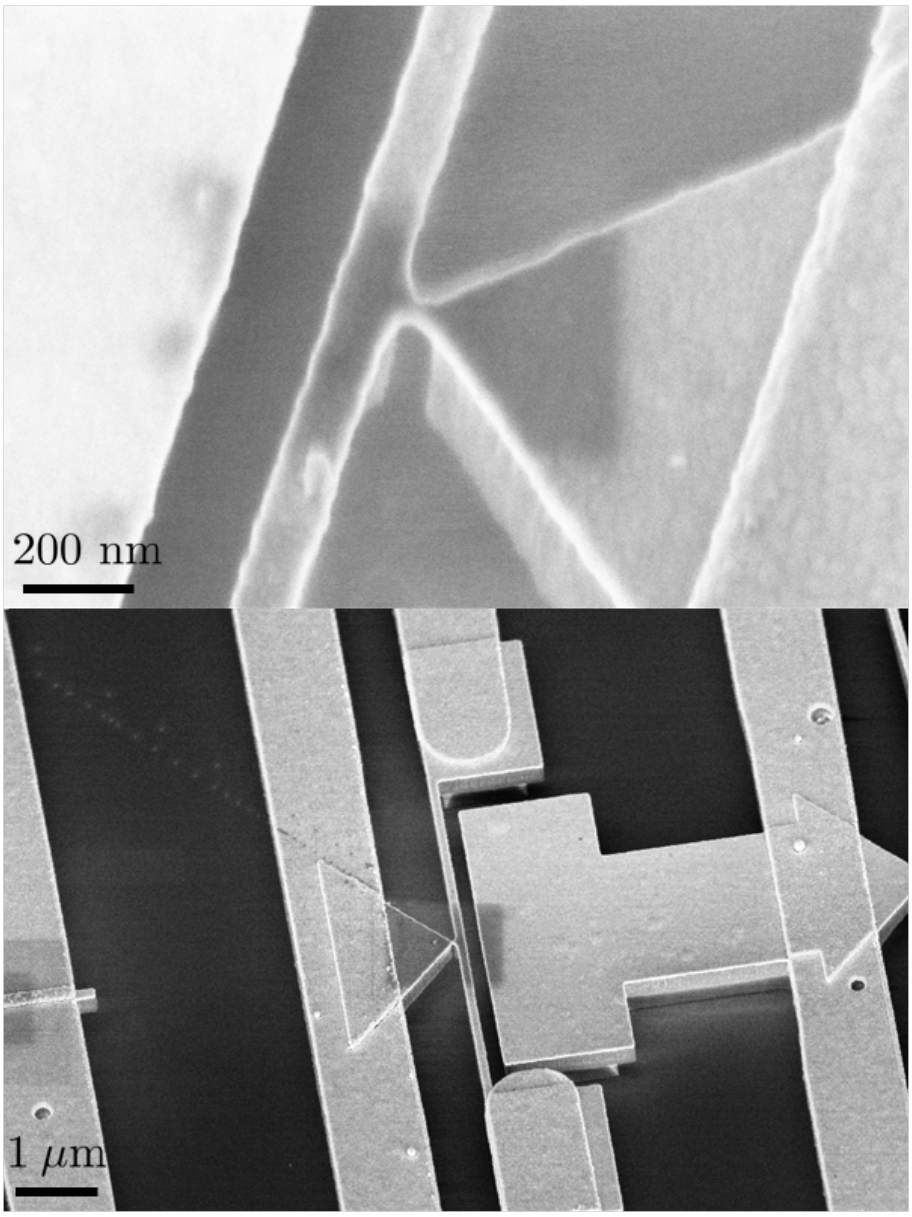

Figure 6.3: Scanning electron micrographs of doubly-clamped RF cantilevers with tunnel junctions (shown before initiating electromigration) along with the optically patterned electrical interconnects.

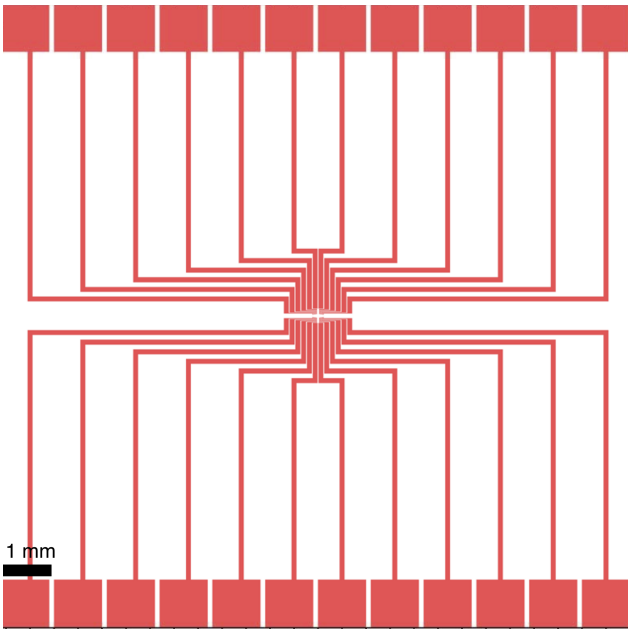

Figure 6.4: A drawing of the photolithography mask used to define the electrical interconnects for the doubly-clamped cantilevers.

ters long. 600 nm of silicon dioxide was grown by thermal oxidation onto a ⟨1 0 0⟩ silicon wafer, followed by a low-pressure chemical vapor deposition of 250 nm of silicon nitride (Figure 6.5a). Electron beam lithography was used to pattern the cantilevers and the adjacent electrodes with a stack of metals (Cr 5 nm/ Au 35 nm/ Cr 10 nm/ Al 20 nm), see Figure 6.5b. The purpose of the electrodes is to capacitively drive and detect the resonator [181]. We defined the cantilever block by photolithography. An XHRi-16 layer was used to protect the aluminum on the cantilevers and electrodes from degradation in the developer. Using the 2 μm thick photoresist and 20 nm of aluminum as etch masks, the cantilever block and the cantilevers were defined by reactive ion etching (nitride etch CHF_3/O_2, 8 min) the unprotected nitride (Figure 6.5c). Optical lithography (resist = nLOF 2020) was used to write the electrical interconnects (Cr 5 nm/ Au 100 nm) to the off-chip measuring apparatus (Figure 6.5d). The backside of the wafer was patterned with photoresist and etched all the way

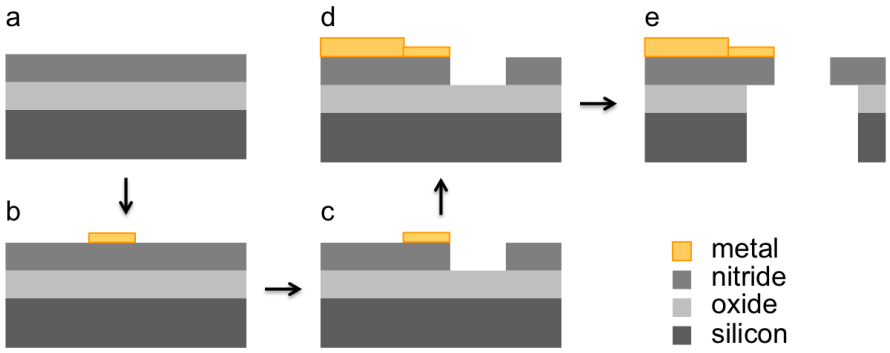

Figure 6.5: An illustration of the key steps for fabricating doubly-clamped nitride cantilevers.

to the oxide layer on the front side of the wafer using a Bosh etch process on the Unaxis 770. Finally, the cantilevers were released (Figure 6.5e) in a buffered hydrofluoric acid solution (BOE 6:1). While this process has not yet been implemented successfully, images of incomplete devices as well as a drawing of the photolithography features are shown in Figure 6.6 and Figure 6.7, respectively. The nanofabrication recipe can be found in Appendix B.

6.3 Mechanics of Doubly-Clamped Cantilevers

For magnetomotive actuation and detection, the cantilever is attached, or clamped, at both ends, as shown in Figure 6.9. In order to compute the mechanics of a doubly-clamped beam, we adopt a calculation from Ref. 182, where the mechanics of a singly-clamped beam are studied in detail. Because the different boundary conditions of doubly- and singly-clamped cantilevers lead to different eigenmodes, different resonance frequencies, and different spring constants, the calculation in Ref. 182 needs to be redone for doubly-clamped cantilevers. We start with the equation of motion for a uniformly driven beam, [183, 184]

$$m\partial_t^2 y + \alpha\partial_t y + EI\partial_x^4 y - T\partial_x^2 y = f(t). \tag{6.1}$$

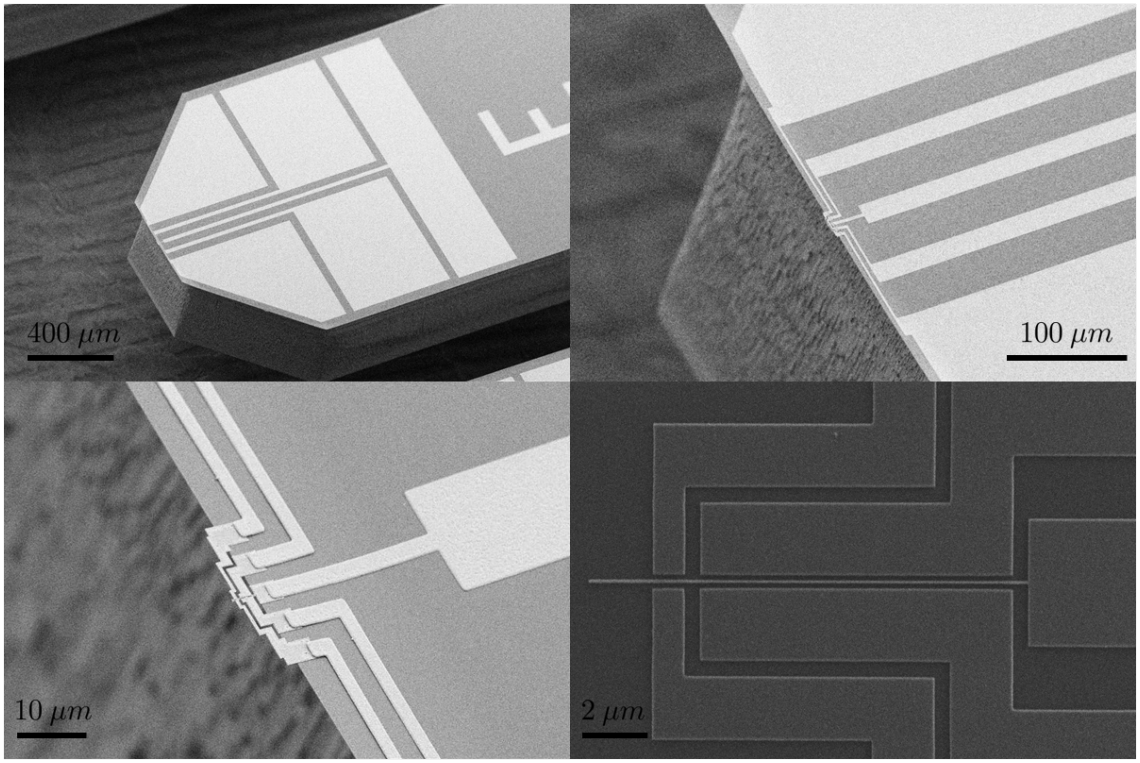

Figure 6.6: Scanning electron micrographs of a singly-clamped cantilever. The cantilever was designed to be used in a capacitive drive and detection scheme. There are five electrical connections, one leading to the cantilever and four leading to electrodes. The inner two electrodes are designed to drive the cantilever, while the outer two electrodes are designed to electrically isolate the cantilever from the surroundings. The bottom right panel shows an SEM right after patterning the cantilever and electrodes using electron beam lithography, immediately before performing the photolithography steps. The processing in the bottom left and in the top panels is complete. Unfortunately, the process failed because every cantilever on the wafer was positioned precisely along the stitch marks of the tool and was either printed doubly or not at all.

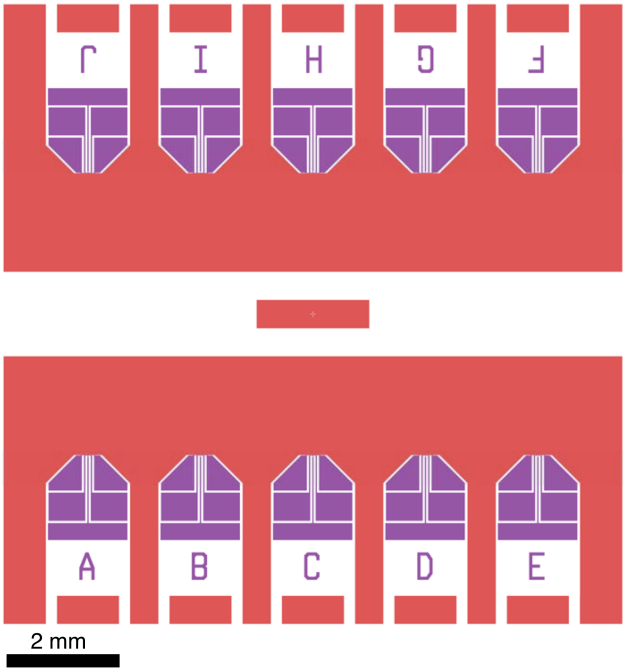

Figure 6.7: A drawing of the photolithography masks used for fabricating singly-clamped cantilevers. Shown are the cantilever dies as well as the electrical interconnects. Not shown are the features used for the backside processing.

Here $y(x,t)$ is the transverse deflection of the beam, m is the mass per unit length, α the coefficient of friction per unit length, E Young's modulus of elasticity, I the areal moment of inertia, and T the tension along the beam. The tension T in a beam of length L and cross-sectional area A arises due to the change in length ΔL of the beam as it is deflected out of equilibrium, and is given by

$$T = AE\frac{\Delta L}{L} \tag{6.2}$$

where

$$\Delta L = \int_{-L/2}^{L/2} \sqrt{1 + \left(\frac{\partial y}{\partial x}\right)^2}\, dx - L. \tag{6.3}$$

It is evident that the term $T\partial_x^2 y$ is cubic in y. Keeping only terms linear in y, we get

$$m\partial_t^2 y + \alpha\partial_t y + EI\partial_x^4 y = f(t). \tag{6.4}$$

Let's solve this equation by separation of variables, i.e.

$$y(x,t) = u(x)Y(t). \tag{6.5}$$

Unfortunately, it is very difficult to calculate $u(x)$ exactly. For that reason we will make the approximation that for the purpose of calculating $u(x)$, we can ignore the friction and driving terms in Eq. 6.4. In other words, we assume that the mode shape $u(x)$ is that of a frictionless freely oscillating beam. Dropping the friction and driving terms in Eq. 6.4 and separating out the spatial dependence, we obtain a differential equation for $u(x)$,

$$\frac{\partial_x^4 u(x)}{u(x)} = \text{ const} \equiv k^4. \tag{6.6}$$

Let's now apply the boundary conditions for a doubly-clamped beam, i.e.

$$u(-L/2) = u(L/2) = \partial_x u(-L/2) = \partial_x u(L/2) = 0. \tag{6.7}$$

For the fundamental mode, the result is

$$u(x) = c\left(\cos(kx)\cosh\left(\frac{kL}{2}\right) - \cosh(kx)\cos\left(\frac{kL}{2}\right)\right) \tag{6.8}$$

where

$$k \cong \frac{4.730041}{L}. \tag{6.9}$$

We'll chose the normalization constant c such that $Y(t)$ represents the position at the center of the beam ($x = 0$), which implies that

$$\begin{aligned} u(0) =& 1, \\ \Rightarrow c =& \frac{1}{\cosh kL/2 - \cos kL/2}. \end{aligned}$$

The normalized $u(x)$ is therefore

$$u(x) = \frac{\cos kx \cosh kL/2 - \cosh kx \cos kL/2}{\cosh kL/2 - \cos kL/2}. \tag{6.10}$$

The function $u(x)$ is graphed in Figure 6.8. We return to Eq. 6.4 and write it in terms of $u(x)$ and $Y(t)$.

$$m\partial_t^2 Y(t)u(x) + \alpha\partial_t Y(t)u(x) + EIk^4 Y(t)u(x) = f(t). \tag{6.11}$$

To eliminate the position dependence, we multiply by $u(x)$ and integrate over the beam. The resulting equation is that of a harmonic oscillator with effective mass M_{eff}, friction Γ_{eff}, spring constant k_{eff}, and force F_{eff}, i.e.

$$M_{\text{eff}}\partial_t^2 Y(t) + \Gamma_{\text{eff}}\partial_t Y(t) + k_{\text{eff}} Y(t) = F_{\text{eff}}(t) \tag{6.12}$$

where

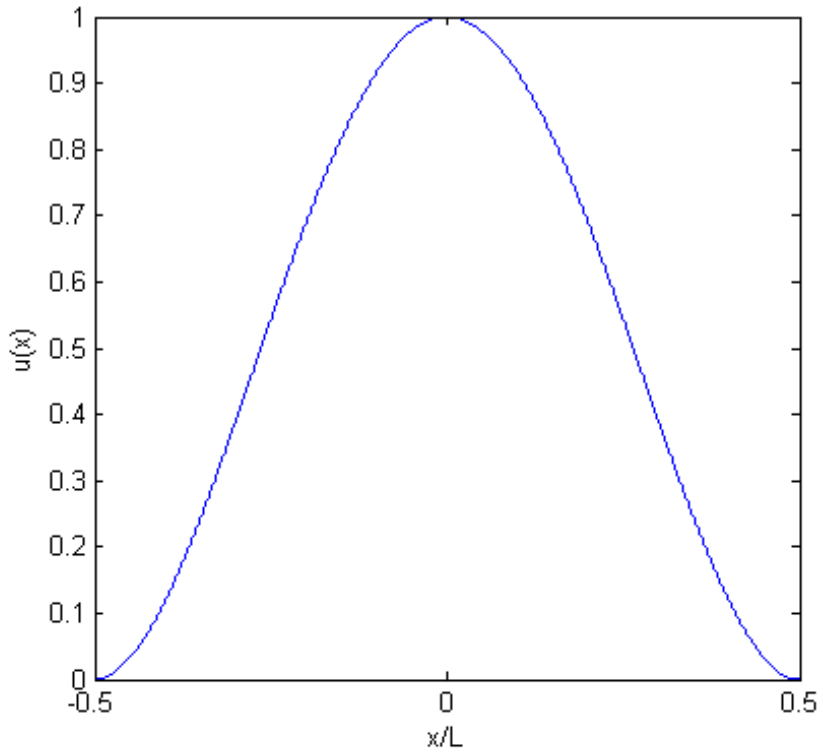

Figure 6.8: Shape of the fundamental mode $u(x)$ of a doubly-clamped cantilever

$$
\begin{aligned}
M_{\text{eff}} =& m \int_{-L/2}^{L/2} u^2(x) dx \\
\Gamma_{\text{eff}} =& \alpha \int_{-L/2}^{L/2} u^2(x) dx \\
k_{\text{eff}} =& EIk^4 \int_{-L/2}^{L/2} u^2(x) dx \\
F_{\text{eff}} =& \int_{-L/2}^{L/2} u(x) f(x,t) dx.
\end{aligned}
\tag{6.13}
$$

For convenience, we list the two numerical integrals for the fundamental mode ($k = 4.730041/L$).

$$
\begin{aligned}
\frac{1}{L} \int_{-L/2}^{L/2} u^2(x) dx &= 0.3965 \\
\frac{1}{L} \int_{-L/2}^{L/2} u(x) dx &= 0.5232
\end{aligned}
\tag{6.14}
$$

We could have multiplied all the above effective parameters by any numerical factor, which would have redefined, for example, the effective mass M_{eff}. Our particular definition of the effective parameters implies that F_{eff} is equivalent to a force f_c applied at the *center* of the beam since

$$
\begin{aligned}
F_{\text{eff}}(t) =& \int u(x) f_c(t) \delta(x) dx \\
=& f_c(t)
\end{aligned}
$$

If we proceed with this definition of F_{eff} to compute force sensitivity, we are computing the sensitivity to a force acting at the center of the beam. From Eq. 2.35, the solution to Eq. 6.12 is

$$
\tilde{Y}(f) = \chi(f) \tilde{F}_{\text{eff}}(f) \tag{6.15}
$$

where

$$
\chi(f) = \frac{1}{k_{\text{eff}}^2 \left(1 - \frac{f^2}{f_c^2} + i \frac{f}{f_c Q}\right)}. \tag{6.16}
$$

$$
f_c = \frac{1}{2\pi} \sqrt{\frac{k_{\text{eff}}}{M_{\text{eff}}}} \tag{6.17}
$$

$$\Gamma = \frac{k_{\text{eff}}}{2\pi f_c Q}. \tag{6.18}$$

For reference purposes, we compute $|\chi|^2$,

$$|\chi(f)|^2 = \frac{1}{k_{\text{eff}}^2 \left((\frac{f^2}{f_c^2} + 1)^2 + \frac{f^2}{f_c^2 Q^2} \right)}. \tag{6.19}$$

6.4 Magnetomotive Actuation and Detection

Magnetomotive actuation and detection is a broadband technique. Unlike capacitive detection, it does not rely on a tuning circuit. The difficulty encountered with a tuning circuit is that the resonance frequency of the cantilever needs to be tuned to that of the circuit, which requires prior knowledge of the cantilever resonance frequency. The magnetomotive measurement scheme avoids this problem altogether as it does not rely on a tuning circuit, and therefore works for a broad range of resonance frequencies. This technique has been demonstrated on cantilevers with resonance frequencies as large as 1 GHz [185]. In a magnetomotive detection scheme (see Figure 6.9) the cantilever is driven by a Lorentz force and detected via an electromotive force. In the following, we will investigate how the on-resonance response of the cantilever to the Lorentz force can be detected as a change in the electrical impedance. The calculation is presented in more detail in Refs. 184 and 186. The Lorentz force per unit length F_L on a cantilever that is placed perpendicular to a uniform magnetic field B is

$$\tilde{F_L}(f) = \tilde{I}(f)B \tag{6.20}$$

where $\tilde{I}(f)$ is the current through the beam. The effective force is therefore

$$\begin{aligned} \tilde{F}_{\text{eff}}(f) &= \int f dx \\ \tilde{F}_{\text{eff}}(f) &= \tilde{I}(f)B \int_{-L/2}^{L/2} u(x) dx. \end{aligned} \tag{6.21}$$

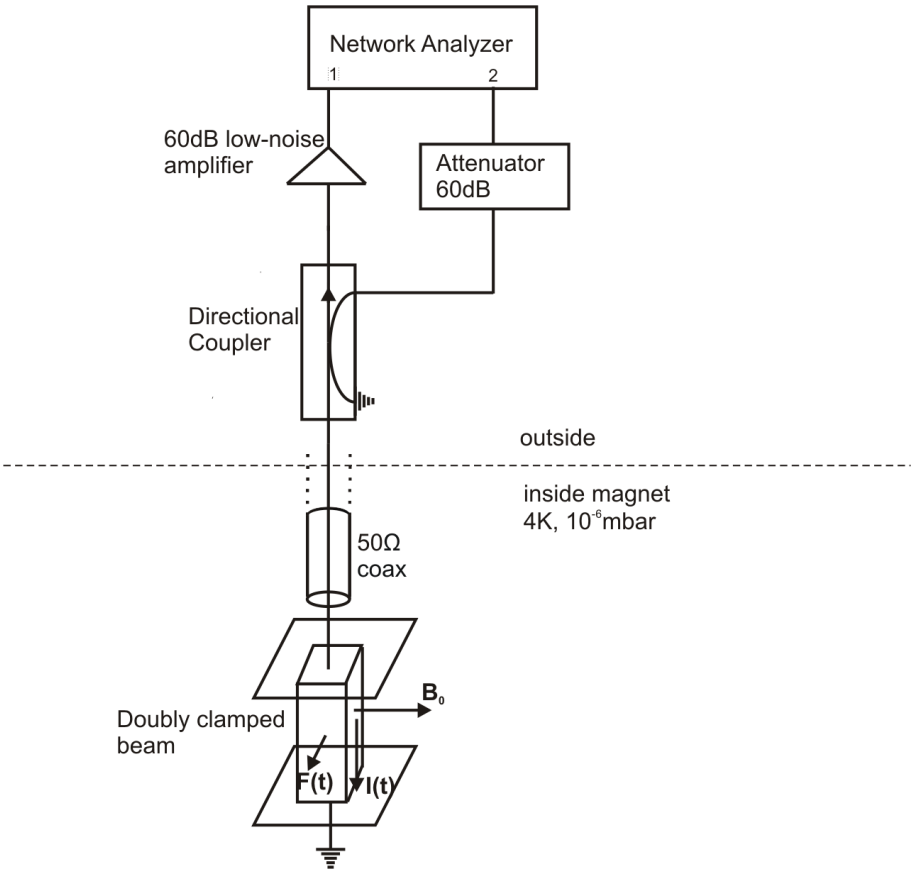

Figure 6.9: A sketch of the experimental setup of the magnetomotive experiments

According to Eq. 6.16, the resulting motion of the cantilever is

$$\tilde{Y}(f) = \frac{\tilde{I}(f)B\int_{-L/2}^{L/2} u(x)dx}{k_{\text{eff}}\left(1 - \frac{f^2}{f_c^2} - \frac{if}{fQ}\right)}. \tag{6.22}$$

By Lentz's law, the motion of the cantilever changes the enclosed magnetic flux and therefore will induce an electromotive force given by

$$\epsilon = -B\int_{-L/2}^{L/2} \frac{\partial y}{\partial t}dx. \tag{6.23}$$

If you are unfamiliar with Lentz's law, you can instead consider the Lorentz force that results from the transverse motion of the cantilever. The result is the same. Moving into

the frequency domain, we have

$$\begin{aligned}\tilde{\epsilon}(f) &= 2\pi i f B \int_{-L/2}^{L/2} \tilde{y}(x,f)dx \\ \tilde{\epsilon}(f) &= 2\pi i B \tilde{Y}(f) \int_{-L/2}^{L/2} u(x)dx.\end{aligned} \tag{6.24}$$

Combining Eq. 6.22 and Eq. 6.24, we get

$$\tilde{\epsilon}(f) = \frac{2\pi i f \tilde{I}(f) B^2}{k_{\text{eff}}\left(1 - \frac{f^2}{f_c^2} - \frac{if}{fQ}\right)} \left[\int_{-L/2}^{L/2} u(x)dx\right]^2. \tag{6.25}$$

Using $k_{\text{eff}} = (2\pi f_c)^2/M_{\text{eff}}$ and writing Eq. 6.25 in terms of the actual mass $M = mL$ rather than the effective mass M_{eff} defined in Eq. 6.13, we get

$$\tilde{\epsilon}(f) = \frac{2\pi i f \tilde{I}(f) B^2}{M f_c^2\left(1 - \frac{f^2}{f_c^2} - \frac{if}{fQ}\right)} \frac{\left[\int_{-L/2}^{L/2} u(x)dx\right]^2}{\int_{-L/2}^{L/2} u^2(x)dx}. \tag{6.26}$$

On resonance ($f = f_c$), the expression reduces to

$$\tilde{f}(f) = \frac{-QB^2}{2\pi f_c M} \frac{\left[\int_{-L/2}^{L/2} u(x)dx\right]^2}{\int_{-L/2}^{L/2} u^2(x)dx}. \tag{6.27}$$

Since the induced voltage is proportional to the applied current, one can define a mechanical resistance R_m,

$$R_m = -\epsilon(\tilde{f})/\tilde{I}(f). \tag{6.28}$$

We see that on-resonance, the electrical resistance increases. The negative sign indicates that the induced electric field opposes the applied current. Using Eq. 6.14 to estimate the integrals for the fundamental mode, we arrive at

$$R_m = 0.6903\frac{QB^2L^2}{2\pi f_c M}. \tag{6.29}$$

For one of our cantilevers, we have

$$\begin{aligned} f_c &= 5.23 \text{ MHz}, \\ B &= 4 \text{ T, and} \\ L &= 10\mu\text{m}. \end{aligned} \tag{6.30}$$

Given that the cantilever has a 10 nm thick Au layer on top of it, with a 2 nm Cr adhesion layer, we estimate the cantilever mass to be $M = 1.2 \times 10^{-15}$ kg. From a rough guess of the quality factor, $Q \approx 10^4$, we estimate the resulting magnetomotive resistance to be

$$R_m = 0.6903 \frac{10^4 (3\text{ T})^2 (15\ \mu\text{m})^2}{(1.46 \times 10^{-15}\text{ kg})(2\pi \times 7.6\text{ MHz})} \approx 300\,\Omega. \tag{6.31}$$

The estimated magnetomotive resistance R_m is comparable to the off-resonance (DC) resistance of 770 Ω, which indicates that the on-resonance change in resistance R_m should be observable. The quantity measured by the network analyzer is a coefficient of reflection r or transmission t, defined by

$$\begin{aligned} r &= \frac{V_r}{V_i} \\ t &= \frac{V_t}{V_i}. \end{aligned} \tag{6.32}$$

Here V_i is the (complex) voltage of the electromagnetic wave traveling into a device, and V_r and V_t are the reflected and transmitted voltages. Phaser notation is used in Eq. 6.32. The currents I_i and I_r of the incoming and reflected waves obey the relations $Z_0 = V_r/I_r = V_i/I_i$ and $Z = (V_i + V_r)/(I_i - I_r)$. Here Z_0 is the characteristic impedance of the electromagnetic waves in the coaxial line to which the oscillator is connected. For laboratory standard coaxials cables $Z_0 = 50\,\Omega$. As a point of interest, we note that Z_0 is of the same order of magnitude as the characteristic impedance of free space of $\approx 377\,\Omega$, which is non-coincidental. From the above relations one can show that reflection coefficient r and impedance Z are related by

$$r = \frac{Z - Z_0}{Z + Z_0}. \tag{6.33}$$

We can see from Eq. 6.33 that the reflection coefficient r is smaller in magnitude the closer the impedance Z is to $50\,\Omega$. Zero reflection ($r = 0$) is achieved only when $Z = 50\,\Omega$. Given that the off- and on-resonance impedances are $770\,\Omega$ and $770\,\Omega + R_m$, we expect more reflection on-resonance because the on-resonance impedance is farther from $50\,\Omega$.

In Figure 6.9 we show a sketch of the experimental setup used to measure the reflection coefficient as a function of frequency. A directional coupler (Mini-Circuits ZDC-10-1) was used to separate the incoming and reflected signals. The function of the directional coupler is similar to that of an optical directional coupler and will not be discussed further here. A 60 dB low-noise amplifier (model MITEQ-AU-1291) was used to amplify the reflected signal, which was then measured in port 1 of a network analyzer (Agilent E5061A). The incoming signal, which was used to drive the cantilever, was generated in port 2. The network analyzer was set to measure the S_{12} parameter, i.e. the reflection coefficient r associated with a signal generated in port 2 and measured in port 1. The magnitude of the drive signal in port 2 was chosen to be as large as possible without overdriving the cantilever. In order to protect the electronics of the network analyzer, an attenuator (Kay 837, -60 dB) was connected to port 2. The attenuator ensured that no matter what signal was generated in port 2, the size of the amplified signal entering port 1 was never enough to damage the electronics of the network analyzer. Grounding wrist straps were worn to avoid electrical damage to the network analyzer. Electrical contact from the external circuitry to the cantilever chip was made with wire bonds (Westbond 7400A Ultrasonic Wire Bonder at the Cornell Nanofabrication Facility). After wirebonding the cantilever was prone to damage due to electrical discharge, which resulted in a loss of conductivity accross the cantilever. In order to prevent such damage, we used grounding wrist straps, wore appropriate clothing (i.e. no wool), and protected the cantilever by encasing it in a metallic box whenever possible. The most important precaution, however, was to establish an electrical short accross the cantilever using a wirebond immediately before wirebonding the cantilever to the external circuitry. This way any excess charge could dissipate accross the wirebond rather than accross the cantilever. This wirebond was only removed at the last possible moment, i.e. immediately before placing the cantilever into in a superconducting magnet, which was held

at $T = 4$ K and $P = 10^{-6}$ mbar. To ensure that the magnet was fully immersed in liquid helium, the helium level in the Dewar containing the magnet must be kept above 5.5 in. The helium filling and refilling protocol is given in Appendix C.1.2. in Ref. 41. Current to the magnet was provided by a four-quadrant power supply (Model 4Q-05100, American Magnetics, Inc., Oak Ridge, Tennessee). The magnet was rated to 6 T and had a field-to-current ratio of 0.1392 TA^{-1}. More detailed information on the magnet, the Dewar, and the operation of the magnet is given in Appendix B of Ref. 119.

In Figure 6.10 we show the observed coeficient of reflection as a function of frequency at $B = 2$ T and $B = 4$ T. A power of -35 dBm was applied to port 2 of the network analyzer, just small enough to avoid non-linear effects, such as an asymmetric shape of the resonance curve or a small shift in the cantilever resonance frequency, both of which are features of an overdriven cantilever. As shown in Figure 6.10 the reflected signal increases on resonance, consistent with the discussion surrounding Eq. 6.33. At larger magnetic fields, a larger on-resonance change in the reflected signal was observed, as predicted by Eq. 6.29.

In principle, one can use an arbitrarily large magnetic field B in order to increase the on-resonance resistance R_m in Eq. 6.29. However, it turns out that an increased magnetic field leads to additional friction and so decreases the cantilever quality factor Q, as can be seen from Figure 6.10. The source of the increased friction is thermally induced current noise, or Johnson noise, given by

$$P_{\delta I} = \frac{4k_B T}{R}, \tag{6.34}$$

where R is the resistance of the cantilever. If the cantilever is placed in a magnetic field, these current fluctuations $\delta I(t)$ result in force fluctuations $\delta F(t)$, which by Lorentz's force

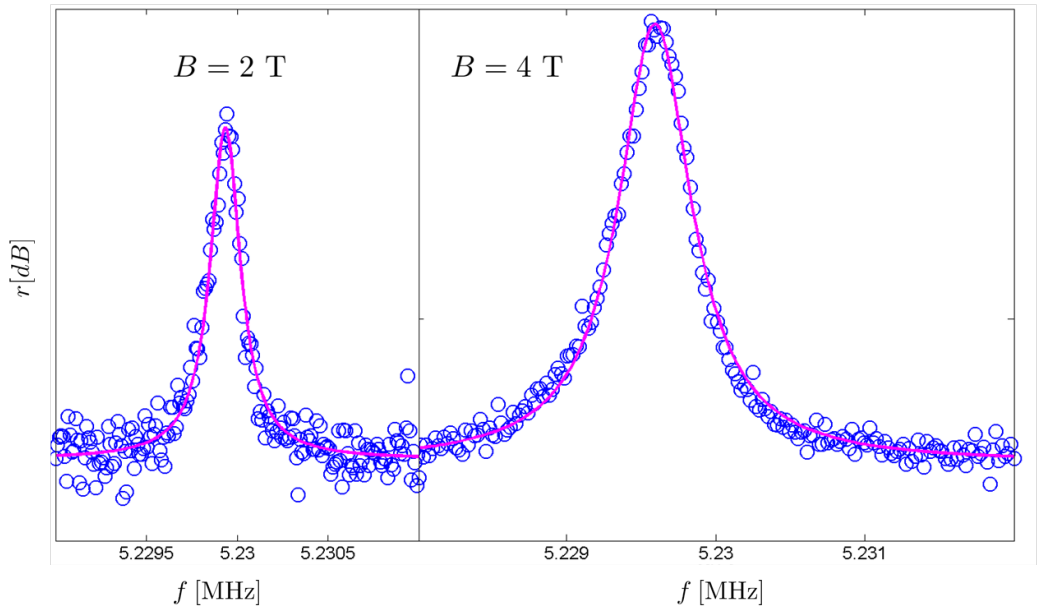

Figure 6.10: Observed magnitude of the reflection coefficient $|r|$ (e.g. the S_{12} parameter) as a function of frequency at $B = 2$ T and at $B = 4$ T. Each data point represents an average of 50 measurements, each taken in a 100 Hz bandwidth. The solid line is a fit to the response function of a harmonic oscillator (see Eq. 6.19), from which we extract quality factors of $Q = 26 \times 10^3$ and $Q = 8.8 \times 10^3$ at $B = 2$ T and at $B = 4$ T, respectively. We see that a larger magnetic field results in a larger signal, but also in a smaller quality factor. The cantilever was held inside a superconducting magnet at a pressure and temperature of $p = 2 \times 10^{-7}$ mbar and $T = 4$ K, respectively. The power applied to port 2 of the network analyzer (-35 dBm) was chosen to maximize the signal without overdriving the cantilever.

are given by

$$\delta F(t) = LB\delta I(t). \tag{6.35}$$

Taking the power spectrum of Eq. 6.35, we have

$$P_{\delta F}(f) = L^2 B^2 P_{\delta I}(f). \tag{6.36}$$

A figure of merit that describes the force sensitivity of the cantilever is the friction Γ [41]. By the fluctuation-dissipation theorem, the force fluctuations $P_{\delta F}(f)$ at the cantilever resonance frequency $f = f_{\text{res}}$ are linked to an increase in friction $\Delta\Gamma$, i.e.

$$\Gamma = \Gamma_0 + \Delta\Gamma \tag{6.37}$$

where

$$\Delta\Gamma = \frac{P_{\delta F}(f_c)}{4k_B T}. \tag{6.38}$$

Γ and Γ_0 are the total and the intrinsic cantilever friction, respectively. Combining Eq. 6.34, Eq. 6.36, Eq. 6.37, and Eq. 6.38, we arrive at an expression for the cantilever friction Γ,

$$\Gamma = \Gamma_0 + \frac{L^2 B^2}{R}. \tag{6.39}$$

We see that Γ increases quadratically with magnetic field. In order to compare with experiment, we express Γ in terms of the experimentally observable quality factor Q using $\Gamma = \frac{k_c}{2\pi f_c Q}$ and $k_c = (2\pi f_c)^2 M$,

$$Q^{-1} = Q_0^{-1} + \frac{L^2 B^2}{2\pi f_c M R}. \tag{6.40}$$

where Q_0 is the intrinsic, or zero-field, quality factor. In Figure 6.11 we indeed observe a quadratic dependence of the observed inverse quality factor Q^{-1} on magnetic field thus confirming the validity of Eq. 6.40. The slope of the data in Figure 6.11 agrees within a

factor of order one with the prediction from Eq. 6.40. Any deviation between the predicted and observed values is most likely due to the uncertainty in determining the cantilever mass. Using the fitted zero-field quality factor of $Q_0 = (8.0 \pm 0.8) \times 10^4$ and the parameters listed in the caption of Figure 6.11, we estimate the zero-field cantilever friction to be

$$\Gamma_0 = 0.5 \times 10^{-12} \text{kg s}^{-1}. \tag{6.41}$$

We note that the preceding analysis assumed that the forces are applied uniformly across the cantilever. Therefore the friction coefficient is the one associated with sensing a uniform force. If we were instead interested in sensing a force acting on the center of the beam, we would have to use the effective mass $M_{\text{eff}} = 0.3965M$ in place of M. The corresponding friction coefficient would be lowered by a factor of 0.3965.

We conclude that Johnson noise significantly decreases the quality factor and increases friction in a typical magnetomotive experiment, and thus places a significant limitation on the sensitivity of magnetomotive detection. The effect can be ameliorated by switching to a lower applied field B. However, at small magnetic fields, the signal R_m (see Eq. 6.29) is small, which places restrictions on the sensitivity of the instrumentation. Choosing an optimal value for the magnetic field is therefore a trade-off between minimizing cantilever friction and minimizing instrument noise.

6.5 Capacitive Actuation and Detection

A capacitive technique exists to simultaneously drive and detect nanomechanical cantilevers [187]. The cantilever is driven by means of an electrostatic force of attraction between the cantilever and a nearby electrode. Since the motion of the cantilever modulates the capacitance to the electrode, the cantilever oscillation can be detected as a change in the electrical impedance.

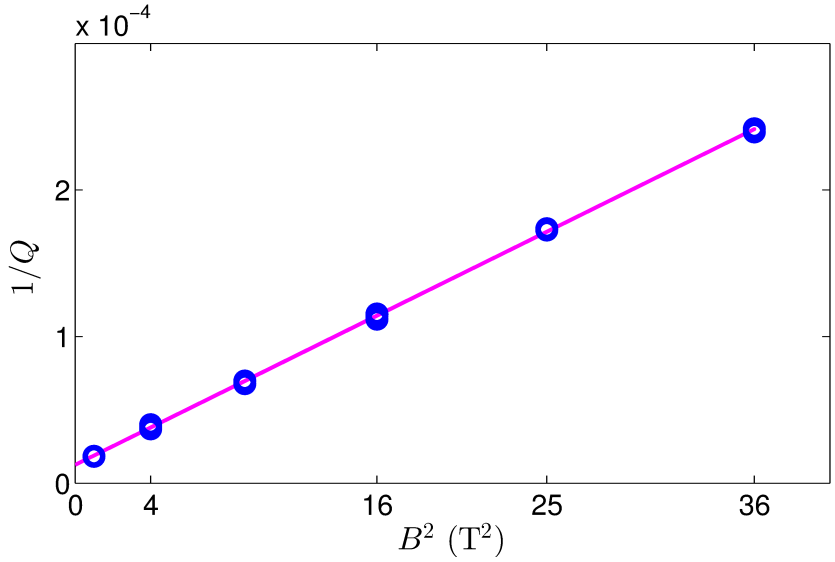

Figure 6.11: The inverse of the quality factor, Q^{-1}, as a function of the applied magnetic field. The quality factor Q at a given magnetic field was determined by fitting the reflection coefficient versus frequency curve, such as the one shown in Figure 6.10, to the response function of a harmonic oscillator (see Eq. 6.19). The solid line is a linear regression of the data and has a slope of $(6.36 \pm 0.07) \times 10^{-6}$ T^{-2}, reasonably close to to the value of 3.3×10^{-6} T^{-2} predicted from Eq. 6.40. The disagreement between the observed and predicted slope is most likely due to the uncertainty in the cantilever mass, which depends critically on cantilever dimensions. The fitted value of the zero-field quality factor is $Q_0 = (8.0 \pm 0.8) \times 10^4$. Parameters: $L = 10$ μm, $R_m = 770$ Ω, $f_c = 5.23$ MHz, and $M = 1.2 \times 10^{-15}$ kg.

A tuning circuit is typically used to increase the motion-induced change in the electrical reflection coefficient, thereby increasing the sensitivity of this technique. Capacitive actuation has been demonstrated at frequencies as high as 700 MHz [188]. Since we have not yet finished fabricating singly-clamped cantilevers for capacitive detection, we will focus on the theoretical aspects of capacitive detection. The experimental setup of the capacitive measurement scheme is described in detail in Ref. 181 and will not be discussed further here. To compute the electrical response of capacitively actuated and detected cantilever, we will consider a measurement scheme where both an AC and DC voltage is applied between the cantilever and a nearby electrode [181]. We will assume that the DC bias voltage V_g is much smaller than the AC voltage V_s between the electrode and the cantilever. The energy stored in the electric field between cantilever and the electrode is given by

$$W(t) = \frac{1}{2}C(x(t))(V_g + V_s(t))^2 \tag{6.42}$$

where $C(x)$ is the cantilever-electrode capacitance and x is the deflection of the cantilever at its midpoint. A force $F(t)$ results on the cantilever because this energy is distance dependent,

$$F(t) = -\frac{1}{2}\frac{dC(x)}{dx}(V_g + V_s(t))^2. \tag{6.43}$$

Assuming $V_g >> V_s$, this force can be approximated as

$$F(t) = -\frac{dC(x)}{dx}V_g V_s(t) + F_0 \tag{6.44}$$

where F_0 is a constant independent of time. If the cantilever is driven on-resonance, i.e.

$$V_s(t) = V_s e^{2\pi i f_c t} \tag{6.45}$$

then the cantilever displacement $x(t)$ is by Eq. 2.36 given by

$$x(t) = -\frac{iQF(t)}{k} \tag{6.46}$$

where k_c is the cantilever spring constant and Q the quality factor. Substituting Eq. 6.44 for the force, we obtain

$$x(t) = iQ\frac{1}{k_c}\frac{dC(x)}{dx}V_g V_s e^{2\pi i f_c t} + x_0. \tag{6.47}$$

where x_0 is the mean cantilever displacement. Taking a time derivative, we have

$$\frac{dx}{dt} = -2\pi f Q\frac{1}{k_c}\frac{dC(x)}{dx}V_g V_s e^{2\pi i f_c t}. \tag{6.48}$$

Next, we investigate how cantilever motion affects the impedance of the circuit. The charge on the electrodes is coupled to the cantilever displacement $x(t)$ through the capacitance $C(x)$,

$$Q(t) = C(x(t))(V_g + V_s(t)). \tag{6.49}$$

Taking a time derivative and assuming that $V_g >> V_s$, we get

$$I(t) = \frac{dC}{dx}\frac{dx}{dt}V_g + 2\pi i f_c C(x)V_s(t). \tag{6.50}$$

In the absence of an applied gate voltage ($V_g = 0$), only the second term survives. In this case current is only weakly position dependent. A finite gate voltage gives rise to the first term in Eq. 6.50, which is quadratic in V_g because $x(t)$ itself contains another factor of V_g (see Eq. 6.47). For large gate voltages the first term in Eq. 6.50 dominates. Assuming that the displacement of the cantilever motion x is small compared to the electrode-cantilever separation d, we can approximate

$$\frac{dC}{dx} \approx -\frac{C}{d}. \tag{6.51}$$

Applying Eq. 6.48 and Eq. 6.51 to Eq. 6.50, we get

$$I(t) = Z_m V_s(t), \tag{6.52}$$

where Z_m is an effective on-resonance impedance given by

$$Z_m(f_c)^{-1} = \frac{2\pi f Q (V_g C)^2}{d^2 k} + 2\pi i f_c C. \tag{6.53}$$

The first term in the above equation results from cantilever displacements and so disappears away from resonance. The second term is the impedance due to the capacitance between the cantilever and the electrodes and does not depend on the cantilever displacement. To describe the behavior of the circuit at all frequencies (i.e. away from resonance as well), we assume that the cantilever's response function is that of a harmonic oscillator with quality factor Q (see Eq. 6.19). Using $k_c = 2\pi f_c^2 M$, the frequency dependence of the effective impedance can be written as

$$Z_m^{-1} = \left(R_m + 2\pi i L + \frac{1}{2\pi i f C} \right)^{-1} + 2\pi i f_c C \tag{6.54}$$

where

$$\begin{aligned} R_m &= \frac{2\pi f_c M d^2}{Q C^2 V_g^2} \\ L_m &= \frac{RQ}{2\pi f_c} \\ C_m &= \frac{1}{2\pi f_c RQ}. \end{aligned} \tag{6.55}$$

On resonance, the effects of the inductor and capacitor cancel, and a large amount of current can leak through R_m, giving rise to a surge in current. For reasonable parameters, $L = 10\ \mu$m, $f_c = 10^6\ \text{s}^{-1}$, $M = 10^{-15}$ kg, $k = M(2\pi f_c)^2$, $Q_0 = 10^5$, $V_G = 10$ V, $C = 10^{-18}$ F, and $d = 100$ nm, we estimate

$$R_m = 30\ \text{k}\Omega. \tag{6.56}$$

Usually, a tuning or tank circuit is used to reduce the on-resonance impedance towards 50 Ω, which makes the change in resistance easier to detect with standard 50Ω impedance matched electronics. A picture of the cantilever chip and tuning circuit is shown in Figure 6.12. The

Figure 6.12: A photograph of a cantilever die and an LC-tank circuit. The cantilever die contains doubly-clamped cantilevers with adjacent electrodes. Electrical contact from the chip to the chip holder is made through wire bonding. The chip holder was obtained from Jerry Drumeheller at the Cornell Nanofabrication Facility. While the capacitive detection scheme has not yet been implemented in the Marohn group, a similar setup (without the LC tank circuit) was used successfully for the magnetomotive detection scheme.

resonance frequency of the tuning circuit is set to the resonance frequency of the cantilever using an adjustable capacitor. More detail on the capacitive measurement technique, which has not yet been implemeneted in the Marohn lab, can be found in Ref. 181.

Appendix A

The Fourier Transform of the Electrostatic Potential of a Point Charge

Here we summarize a calculation by Roger F. Loring and John A. Marohn of the Fourier transform of the potential $\phi(x, y, z)$ of a point charge located at the origin. The Fourier transform of $\phi(x, y, z)$ is taken in x and in y only, and can be written as

$$\tilde{\phi}_q(k_x, k_y, z) = \int dx\, dy\, e^{i2\pi k_x x} e^{i2\pi k_y y} \frac{q}{4\pi\epsilon_0 \sqrt{x^2 + y^2 + z^2}}. \tag{A.1}$$

Because the integrand is even in x and in y, the expression simplifies to

$$\tilde{\phi}_q(k_x, k_y, z) = \frac{q}{4\pi\epsilon_0} \int dx\, dy\, \frac{\cos(2\pi k_x x)\cos(2\pi k_y y)}{\sqrt{x^2 + y^2 + z^2}}. \tag{A.2}$$

In polar coordinates, $x = \rho\cos\phi$ and $y = \rho\sin\phi$, so that

$$\tilde{\phi}_q(k_x, k_y, z) = \frac{q}{4\pi\epsilon_0} \int_0^{2\pi} d\phi \int_0^{\infty} \rho d\rho \frac{\cos(2\pi k_x \rho\cos\phi)\cos(2\pi k_y \rho\sin\phi)}{\sqrt{\rho^2 + z^2}}. \tag{A.3}$$

To perform this integral, we first combine the two cosines by a trig identity, and then use a Bessel function to expand a cosine of a cosine. Using a trig identity, the numerator becomes

$$\begin{aligned} \chi &= \frac{1}{2}\cos\left(2\pi\rho k_x \cos\phi + 2\pi\rho k_y \sin\phi\right) + \frac{1}{2}\cos\left(2\pi\rho k_x \cos\phi - 2\pi\rho k_y \sin\phi\right) \\ \chi &= \frac{1}{2}\cos\left(2\pi\rho k\cos(\phi - \theta)\right) + \frac{1}{2}\cos\left(2\pi\rho k\cos(\phi + \theta)\right) \end{aligned} \tag{A.4}$$

where we used $k_x = k\cos\theta$ and $k_y = k\sin\theta$. Using a Bessel function to expand the cosine, we get

$$\begin{aligned} \chi = \frac{1}{2}J_0(2\pi\rho k) &+ 2\sum_{n=2,4,\ldots}^{\infty} J_n(2\pi\rho k)\cos(n(\phi - \theta)) \\ &+ 2\sum_{n=2,4,\ldots}^{\infty} J_n(2\pi\phi\rho k)\cos(n(\phi + \theta)) \end{aligned} \tag{A.5}$$

$$\chi = \frac{1}{2} J_0(2\pi\rho k) + 2 \sum_{n=2,4,\ldots}^{\infty} J_n(2\pi\rho k)\cos(n\phi)\cos(n\theta). \tag{A.6}$$

All the terms for which $n \neq 0$ vanish upon integrating over ϕ. Integration over the remaining term is trivial. The result is

$$\tilde{\phi}_q(k_x, k_y, z) = \frac{q}{4\pi\epsilon_0} \int_0^{\infty} \rho d\rho \frac{J_0(2\pi\rho k)}{\sqrt{\rho^2 + z^2}}. \tag{A.7}$$

Integrating over ρ we finally arrive at our final expression for the Fourier transform of the electric potential of a point charge,

$$\tilde{\phi}_q(k_x, k_y, z) = \frac{q}{4\pi\epsilon_0 k} e^{-2\pi k z}. \tag{A.8}$$

We note that Eq. A.8 can be used to compute the Fourier transforms of higher order poles, i.e. dipoles or quadrupoles. For instance, to calculate the Fourier transform of the potential ϕ_{dip} due to a dipole $\mathbf{p}$ located at the origin, we make use of the relation

$$\phi_{\text{dip}}(\mathbf{r}) = \frac{\mathbf{p}}{q} \cdot \nabla \phi_q(\mathbf{r}). \tag{A.9}$$

It's easy to verify that the above expression is equivalent to the usual expression for a dipole potential. Taking a Fourier transform of Eq. A.9, we have

$$\tilde{\phi}_{\text{dip}}(k_x, k_y, z) = \frac{p_x 2\pi k_x + p_y 2\pi k_y + p_z \partial_z}{q} \tilde{\phi}_q(k_x, k_y, z), \tag{A.10}$$

which using Eq. A.8 simplifies to

$$\tilde{\phi}_{\text{dip}}(k_x, k_y, z) = \frac{p_x k_x + p_y k_y - p_z k}{2\epsilon_0 k} e^{-2\pi k z}. \tag{A.11}$$

It is also easy to compute electric fields and field gradients. For example, the Fourier transform of the electric field of a point charge $\mathbf{E}_q(\mathbf{r}) = -\nabla\phi_q(\mathbf{r})$ is given by

$$\tilde{\mathbf{E}}_q(k_x, k_y, z) = -2\pi(k_x, k_y, -k)\tilde{\phi}_q(k_x, k_y, z). \tag{A.12}$$

From Eq. A.8 we then have

$$\tilde{\mathbf{E}}_q(2\pi k_x r, 2\pi k_y, z) = \frac{(-k_x, -k_y, k)q}{2\epsilon_0 k} e^{-2\pi k z}. \tag{A.13}$$

Appendix B

Nanofabrication Recipes

B.1 Fabricating Transistor Substrates

Grow 300 nm of oxide onto n-type silicon wafers.

The MOS clean and furnace processing is usually done with a batch of 25 wafers. All other processes are performed on three wafers, which is the maximum that will fit in the evaporator chamber. It is crucial that the wafers for the transistor substrates are n-type because the dopants in p-type wafers react with fluorine in the Oxford etcher. N-type wafers can easily be recognized as they have the main flat opposite (not at 90 degrees of) the smaller flat.

- MOS clean, HF dip is not necessary. Start programming the furnace oven when wafers are in base bath rinse, Coral into oxide furnace when half-way through acid rinse cycle. Reserve 2 h on Coral. Process takes 1h 35 min from the time the torch light OK passes until the furnace is unloaded.
- Oxide furnace: 315 nm of thermal SiO, recipe 6 (wet oxide, no HCl), no buffer/spacer wafers necessary

  Cycle 5: 10 min ramp, 1000 C (reduced from 1200 C)

  Cycle 8: 50 min

  Cycle ?(varies): 10 min ramp, P 900 C
- Measure oxide thickness with F50 (filmetrics)

Etch windows through the oxide

- Spin resist: 3000 rpm, 30 s

  IPA/acetone

  P20, wait 10 s

  SPR 955 CM 2.1

  Bake 90 s, 90 C

- Autostep: mask: GATE PADS, EXEC FET\GATE, exposure = 0.6 s, 1st level
- Postexposure bake: 90 s, 115 C
- Develop: HEX 1206, recipe 3 or HMP recipe 2 (726 MIF, 120 s, DP), inspect wafer by eye
- Ox80: oxide etch CHF_3/O_2, 20 min, then CF_4 2 min (CF_4 removes both Si and SiO near Si-SiO interface). After the etch check if gate squares are grey like Si. Optionally you can also check for conductivity between the gates using a multimeter.

Pattern the source and drain electrodes

- Remove resist with acetone/IPA, sonicate in acetone/IPA for 5 min, remove from bath while rinsing with acetone, then IPA, N_2 blow dry
- Spin resist: 3000 rpm, 30 s

  acetone/IPA

  P20, wait 10 s

  nLOF 2020

Bake 60 s, 115 C

- Spend 10 min or so inspecting the mask (= 5um FET) under an optical microscope to check for dust, handle mask with clean gloves, blow with N_2 gun by the autostep prior using it
- Autostep:mask: 5um FET, EXEC FET\FET, exposure = 0.11 s, 1st level (no alignment necessary since the tolerances are huge, i.e. 0.5 mm)
- PEB: 60 s, 115 C (same as prebake)
- Develop: 726 MIF 120 s DP (recipe 2 on HMP). Inspect wafer under an optical microscope making sure that there are no specks that will short the source and drain electrodes.
- Glen 1000, recipe 3 (100 W, 45 s), RIE mode (tray b!!!)
- Evaporate: 5 nm Cr, 30 nm Au
- Liftoff: fluid 1165, 8 h or more
- Remove from liftoff: sonicate for 5 min, remove while rinsing with DI H_2O, N_2 blow dry
- Spin resist: acetone/IPA, 3000 rpm, 30 s. The resist protects the wafer from the dicing saw

  P20, wait 10 s

  SPR 955 CM 2.1

  Bake 90 s, 90 C

- Dicing saw: put wafer's on transparent UV tape (wafers facing down, then place tape over metal ring and waver, $\Delta x = \Delta y = 16$ mm, adjust depth such that you leave 50 μm of material, use 1 min of UV light to remove the tape.)

B.2 Fabricating Split Gate Transistors

Pattern the intedigitated gate electrodes

- Spin resist onto fused silica wafers: 3000 rpm, 30 s

  acetone/IPA

  P20, wait 10 s

  nLOF 2020

  Bake 60 s, 115 C

- Autostep: mask = SPLITGATE, EXEC SPLITGATE\GATE, exposure = 0.16 s, manual loading, no allignment

- PEB: 90 s, 115 C

- Develop: HEX 1206, recipe 3 or HMP recipe 2 (726 MIF, 120 s, DP), inspect wafer by eye

- Glen 1000, recipe 3 (100 W, 45 s), RIE mode (tray b!!!)

- Evaporation: 3 nm Cr, 12 nm Pt

- Liftoff: fluid 1165, 8 h or more

- Remove from liftoff: sonicate for 5min, remove while rinsing with DI H_2O, the N_2 dry. Check with a multimeter for shorted gates.

Define the insulating layer along with etch windows to the underlying gate electrodes

- GSI recipe 4 (undoped oxide), N1.46, 67 s (gives 200 nm oxide), 400 C
- Spin resist: 3000 rpm, 30 s

  acetone/IPA

  P20, wait 10 s

  SPR 955 CM 2.1

  Bake 90 s, 90 C
- Autostep: mask = GATE PADS, EXEC SPLITGATE\PADS, exposure = 0.6 s, manual loading, do alignment
- PEB: 90 s, 115 C
- Develop: HEX 1206 recipe 3 or HMP recipe 2 (726 MIF, 120 s, DP), inspect wafer by eye
- Ox 80: Oxygen clean without wafer, 5 min (optional), CHF_3/O_2, oxide etch, 15 min (tool specifications: 38 nm/min). Use a multimeter to ensure that the etch completed all they way to the gate contacts.
- Remove resist with acetone/IPA, sonication in acetone/IPA for 5 min, remove with rinsing with acetone, then IPA, then N_2 blow dry

Define the source and drain electrodes

- Spin resist: 3000 rpm, 30 s

acetone/IPA

P20, wait 10 s

nLOF 2020

Bake 60 s, 115 C

- Autostep: MAP SPLITGATE\FET, exposure = 0.11 s, mask: FET, spend at least 10 min inspecting mask under a microscope to check for dust, handle mask with clean gloves, blow with N_2 before using it, use manual loading, do alignment
- PEB: 60 s, 115 C
- Develop: 726 MIF 120 s, DP (recipe 2 on HMP), inspect wafer with microscope making sure that there are no specks that will short source to drain
- Glen 1000, recipe 3 (100 W, 45 s), RIE mode (tray b!!!)
- Evaporation: 3 nm Cr, 17 nm Au
- Liftoff: fluid 1165, 8 h or more
- Remove from liftoff: sonicate for 5 min, remove while rinsing with DI H_2O, the N_2 dry
- Dicing saw: put wafer's on blue tape (wafers facing down, then place tape over metal ring and waver, $\Delta x = \Delta y = 15.875$ mm, set depth such that you cut all the way through

B.3 Fabricating Singly-Clamped Cantilevers for Capacitive Detection

Grow oxide and deposit nitride onto silicon wafers

- MOS clean a set of *double-sided polished* silicon wafers (25 or 30 wafers). HF dip is not necessary. Start programming oven when in base bath rinse. Coral into oxide furnace when half-way through acid rinse cycle.
- Oxide furnace: grow 600 nm of thermal SiO, recipe 6 (wet oxide, no HCl)

  Cycle 5: 10 min ramp, 1000 C

  Cycle 8: 130 min

  Cycle ?(varies): 10 min ramp, P 850 C
- Measure oxide thickness of a single wafer with the filmetrics F50. Note: This step will contaminate the wafer and it will no longer be MOS cleaned.
- Nitride furnace: 340 nm of thermal LS SiN, recipe 3

  Cycle 8: 12 min pumpdown

  Cycle 14: 100 min deposition time

Layer 1: Define cantilevers by Ebeam lithography

- Acetone/IPA clean in spinner
- 4% PMMA, 495 K in anisole, 60 s, 4000 rpm, bake 15 min, 170 C
- 2% PMMA, 950K in MIBK, 60 s, 2000 rpm, bake 15 min, 170 C

- Jeol: hoepker_n/090604/mixed.mgn (need to change this file)
- Develop: MIBK:IPA, 1:3, 75 s, wash with IPA, dry with N2
- Glenn 1000, recipe 3 (100 W, 45 s, RIE mode, tray b)
- Evaporation: Cr 5 nm, Au 35 nm, Cr 10 nm, Al 20 nm
- Liftoff: Methylene-Cl + Acetone, 1:1 in sealed containers for 8 h or more
- Pull out of liftoff: sonicate 5 min, wash with acetone+IPA, dry with N2

Layer 2: Etch through nitride to define cantilever block and cantilever by photolithography

- Spin antireflective coating and resist

  Acetone/IPA clean, 30 s, 4000 rpm

  XHRi-16, 30 s, 4000 rpm, bake 60 s, 180 C. The XHRi-16 protects the Al electron beam features from the developer and the BOE.

  SPR 955 CM 2.1, 3000 rpm, 30 s (the resulting resist is 2 μm thick)

  bake 90 s, 90 C

- Autostep: exposure = 0.6 s (double check exposure), focus = -4, mask = RF FRONT, MAP RF\FRONT, do alignment
- Postexp bake: 115 C, 90 s
- Develop: 300 MIF developer, 150 s

- Ox 81etcher

  O_2 clean, 1 min 40 s to remove XHRi-16

  Nitride etch CHF_3/O_2, 8 min (2 μm resist and 20 nm Al features are the etch masks)

  O_2 clean, 3 min to remove fluoropolymers from nitride etch

- Rinse with acetone to remove resist, then sonicate in acetone for 5 min, rinse with IPA, N_2 dry

- O_2 clean, 1 min 40 s to remove remaining XHRi-16

- Al etch, 3 min to remove Al

- Cr etch, 1 min to remove Cr

Layer 3: Define the electrical contact pads by photolithography

- Sping resist, 30 s, 3000 rpm

  Acetone/IPA

  P20, wait 10 s

  nLOF 2020, 30 s, 3000 rpm, bake 60 s, 110 C (resulting in 2 μm thick resist)

- Autostep: exposure = 0.11 s, focus = -4, mask = RF PADS, MAP RF\PADS, do alignment

- Postexposure bake: 60 s, 110 C

- Develop: 300 MIF for 120 s in beaker (may need to develop longer, watch wafer as it is developing), wash with DI H_2O, dry with N2

- Evaporate: Cr 5 nm, Au 100 nm
- Liftoff: fluid 1165, 8 h or more
- Pull out of liftoff: wash with DI H_2O, dry with N2

Release cantilevers

- Deposit SiO: 2 μm on front and 1.6 μm on backside of wafer Use IPA rather than GSI since wafer has metal on it.

  frontside: process 1B for 40 min, clean for 50 min

  backside: process 1B for 25 min, 35 min clean, process 1B for 25min, 35 min clean
- Backside resist: use Jonilyns backside recipe OR

  P20, wait 10 s, 3000 rpm, 30 s

  SPR 220-7.0, ramp from 500 2500 rpm over 30 s

  bake 90 s, 115 C, air cool
- EV620: backside exposure, mask = backside Showey, 25 s (not 12 s!), no PEB, do alignment with crosshair method, position = nch28_audio, load wafer with resist side up!
- Develop: 300 MIF, 5 min (recipe 2 followed by recipe 6 in HMP)
- bake in oven at 90 C for 1 day or more
- P10: confirm resist thickness, should be > 11.5 μm
- Ox81: CHF3/O_2 oxide etch on backside to expose underlying Si, 55 min + 15 min + 20 min

- Unaxis 770, backside dry etch, 470 loops with 1Thru process. Do 200 loops at a time and measure Si etched by profilometry. Stop when there's less than 100 μm of Si left, then remove resist with acetone and IPA and attach a handler wafer using small amounts of CoolGrease on opposite sides of the wafer. Use 0-Trench process until Si is removed. Finding the right stopping point is an art. Dont etch too far!

- Release cantilevers: BOE 6:1, 15 min (may be too long) in teflon boat. Rinse in 3 separate baths of DI H_2O, then 3 baths of IPA before transferring to the critical point dryer. Note: It may be possible to perform the cantilever release using a dry oxide etch process instead.

B.4 Doubly-Clamped Cantilevers for Magnetomotive Detection

Grow oxide and deposit nitride onto regular silicon wafers

- MOS clean a set of *double-sided polished* silicon wafers, HF dip is not necessary, start programming oven when in base bath rinse, coral into oxide furnace when half-way through acid rinse cycle

- Oxide furnace: 600 nm of thermal SiO, recipe 6 (wet oxide, no HCl)

  Cycle 5: 10 min ramp, 1000 C

  Cycle 8: 130 min

  Cycle ?(varies): 10 min ramp, P 850 C

- Measure oxide thickness of a single wafer with the filmetrics F50 (note: this step will contaminate the wafer and it will no longer be MOS cleaned)

- Nitride furnace: deposit 340 nm of thermal low-stress SiN, recipe 3

  Cycle 8: 12 min pumpdown

  Cycle 14: 100 min deposition time

Layer 1: Define cantilevers and tunnel junctions by electron beam lithography

- Acetone/IPA clean in spinner
- 4% PMMA, 495 K in anisole, 60 s, 4000 rpm, bake 15 min, 170 C
- 2% PMMA, 950 K in MIBK, 60 s, 2000 rpm, bake 15 min, 170 C
- Jeol: hoepker_n/081119/mixed.mgn (need to change this file)
- Develop: MIBK:IPA, 1:3, 75 s, wash with IPA, dry with N2
- Glenn 1000, recipe 3 (100 W, 45 s, RIE mode, tray b)
- Evaporation: Cr 5 nm, Au 35 nm, Cr 10 nm, Al 20 nm
- Liftoff: Methylene-Cl + Acetone, 1:1 by eye in sealed containers for 8 h or more
- Pull out of liftoff: sonicate 5 min, wash with acetone and IPA, dry with N2
- Inspect wafers under an optical microscope

Layer 2: Define electrical contacts to Ebeam features by photolithography

- Spin antireflective coating plus resist

  Rinse with acetone/IPA, 30 s, 4000 rpm

  XHRi-16, 30 s, 4000 rpm, bake 60 s, 180 C

nLOF 2020, 30 s, 3000 rpm, bake 60 s at 115 C

- Autostep: focus = -4, exposure = 0.11 s, MAP TUNN\WIRE, do alignment
- Postexposure bake: 115 C, 60 s
- Development: 300 MIF, 120 s
- Inspect wafer under an optical microscpe
- Ox81: O_2 clean, 1 min 40 s to remove XHRi-16 layer
- Evaporation: 5 nm Cr, 100 nm Au, 10 nm Cr, 20 nm Al
- Liftoff: fluid 1165, 8 h or more
- Pull out of liftoff: wash with DI H_2O, dry with N2
- Ox81: O_2 clean, 1 min 40 s to remove remaining XHRi-16
- Ox81: nitride etch CHF_3/O_2, 8 min, (Al is the etch mask)
- Ox81: O_2 clean, 3 min to remove fluoropolymers
- SEM the cantilevers

Release Cantilevers

- Cleave wafer into chips using a diamond scribe
- BOE 6:1 etch for 7 min, then rinse in DI H_2O, dry with N2
- Measure resistance across cantilevers using a multimeter
- SEM the cantilevers

BIBLIOGRAPHY

[1] N. Hoepker, S. Lekkala, R. F. Loring, and J. A. Marohn, Quantifying dielectric fluctuations over polymer films using an atomic force microscope, J. Phys. Chem. B **115**, 14493 (2011). (document), 2.1, 2.4.2, 3.1, 3.2, 3.3, 3.5, 3.6, 3.7, 3.8, 3.9, 3.10, 3.11, 4.2.2, 5.2.3, 5.2.4, 6.1

[2] S. Lekkala, N. Hoepker, J. A. Marohn, and R. F. Loring, Charge carrier dynamics and interactions in electric force microscopy, J. Chem. Phys. **137**, 124701 (2012). (document), 5.1, 5.2, 5.3, 5.7, 5.8, 5.9, 5.2.3, 5.2.3, 5.2.3, 5.2.3

[3] J. L. Luria, N. Hoepker, R. Bruce, A. R. Jacobs, C. Groves, and J. A. Marohn, Spectroscopic imaging of photopotentials and photoinduced potential fluctuations in a bulk heterojunction solar cell film, ACS Nano (2012), DOI: 10.1021/nn300941f. (document), 4.1, 4.1, 4.2.1, 4.2, 4.3, 4.4, 4.2.2, 4.5, 4.6, 4.7, 4.8, 4.9

[4] G. Binnig, C. F. Quate, and C. Gerber, Atomic force microscope, Phys. Rev. Lett. **56**, 930 (1986). 1, 3.1

[5] Y. Martin, C. C. Williams, and H. K. Wickramasinghe, Atomic force microscope force mapping and profiling on a sub-å scale, J. Appl. Phys. **61**, 4723 (1987). 1, 3.1

[6] C. D. Frisbie, L. F. Rozsnyai, A. Noy, M. S. Wrighton, and C. M. Lieber, Functional-group imaging by chemical force microscopy, Science **265**, 2071 (1994). 1, 3.1

[7] D. Rugar, H. J. Mamin, P. Guethner, S. E. Lambert, S. J.E., I. McFadyen, and T. Yogi, Magnetic force microscopy – General principles and application to longitudinal recording media, J. Appl. Phys. **68**, 1169 (1990). 1, 3.1

[8] Y. Martin, D. W. Abraham, and H. K. Wickramasinghe, High-resolution capacitance measurement and potentiometry by force microscopy, Appl. Phys. Lett. **52**, 1103 (1988). 1, 3.1

[9] S. Kalinin and A. Gruverman, *Scanning Probe Microscopy: Electrical and Electromechanical Phenomena at the Nanoscale*, Springer Verlag, New York, 2005. 1, 3.1

[10] M. Nonnenmacher, M. P. O'Boyle, and H. K. Wickramasinghe, Kelvin probe force microscopy, Appl. Phys. Lett. **58**, 2921 (1991). 1, 3.1

[11] W. Denk and D. W. Pohl, Local electrical dissipation imaged by scanning force microscopy, Appl. Phys. Lett. **59**, 2171 (1991). 1, 3.1

[12] T. D. Stowe, T. W. Kenny, D. J. Thomson, and D. Rugar, Silicon dopant imaging by dissipation force microscopy, Appl. Phys. Lett. **75**, 2785 (1999).

[13] J. Y. Park, D. F. Ogletree, P. A. Thiel, and M. Salmeron, Influence of carrier density on the friction properties of silicon *pn* junctions, Phys. Rev. B **76**, 064108 (2007). 3.1

[14] P. Hoffmann, S. Jeffery, J. Pethica, H. Ozer, and A. Oral, Energy dissipation in atomic force microscopy and atomic loss processes, Phys. Rev. Lett. **87**, 265502 (2001). 3.1

[15] I. Dorofeyev, H. Fuchs, G. Wenning, and B. Gotsmann, Brownian motion of microscopic solids under the action of fluctuating electromagnetic fields, Phys. Rev. Lett. **83**, 2402 (1999). 3.1

[16] S. Kuehn, R. F. Loring, and J. A. Marohn, Dielectric fluctuations and the origins of noncontact friction, Phys. Rev. Lett. **96**, 156103 (2006). 3.1, 3.3

[17] S. M. Yazdanian, J. A. Marohn, and R. F. Loring, Dielectric fluctuations in force

microscopy: Noncontact friction and frequency jitter, J. Chem. Phys. **128**, 224706 (2008). 1, 2.4.3, 3.1, 3.3, 3.3, 3.3, 3.5, 4.2.2, 5.2.3, 5.2.4

[18] S. Kuehn, S. A. Hickman, and J. A. Marohn, Advances in mechanical detection of magnetic resonance, J. Chem. Phys. **128**, 052208 (2008). 1, 6.1

[19] L. E. Walther, N. E. Israeloff, E. Vidal Russell, and H. Alvarez Gomariz, Mesoscopic-scale dielectric relaxation at the glass transition, Phys. Rev. B **57**, R15112 (1998). 1, 3.1, 3.4, 3.4, 3.5

[20] L. E. Walther, E. V. Russell, N. E. Israeloff, and H. A. Gomariz, Atomic force measurement of low-frequency dielectric noise, Appl. Phys. Lett. **72**, 3223 (1998). 3.4, 3.4, 3.5

[21] E. V. Russell, N. E. Israeloff, L. E. Walther, and H. A. Gomariz, Nanometer scale dielectric fluctuations at the glass transitions, Phys. Rev. Lett. **81**, 1461 (1998).

[22] E. V. Russell and N. E. Israeloff, Direct observation of molecular cooperativity near the glass transition, Nature **408**, 695 (2000). 3.5

[23] P. S. Crider, M. R. Majewski, J. Zhang, H. Oukris, and N. E. Israeloff, Local dielectric spectroscopy of polymer films, Appl. Phys. Lett. **91**, 013102 (2007).

[24] P. S. Crider, M. R. Majewski, J. Zhang, H. Oukris, and N. E. Israeloff, Local dielectric spectroscopy of near-surface glassy polymer dynamics, J. Chem. Phys. **128**, 044908 (2008). 1, 3.1, 3.4, 3.4

[25] E. M. Muller and J. A. Marohn, Microscopic evidence for spatially inhomogeneous charge trapping in pentacene, Adv. Mater. **17**, 1410 (2005). 1

[26] L. Burgi, T. Richards, M. Chiesa, R. H. Friend, and H. Sirringhaus, A microscopic view of charge transport in polymer transistors, Synth. Met. **146**, 297 (2004). 1

[27] W. Pasveer, J. Cottaar, C. Tanase, R. Coehoorn, P. Bobbert, P. Blom, M. De Leeuw, and M. Michels, Unified description of charge-carrier mobilities in disordered semiconducting polymers, Phys Rev. Lett. **94**, 1 (2005). 1, 5.1, 5.1.1, 5.1.1, 5.1.1, 5.2.1

[28] M. Bouhassoune, S. L. M. van Mensfoort, P. A. Bobbert, and R. Coehoorn, Carrier-density and field-dependent charge-carrier mobility in organic semiconductors with correlated gaussian disorder, Organic Electronics **10**, 437 (2009). 5.1, 5.1.1, 5.1.1

[29] H. Bässler, Charge transport in disordered organic photoconductors a monte carlo simulation study, Phys. Status Solidi (b) **175**, 15 (1993). 5.1.1

[30] D. H. Dunlap, P. E. Parris, and V. M. Kenkre, Charge-dipole model for the universal field dependence of mobilities in molecularly doped polymers, Phys. Rev. Lett. **77**, 542 (1996). 5.1.1, 5.1.1

[31] S. V. Novikov, D. H. Dunlap, V. M. Kenkre, P. E. Parris, and A. V. Vannikov, Essential role of correlations in governing charge transport in disordered organic materials, Phys. Rev. Lett. **81**, 4472 (1998). 5.1, 5.1.1, 5.1.1

[32] I. I. Fishchuk, V. I. Arkhipov, A. Kadashchuk, P. Heremans, and H. Bässler, Analytic model of hopping mobility at large charge carrier concentrations in disordered organic semiconductors: Polarons versus bare charge carriers, Phys. Rev. B **76**, 045210 (2007). 5.1.1

[33] P. M. Borsenberger and D. S. Weiss, *Organic Photoreceptors For Xerography*, Marcel Dekker, Inc., 1998. 1, 5.1, 5.2.1

[34] E. M. Roeling, W. C. Germs, B. Smalbrugge, E. J. Geluk, T. de Vries, R. A. J. Janssen, and M. Kemerink, Organic electronic ratchets doing work, Nat. Mater. **10**, 51 (2011). 1, 5.1, 5.3, 5.3

[35] K. Bruland, J. Garbini, W. Dougherty, S. Chao, S. Jensen, and J. Sidles, Thermal tuning of a fiber-optic interferometer for maximum sensitivity, Rev. Sci. Instrum. **70**, 3542 (1999). 2.1

[36] W. R. Silveira, *Microscopic View of Charge Injection in a Model Organic Semiconductor*, PhD thesis, Cornell University, 2005. 2.1, 5.1, 5.2.1

[37] S. A. Hickman, *Batch fabrication of cantilevered magnetic nanorods on attonewton-sensitivity silicon oscillators for magnetic resonance force microscopy*, PhD thesis, Cornell University, Ithaca, New York, 2010. 2.1

[38] T. R. Albrecht, P. Grutter, D. Horne, and D. Rugar, Frequency modulation detection using high-q cantilevers for enhanced force microscope sensitivity, J. Appl. Phys. **69**, 668 (1991). 2.1, 2.4.3, 2.4.4, 3.5, 4.1, 4.3, 4.3, 4.3

[39] E. W. Moore, *1. Mechanical Detection of Electron Spin Resonance from Nitroxide Spin Probes, 2. Ultrasensitive Cantilever Torque Magnetometry of Magnetization Switching in Individual Nickel Nanorods*, PhD thesis, Cornell University, 2011. 2.1, 2.1

[40] S. M. Yazdanian, *Scanned Probe Microscopy Studies of Thin Organic Films using Cantilever Frequency Noise*, PhD thesis, Cornell University, 2009. 2.1, 3.2, 5.2.1

[41] S. Kuehn, *Force-Gradient Detected Nuclear Magnetic Resonance and the Origins of Noncontact Friction*, PhD thesis, Cornell University, Ithaca, New York, 2007. 2.2, 6.4, 6.4

[42] J. L. Hutter and J. Bechhoefer, Calibration of atomic-force microscope tips, Rev. Sci. Instrum. **64**, 1868 (1993). 2.3

[43] F. J. Giessibl, Forces and frequency shifts in atomic-resolution dynamic-force microscopy, Phys. Rev. B **56**, 16010 (1997). 2.4

[44] H. Goldstein, C. Poole, and J. Safko, *Classical Mechanics*, Addison Wesley, 2002. 2.4

[45] A. Pathak and S. Mandal, Classical and quantum oscillators of quartic anharmonicities: second-order solution, Phys. Lett. A **286**, 261 (2001). 2.4

[46] C. A. Brau, *Modern Problems In Classical Electrodynamics*, Oxford University Press, INc., 2004. 2.4, 2.5

[47] W. R. Silveira, E. M. Muller, T. N. Ng, D. H. Dunlap, and J. A. Marohn, High-sensitivity electric force microscopy of organic electronic devices and materials, in *Scanning Probe Microscopy: Electrical and Electromechanical Phenomena at the Nanoscale*, edited by S. V. Kalinin and A. Gruverman, volume II, pages 788 – 830, Springer Verlag, New York, 2007. 2.4, 2.5

[48] O. Cherniavskaya, L. Chen, V. Weng, L. Yuditsky, and L. E. Brus, Quantitative noncontact electrostatic force imaging of nanocrystal polarizability, J. Phys. Chem. B **107**, 1525 (2003). 2.4, 2.4, 2.4, 2.4.1, 3.5, 4.2.2

[49] J. L. Luria, *Spectroscopic Characterization of Charge Generation and Trapping in Third-Generation Solar Cell Materials Using Wavelength- and Time-Resolved Electric Force Microscopy*, PhD thesis, Cornell University, 2011. 2.4.2, 4.2.1

[50] S. M. Yazdanian, N. Hoepker, S. Kuehn, R. F. Loring, and J. A. Marohn, Quantifying electric field gradient fluctuations over polymers using ultrasensitive cantilevers, Nano Lett. **9**, 3668 (2009). 2.4.3, 3.1, 3.3, 3.4, 3.5, 4.2.2, 4.2.2, 5.2.3, 5.2.4, 6.1

[51] Y. Obukhov, K. C. Fong, D. Daughton, and P. C. Hammel, Real time cantilever signal frequency determination using digital signal processing, J. Appl. Phys. **101**, 034315 (2007). 2.4.3, 3.5

[52] A. Labuda, J. R. Bates, and P. H. Grütter, The noise of coated cantilevers, Nanotech. **23**, 025503 (2012). 2.4.4

[53] J. D. Jackson, *Classical Electrodynamics*, John Wiley & Sons, Inc., 1998. 2.5

[54] Y. Qi, J. Y. Park, B. L. M. Hendriksen, D. F. Ogletree, and M. Salmeron, Electronic contribution to friction on gaas: An atomic force microscope study, Phys. Rev. B **77**, 184105 (2008). 3.1

[55] B. N. J. Persson and A. I. Volokitin, Comment on "brownian motion of microscopic solids under the action of fluctuating electromagnetic fields", Phys. Rev. Lett. **84**, 3504 (2000). 3.1

[56] P. Grütter, Y. Liu, P. LeBlanc, and U. Dürig, Magnetic dissipation force microscopy, Appl. Phys. Lett. **71**, 279 (1997). 3.1

[57] Y. Liu and P. Grütter, Theory of magnetoelastic dissipation due to domain wall width oscillation, J. Appl. Phys. **83**, 5922 (1998). 3.1

[58] B. Hoffmann, R. Houbertz, and U. Hartmann, Eddy current microscopy, Appl. Phys. A **66**, S409 (1998). 3.1

[59] V. Nalladega, S. Sathish, K. V. Jata, and M. P. Blodgett, Development of eddy current microscopy for high resolution electrical conductivity imaging using atomic force microscopy, Rev. Sci. Instrum. **79**, 073705 (2008). 3.1

[60] B. C. Stipe, H. J. Mamin, T. D. Stowe, T. W. Kenny, and D. Rugar, Magnetic dissipation and fluctuations in individual nanomagnets measured by ultrasensitive cantilever magnetometry, Phys. Rev. Lett. **86**, 2874 (2001). 3.1

[61] T. Ng, N. Jenkins, and J. Marohn, Thermomagnetic fluctuations and hysteresis loops of magnetic cantilevers for magnetic resonance force microscopy, IEEE Trans. Mag. **42**, 378 (2006). 3.1

[62] B. C. Stipe, H. J. Mamin, T. D. Stowe, T. W. Kenny, and D. Rugar, Noncontact friction and force fluctuations between closely spaced bodies, Phys. Rev. Lett. **87**, 096801 (2001). 3.1

[63] S. Kuehn, J. Marohn, and R. Loring, Noncontact dielectric friction, J. Phys. Chem. B **110**, 14525 (2006). 3.1, 3.3, 6.1

[64] T. D. Stowe, K. Yasumura, T. W. Kenny, D. Botkin, K. Wago, and D. Rugar, Attonewton force detection using ultrathin silicon cantilevers, Appl. Phys. Lett. **71**, 288 (1997). 3.1

[65] N. E. Jenkins, L. P. DeFlores, J. Allen, T. N. Ng, S. R. Garner, S. Kuehn, J. M. Dawlaty, and J. A. Marohn, Batch fabrication and characterization of ultrasensitive cantilevers with submicron magnetic tips, J. Vac. Sci. Technol. B **22**, 909 (2004). 3.1

[66] R. Richert and H. Wagner, The dielectric modulus: relaxation versus retardation, Solid State Ionics **105**, 167 (1998). 3.1, 3.5

[67] M. Tyagi, A. Alegría, and J. Colmenero, Broadband dielectric study of oligomer of poly(vinyl acetate): A detailed comparison of dynamics with its polymer analog, Phys. Rev. E **75**, 061805 (2007). 3.1

[68] U. Tracht, A. Heuer, and H. W. Spiess, Geometry of reorientational dynamics in supercooled poly(vinyl acetate) studied by ^{13}C two-dimensional nuclear magnetic resonance echo experiments, J. Chem. Phys. **111**, 3720 (1999). 3.1, 3.5

[69] N. E. Israeloff, Dielectric polarization noise through the glass transition, Phys. Rev. B **53**, R11913 (1996). 3.4, 3.5

[70] N. E. Israeloff and T. S. Grigera, Low-frequency dielectric fluctuations near the glass transition, Europhys. Lett. **43**, 308 (1998). 3.5

[71] N. G. McCrum, B. E. Read, and G. Williams, *Anelastic and Dielectric Effects in Polymeric Solids*, Dover Publications Inc., 1991. 3.5

[72] M. Scharber, D. Mhlbacher, M. Koppe, P. Denk, C. Waldauf, A. Heeger, and C. Brabec, Design rules for donors in bulk-heterojunction solar cells–Towards 10% energy-conversion efficiency, Adv. Mater. **18**, 789 (2006). 4.1

[73] G. Dennler, M. C. Scharber, T. Ameri, P. Denk, K. Forberich, C. Waldauf, and C. J. Brabec, Design rules for donors in bulk-heterojunction tandem solar cells-towards 15% energy-conversion efficiency, Adv. Mater. **20**, 579 (2008). 4.1

[74] C. R. McNeill and N. C. Greenham, Conjugated-polymer blends for optoelectronics, Adv. Mater. **21**, 3840 (2009). 4.1

[75] Y. Liang, D. Feng, Y. Wu, S.-T. Tsai, G. Li, C. Ray, and L. Yu, Highly efficient solar cell polymers developed via fine-tuning of structural and electronic properties, J. Am. Chem. Soc. **131**, 7792 (2009). 4.1

[76] A. C. Arias, N. Corcoran, M. Banach, R. H. Friend, J. D. MacKenzie, and W. T. S. Huck, Vertically segregated polymer-blend photovoltaic thin-film structures through surface-mediated solution processing, Appl. Phys. Lett. **80**, 1695 (2002). 4.1

[77] C. Groves, O. G. Reid, and D. S. Ginger, Heterogeneity in polymer solar cells: Local morphology and performance in organic photovoltaics studied with scanning probe microscopy, Acc. Chem. Res. **43**, 612 (2010). 4.1

[78] C. J. Brabec, A. Cravino, D. Meissner, N. S. Sariciftci, T. Fromherz, M. T. Rispens, L. Sanchez, and J. C. Hummelen, Origin of the open circuit voltage of plastic solar cells, Adv. Funct. Mater. **11**, 374 (2001). 4.1

[79] B. A. Gregg, Excitonic solar cells, J. Phys. Chem. B **107**, 4688 (2003).

[80] P. Peumans and S. R. Forrest, Separation of geminate charge-pairs at donor-acceptor interfaces in disordered solids, Chem. Phys. Lett. **398**, 27 (2004).

[81] L. J. A. Koster, V. D. Mihailetchi, R. Ramaker, and P. W. M. Blom, Light intensity dependence of open-circuit voltage of polymer:fullerene solar cells, Appl. Phys. Lett. **86**, 123509 (2005).

[82] B. P. Rand, D. P. Burk, and S. R. Forrest, Offset energies at organic semiconductor heterojunctions and their influence on the open-circuit voltage of thin-film solar cells, Phys. Rev. B **75**, 115327 (2007).

[83] S. Westenhoff, I. A. Howard, J. M. Hodgkiss, K. R. Kirov, H. A. Bronstein, C. K. Williams, N. C. Greenham, and R. H. Friend, Charge recombination in organic photovoltaic devices with high open-circuit voltages, J. Am. Chem. Soc. **130**, 13653 (2008).

[84] W. J. Potscavage, Jr., A. Sharma, and B. Kippelen, Critical interfaces in organic solar cells and their influence on the open-circuit voltage, Acc. Chem. Res. **42**, 1758 (2009).

[85] G. Garcia-Belmonte and J. Bisquert, Open-circuit voltage limit caused by recombination through tail states in bulk heterojunction polymer-fullerene solar cells, Appl. Phys. Lett. **96**, 113301 (2010).

[86] O. G. Reid, H. Xin, S. A. Jenekhe, and D. S. Ginger, Nanostructure determines the intensity-dependence of open-circuit voltage in plastic solar cells, J. Appl. Phys. **108**, 084320 (2010). 4.1

[87] A. Maurano et al., Recombination dynamics as a key determinant of open circuit voltage in organic bulk heterojunction solar cells: A comparison of four different donor polymers, Adv. Mater. **22**, 4987 (2010).

[88] C. W. Schlenker and M. E. Thompson, The molecular nature of photovoltage losses in organic solar cells, Chem. Commun. **47**, 3702 (2011). 4.1

[89] L. S. C. Pingree, O. G. Reid, and D. S. Ginger, Electrical scanning probe microscopy on active organic electronic devices, Adv. Mater. **21**, 19 (2009). 4.1

[90] M. Chiesa, L. Bürgi, J. S. Kim, R. Shikler, R. H. Friend, and H. Sirringhaus, Correlation between surface photovoltage and blend morphology in polyfluorene-based photodiodes, Nano Lett. **5**, 559 (2005). 4.1, 4.2.1, 4.2.2

[91] K. Maturova, M. Kemerink, M. Wienk, D. Charrier, and R. Janssen, Scanning Kelvin probe microscopy on bulk heterojunction polymer blends, Adv. Funct. Mater. **19**, 1379 (2009). 4.2.2

[92] O. G. Reid, G. E. Rayermann, D. C. Coffey, and D. S. Ginger, Imaging local trap formation in conjugated polymer solar cells: A comparison of time-resolved electrostatic force microscopy and scanning kelvin probe imaging, J. Phys. Chem. C **114**, 20672 (2010). 4.1

[93] E. J. Spadafora, R. Demadrille, B. Ratier, and B. Grevin, Imaging the carrier photogeneration in nanoscale phase segregated organic heterojunctions by kelvin probe force microscopy, Nano Lett. **10**, 3337 (2010). 4.1

[94] D. C. Coffey and D. S. Ginger, Time-resolved electrostatic force microscopy of polymer solar cells, Nat. Mater. **5**, 735 (2006). 4.1, 4.2.1, 5.3

[95] R. Giridharagopal, G. E. Rayermann, G. Shao, D. T. Moore, O. G. Reid, A. F. Tillack, D. J. Masiello, and D. S. Ginger, Submicrosecond time resolution atomic force microscopy for probing nanoscale dynamics, Nano Letters **12**, 893 (2012). 4.1

[96] T. A. Bull, L. S. C. Pingree, S. A. Jenekhe, D. S. Ginger, and C. K. Luscombe, The role of mesoscopic pcbm crystallites in solvent vapor annealed copolymer solar cells, ACS Nano **3**, 627 (2009). 4.1

[97] L. S. C. Pingree, O. G. Reid, and D. S. Ginger, Imaging the evolution of nanoscale photocurrent collection and transport networks during annealing of polythiophene/fullerene solar cells, Nano Lett. **9**, 2946 (2009).

[98] X.-D. Dang, A. Mikhailovsky, and T.-Q. Nguyen, Measurement of nanoscale external quantum efficiency of conjugated polymer:fullerene solar cells by photoconductive atomic force microscopy, Appl. Phys. Lett. **97**, 113303 (2010).

[99] X.-D. Dang, A. B. Tamayo, J. Seo, C. V. Hoven, B. Walker, and T.-Q. Nguyen, Nanostructure and optoelectronic characterization of small molecule bulk heterojunction solar cells by photoconductive atomic force microscopy, Adv. Funct. Mater. **20**, 3314 (2010).

[100] B. H. Hamadani, S. Jung, P. M. Haney, L. J. Richter, and N. B. Zhitenev, Origin of nanoscale variations in photoresponse of an organic solar cell, Nano Lett. **10**, 1611 (2010).

[101] B. H. Hamadani, N. Gergel-Hackett, P. M. Haney, and N. B. Zhitenev, Imaging of

nanoscale charge transport in bulk heterojunction solar cells, J. Appl. Phys. **109**, 124501 (2011). 4.1

[102] C. R. McNeill and P. C. Dastoor, Photocurrent pattern formation in polymer/methanofullerene blends imaged by near-field scanning photocurrent microscopy, J. Appl. Phys. **99**, 033502 (2006). 4.1

[103] T. J. K. Brenner and C. R. Mcneill, Spatially resolved spectroscopic mapping of photocurrent and photoluminescence in polymer blend photovoltaic devices, J. Phys. Chem. C **115**, 19364 (2011). 4.1, 4.2.1, 4.2.1

[104] Y. Xia and R. Friend, Phase separation of polyfluorene-based blend films and its influence on device operations, Adv. Mater. **18**, 1371 (2006). 4.1

[105] C. R. McNeill, B. Watts, L. Thomsen, H. Ade, N. C. Greenham, and P. C. Dastoor, X-ray microscopy of photovoltaic polyfluorene blends: Relating nanomorphology to device performance, Macromolecules **40**, 3263 (2007). 4.1, 4.2.1

[106] A. Cadby, G. Khalil, A. M. Fox, and D. G. Lidzey, Mapping exciton quenching in photovoltaic-applicable polymer blends using time-resolved scanning near-field optical microscopy, J. Appl. Phy. **103**, 093715 (2008). 4.1

[107] H. Snaith, A. Arias, A. Morteani, C. Silva, and R. Friend, Charge generation kinetics and transport mechanisms in blended polyfluorene photovoltaic devices, Nano Lett. **2**, 1353 (2002). 4.1, 4.2.1

[108] C. R. McNeill, H. Frohne, J. L. Holdsworth, and P. C. Dastoor, Near-field scanning photocurrent measurements of polyfluorene blend devices: Directly correlating morphology with current generation, Nano Lett. **4**, 2503 (2004). 4.2.1

[109] R. Shikler, M. Chiesa, and R. H. Friend, Photovoltaic performance and morphology of polyfluorene blends: The influence of phase separation evolution, Macromolecules **39**, 5393 (2006). 4.1

[110] A. Carbone, C. Pennetta, and L. Reggiani, Trapping-detrapping fluctuations in organic space-charge layers, Appl. Phys. Lett. **95**, 233303 (2009). 4.1

[111] A. Carbone, B. K. Kotowska, and D. Kotowski, f^{γ} current fluctuations in organic semiconductors: evidence for percolation, Eur. Phys. J. D **50**, 77 (2006). 4.1, 5.1.3

[112] T. D. Krauss and L. E. Brus, Charge, polarizability, and photoionization of single semiconductor nanocrystals, Phys. Rev. Lett. **83**, 4840 (1999). 4.1, 4.3

[113] L. Cockins, Y. Miyahara, S. D. Bennett, A. A. Clerk, and P. Grutter, Excited-state spectroscopy on an individual quantum dot using atomic force microscopy, Nano Lett. **12**, 709 (2012). 4.1

[114] L. Cockins, Y. Miyahara, and P. Grutter, Spatially resolved low-frequency noise measured by atomic force microscopy, Phys. Rev. B **79**, 121309 (2009). 4.1

[115] S. Machlup, Noise in semiconductors: Spectrum of a two-parameter random signal, J. Appl. Phys. **25**, 341 (1954). 4.2.2

[116] Y. Zhang and P. W. M. Blom, Electron and hole transport in poly(fluorene-benzothiadiazole), Appl. Phys. Lett. **98**, 143504 (2011). 4.2.2

[117] C. Jundt, G. Klein, B. Sipp, J. Lemoigne, M. Joucla, and A. A. Villaeys, Excition dynamics in pentacene thin-fims studied by pump-probe spectroscopy, Chem . Phys. Lett. **241**, 84 (1995). 4.4

[118] H. Marciniak, M. Fiebig, M. Huth, S. Schiefer, B. Nickel, F. Selmaier, and S. Lochbrunner, Ultrafast exciton relaxation in microcrystalline pentacene films, Phys. Rev. Lett. **99**, 176402 (2007). 4.4, 4.4

[119] T. N. Ng, *Developments in Force Detection: Integrated Cantilever Magnetometry and Electric Force Microscopy of Organic Semiconductors*, PhD thesis, Cornell University, 206. 5.1, 6.4

[120] C. Tanase, E. J. Meijer, P. W. M. Blom, and D. M. de Leeuw, Unification of the hole transport in polymeric field-effect transistors and light-emitting diodes, Phys. Rev. Lett. **91**, 216601 (2003). 5.1, 5.1.1

[121] N. I. Craciun, J. Wildeman, and P. W. M. Blom, Universal Arrhenius temperature activated charge transport in diodes from disordered organic semiconductors, Phys. Rev. Lett. **100**, 056601 (2008). 5.1, 5.1.1, 5.1.1

[122] M. Surin, P. Leclère, R. Lazzaroni, J. D. Yuen, G. Wang, D. Moses, A. J. Heeger, S. Cho, and K. Lee, Relationship between the microscopic morphology and the charge transport properties in poly(3-hexylthiophene) field-effect transistors, J. Appl. Phys. **100**, 033712 (2006). 5.1

[123] R. Ruiz, A. Papadimitratos, A. Mayer, and G. Malliaras, Thickness dependence of mobility in pentacene thin-film transistors, Adv. Mater. **17**, 1795 (2005). 5.1

[124] T. Sakanoue and H. Sirringhaus, Band-like temperature dependence of mobility in a solution-processed organic semiconductor, Nat. Mater. **9**, 736 (2010). 5.1.1

[125] S. Verlaak, V. Arkhipov, and P. Heremans, Modeling of transport in polycrystalline organic semiconductor films, Appl. Phys. Lett. **82**, 745 (2003). 5.1.1

[126] I. N. Hulea, H. B. Brom, A. J. Houtepen, D. Vanmaekelbergh, J. J. Kelly, and E. A. Meulenkamp, Wide energy-window view on the density of states and hole mobility in poly(*p*-phenylene vinylene), Phys. Rev. Lett. **93**, 166601 (2004). 5.1.1

[127] O. Tal, Y. Rosenwaks, Y. Preezant, N. Tessler, C. Chan, and A. Kahn, Direct determination of the hole density of states in undoped and doped amorphous organic films with high lateral resolution, Phys. Rev. Lett. **95**, 256405 (2005). 5.1.1

[128] Z. G. Yu, D. L. Smith, A. Saxena, R. L. Martin, and A. R. Bishop, Molecular geometry fluctuation model for the mobility of conjugated polymers, Phys. Rev. Lett. **84**, 721 (2000). 5.1.1

[129] P. E. Parris, M. Kuś, D. H. Dunlap, and V. M. Kenkre, Nonlinear response theory: Transport coefficients for driving fields of arbitrary magnitude, Phys. Rev. E **56**, 5295 (1997). 5.1.1, 5.1.1

[130] D. H. Dunlap, V. M. Kenkre, and P. E. Parris, What is behind the $\sqrt{E}$?, J. Imag. Sci. Tech. **43**, 437 (1999). 5.1.1

[131] M. C. J. M. Vissenberg and M. Matters, Theory of the field-effect mobility in amorphous organic transistors, Phys. Rev. B **57**, 12964 (1998). 5.1.1

[132] M. Kemerink, T. Hallam, M. J. Lee, N. Zhao, M. Caironi, and H. Sirringhaus, Temperature- and density-dependent channel potentials in high-mobility organic field-effect transistors, Phys. Rev. B **80**, 115325 (2009). 5.1.1

[133] S. D. Baranovskii, H. Cordes, F. Hensel, and G. Leising, Charge-carrier transport in disordered organic solids, Phys. Rev. B **62**, 7934 (2000). 5.1.1

[134] N. Vukmirovic and L.-W. Wang, Charge carrier motion in disordered conjugated polymers: A multiscale ab initio study, Nano Lett. **9**, 3996 (2009). 5.1.1, 5.2.1

[135] Y. Roichman and N. Tessler, Generalized Einstein relation for disordered semiconductors—implications for device performance, Appl. Phys. Lett. **80**, 1948 (2002). 5.1.1

[136] S. L. M. van Mensfoort and R. Coehoorn, Effect of gaussian disorder on the voltage dependence of the current density in sandwich-type devices based on organic semiconductors, Phys. Rev. B **78**, 085207 (2008). 5.1.1

[137] O. G. Reid, K. Munechika, and D. S. Ginger, Space charge limited current measurements on conjugated polymer films using conductive atomic force microscopy, Nano Lett. **8**, 1602 (2008). 5.1.2

[138] W. E. Spear, The hole mobility in selenium, Proc. Phys. Soc. **76**, 826 (1960). 5.1.2

[139] J. Oliver H. LeBlanc, Hole and electron drift mobilities in anthracene, J. Chem. Phys. **33**, 626 (1960).

[140] R. G. Kepler, Charge carrier production and mobility in anthracene crystals, Phys. Rev. **119**, 1226 (1960). 5.1.2

[141] L. Dunn, D. Basu, L. Wang, and A. Dodabalapur, Organic field effect transistor mobility from transient response analysis, Appl. Phys. Lett. **88**, 063507 (2006). 5.1.2

[142] D. Basu, L. Wang, L. Dunn, B. Yoo, S. Nadkarni, A. Dodabalapur, M. Heeney, and I. McCulloch, Direct measurement of carrier drift velocity and mobility in a polymer field-effect transistor, Appl. Phys. Lett. **89**, 242104 (2006).

[143] R. Dost, A. Das, and M. Grell, Time-of-flight mobility measurements in organic field-effect transistors, J. Appl. Phys. **104**, 084519 (2008). 5.1.2

[144] G. Juška, K. Arlauskas, M. Viliūnas, and J. Kočka, Extraction current transients: New method of study of charge transport in microcrystalline silicon, Phys. Rev. Lett. **84**, 4946 (2000). 5.1.2

[145] S. Tiwari and N. Greenham, Charge mobility measurement techniques in organic semiconductors, Opt. Quant. Electron. **41**, 69 (2009). 5.1.2, 5.1.2

[146] P. G. Schouten, J. M. Warman, and M. P. de Haas, Effect of accumulated radiation dose on pulse radiolysis conductivity transients in a mesomorphic octa-n-alkoxy-substituted phthalocyanine, J. Chem. Phys. **97**, 9863 (1993). 5.1.2

[147] L. Burgi, H. Sirringhaus, and R. H. Friend, Noncontact potentiometry of polymer field-effect transistors, Appl. Phys. Lett. **80**, 2913 (2002). 5.1.2

[148] V. Podzorov, E. Menard, J. Rogers, and M. Gershenson, Hall effect in the accumulation layers on the surface of organic semiconductors, Phys. Rev. Lett. **95**, 226601 (2005). 5.1.2

[149] A. Carbone, B. K. Kotowska, and D. Kotowski, Space-charge-limited current fluctuations in organic semiconductors, Phys. Rev. Lett. **95**, 236601 (2005). 5.1.3

[150] M. Sampietro, G. Ferrari, D. Natali, U. Scherf, K. O. Annan, F. P. Wenzl, and G. Leising, Tracking of conduction phenomena and degradation in organic light emitting diodes by current noise measurements, Appl. Phys. Lett. **78**, 3262 (2001). 5.1.3

[151] A. N. Pal and A. Ghosh, Resistance noise in electrically biased bilayer graphene, Phys. Rev. Lett. **102**, 126805 (2009). 5.1.3

[152] I. Shlimak, Y. Kraftmakher, R. Ussyshkin, and K. Zilberberg, $1/f$ hopping noise in crystalline germanium, Solid State Commun. **93**, 829 (1995). 5.1.3

[153] V. I. Kozub, Low-frequency noise due to site energy fluctuations in hopping conductivity, Solid State Commun. **97**, 843 (1996). 5.1.3

[154] V. Y. Pokrovskii, A. K. Savchenko, W. R. Tribe, and E. H. Linfield, Modulation origin of $1/f$ noise in two-dimensional hopping, Phys. Rev. B **64**, 201318 (2001). 5.1.3

[155] M. Jaquith, E. Muller, and J. Marohn, Time-resolved electric force microscopy of charge trapping in polycrystalline pentacene, J. Phys. Chem. B **111**, 7711 (2007). 5.2.1, 6.1

[156] J. A. Marohn, Internal group documents. 5.2.2

[157] D. Lee, A. Wetzel, R. Bennewitz, E. Meyer, M. Despont, P. Vettiger, and C. Gerber, Switchable cantilever for a time-of-flight scanning force microscope, Appl. Phys. Lett. **84**, 1558 (2004). 5.3

[158] A. Leyk, C. Böhm, D. W. van der Weide, and E. Kubalek, 104 GHz signals measured by high frequency scanning force microscope test systems, Electron. Lett. **31**, 1046 (1995). 5.3, 6.1

[159] A. Leyk and E. Kubalek, High spatially resolved MMIC-internal millimetre-wave measurements of sinusoidal signals by high frequency electric force microscope-testing, Electron. Lett. **34**, 196 (1998).

[160] J. Bangert and E. Kubalek, Digital signal measurements with electric force microscope testing, Surf. Interface Anal. **27**, 307 (1999). 5.3, 6.1

[161] D. van der Weide and P. Neuzil, The nanoscilloscope: Combined topography and AC field probing with a micromachined tips, J. Vac. Sci. Technol. B **14**, 4144 (1996). 5.3

[162] D. van der Weide, Localized picosecond resolution with a near-field microwave/scanning-force microscope, Appl. Phys. Lett. **70**, 677 (1997). 5.3

[163] E. M. Roeling, W. C. Germs, B. Smalbrugge, E. J. Geluk, T. de Vries, R. A. J. Janssen, and M. Kemerink, Scaling of characteristic frequencies of organic electronic ratchets, Phys. Rev. B **85** (2012). 5.3

[164] E. M. Roeling, W. C. Germs, B. Smalbrugge, E. J. Geluk, T. de Vries, R. A. J. Janssen, and M. Kemerink, The performance of organic electronic ratchets, AIP Adv. **2** (2012). 5.3

[165] S. Scheinert and G. Paasch, Fabrication and analysis of polymer field-effect transistors, Phys. Status Solidi (a) **201**, 1263 (2004). 5.3

[166] H. Kawakatsu, S. Kawai, D. Saya, M. Nagashio, D. Kobayashi, H. Toshiyoshi, and H. Fujita, Towards atomic force microscopy up to 100 MHz, Review of Scientific Instruments **73**, 2317 (2002). 6.1

[167] R. Ried, H. Mamin, B. Terris, L.-S. Fan, and D. Rugar, 6-MHz 2-N/m piezoresistive atomic-force microscope cantilevers with INCISIVE tips, Microelectromechanical Systems, Journal of **6**, 294 (1997).

[168] S. Hosaka, K. Etoh, A. Kikukawa, H. Koyanagi, and K. Itoh, 6.6 MHz silicon AFM cantilever for high-speed readout in AFM-based recording, Microelectronic Engineering **46**, 109 (1999). 6.1

[169] U. Kemiktarak, T. Ndukum, K. C. Schwab, and K. L. Ekinci, Radio-frequency scanning tunnelling microscopy, Nature **450**, 85 (2007). 6.1

[170] E. W. Moore, S. G. Lee, S. A. Hickman, S. J. Wright, L. E. Harrell, P. P. Borbat, J. H.

Freed, and J. A. Marohn, Scanned-probe detection of electron spin resonance from a nitroxide spin probe, Proc. Natl. Acad. Sci. U.S.A. **106**, 22251 (2009). 6.1

[171] C. L. Degen, M. Poggio, H. J. Mamin, C. T. Rettner, and D. Rugar, Nanoscale magnetic resonance imaging, Proc. Natl. Acad. Sci. U.S.A. **106**, 1313 (2009).

[172] D. Rugar, R. Budakian, H. J. Mamin, and B. W. Chui, Single spin detection by magnetic resonance force microscopy, Nature **430**, 329 (2004). 6.1

[173] J. M. Nichol, E. R. Hemesath, L. J. Lauhon, and R. Budakian, Nanomechanical detection of nuclear magnetic resonance using a silicon nanowire oscillator, Phys. Rev. B **85**, 054414 (2012). 6.1

[174] S. R. Garner, S. Kuehn, J. M. Dawlaty, N. E. Jenkins, and J. A. Marohn, Force-gradient detected nuclear magnetic resonance, Appl. Phys. Lett. **84**, 5091 (2004). 6.1

[175] K. L. Ekinci, Electromechanical transducers at the nanoscale: Actuation and sensing of motion in nanoelectromechanical systems (nems), Small **1**, 786 (2005). 6.1

[176] M. F. Bocko, K. A. Stephenson, and R. H. Koch, Vacuum tunneling probe: A nonreciprocal, reduced-back-action transducer, Phys. Rev. Lett. **61**, 726 (1988). 6.1

[177] C. Meyer, H. Lorenz, and K. Karrai, Optical detection of quasi-static actuation of nanoelectromechanical systems, Appl. Phys. Lett. **83**, 2420 (2003). 6.1

[178] T. Kouh, D. Karabacak, D. H. Kim, and K. L. Ekinci, Diffraction effects in optical interferometric displacement detection in nanoelectromechanical systems, Appl. Phys. Lett. **86**, 013106 (2005). 6.1

[179] J. M. Nichol, E. R. Hemesath, L. J. Lauhon, and R. Budakian, Displacement detection of silicon nanowires by polarization-enhanced fiber-optic interferometry, Appl. Phys. Lett. **93**, 193110 (2008). 6.1

[180] H. Park, A. K. L. Lim, A. P. Alivisatos, J. Park, and P. L. McEuen, Fabrication of metallic electrodes with nanometer separation by electromigration, Appl. Phys. Lett. **75**, 301 (1999). 6.2

[181] P. A. Truitt, J. B. Hertzberg, C. C. Huang, K. L. Ekinci, and K. C. Schwab, Efficient and sensitive capacitive readout of nanomechanical resonator arrays, Nano Lett. **7**, 120 (2007). 6.2, 6.5, 6.5

[182] N. E. Jenkins, *Expanding the Limits of Magnetic Resonance Force Microscopy*, PhD thesis, Cornell University, Ithaca, New York, 2007. 6.3

[183] D. S. Greywall, B. Yurke, P. A. Busch, A. N. Pargellis, and R. L. Willett, Evading amplifier noise in nonlinear oscillators, Phys. Rev. Lett. **72**, 2992 (1994). 6.3

[184] B. Yurke, D. S. Greywall, A. N. Pargellis, and P. A. Busch, Theory of amplifier-noise evasion in an oscillator employing a nonlinear resonator, Phys. Rev. A **51**, 4211 (1995). 6.3, 6.4

[185] X. M. Henry Huang, C. A. Zorman, M. Mehregany, and M. L. Roukes, Nanoelectromechanical systems: Nanodevice motion at microwave frequencies, Nature **421**, 496 (2003). 6.4

[186] A. Cleland and M. Roukes, External control of dissipation in a nanometer-scale radiofrequency mechanical resonator, Sensor Actuat. A - Phys. **72**, 256 (1999). 6.4

[187] J. Brugger, N. Blanc, P. Renaud, and N. de Rooij, Microlever with combined integrated

sensor/actuator functions for scanning force microscopy, Sensors and Actuators A: Physical **43**, 339 (1994). 6.5

[188] L. Sekaric, J. M. Parpia, H. G. Craighead, T. Feygelson, B. H. Houston, and J. E. Butler, Nanomechanical resonant structures in nanocrystalline diamond, Appl. Phys. Lett. **81**, 4455 (2002). 6.5